Structure d’un front de combustion propagé en co-courant dans un lit fixe de schiste bitumineux broyé

Márcio Ferreira Martins

Márcio Ferreira Martins. Structure d’un front de combustion propagé en co-courant dans un lit fixe de schiste bitumineux broyé. Energie électrique. Institut National Polytechnique (Toulouse), 2008. Français. NNT : 2008INPT025G . tel-04477874

HAL Id: tel-04477874
https://hal.science/tel-04477874
Submitted on 26 Feb 2024

THÈSE

En vue de l'obtention du

DOCTORAT DE L'UNIVERSITÉ DE TOULOUSE

Délivré par *L'INSTITUT NATIONAL POLYTECHNIQUE DE TOULOUSE*
Discipline ou spécialité : *Énergétique et Tranferts*

Présentée et soutenue par *Márcio FERREIRA MARTINS*
Le *29 septembre 2008*

Titre : *The structure of a combustion front propagating in a fixed bed of crushed oil shale: co-current configuration*

JURY
CONSALVI Jean-Louis (Rapporteur)
REIN Guillermo (Rapporteur)
KAMP Arjan (Membre)
QUINTARD Michel (Membre)
THOVERT Jean-François (Membre)
VANTELON Jean-Pierre (Invité)

Ecole doctorale : *MEGeP (Mécanique, Energétique, Procédés, Génie Civil)*
Unité de recherche : *Centre RAPSODEE. EMAC-CNRS 2392*
Directeur(s) de Thèse : *SALVADOR Sylvain*
Rapporteurs : *CONSALVI Jean-Louis et REIN Guillermo*

Université de Toulouse
École doctorale : MEGeP
Centre RAPSODEE, UMR EMAC-CNRS 2392

Résumé

Pour

Márcio Ferreira Martins

Structure d'un front de combustion propagé en co-courant dans un lit fixe de schiste bitumineux broyé

La propagation d'un front de combustion au sein d'un milieu poreux réactif met en œuvre des mécanismes thermiques, chimiques et de transfert, avec de forts couplages. Afin de caractériser la structure thermique et chimique du front, un dispositif expérimental finement instrumenté permettant la réalisation d'expériences de combustion co-courant 1D a été mis au point, puis validé avec un milieu poreux modèle : un mélange carbone/sable. Ce réacteur à lit fixe vertical est alimenté en air descendant ; un dispositif original permet de prélever des microéchantillons de gaz au sein même du front.

La combustion du schiste bitumineux de Timahdit au Maroc broyé à 500-1000 µm et additionné de sable est réalisée avec une vitesse d'air (de Darcy à 20°C) de 0.024 $m\ s^{-1}$. Le front se propage à 6.13×10^{-5} $m\ s^{-1}$ et sa température de pic est de 1100 °C.

Un bilan matière est établi sur la base d'une caractérisation chimique et physique détaillée du milieu, de son résidu solide après combustion et des produits gazeux. La matière organique est convertie pour ¼ en carbone fixe – dont l'oxydation fournit l'énergie qui propage le front - ¼ en gaz de pyrolyse et ½ en huile.

Un modèle numérique à deux températures développé par l'IMFT a été validé. Les approches à la fois expérimentale et numérique permettent *in fine* d'évaluer l'épaisseur des différentes zones de réaction : devolatilisation du schiste, oxydation du résidu carboné et décarbonatation de $CaCO_3$.

Une étude de variation des paramètres principaux - vitesse d'air et taille des particules - est finalement proposée.

University of Toulouse
Doctoral school: MEGeP
Centre RAPSODEE, UMR EMAC-CNRS 2392

Abstract

by

Márcio Ferreira Martins

The structure of a combustion front propagating in a fixed bed of crushed oil shale: co-current configuration

The propagation of a combustion front in reactive porous medium involves thermal, chemical and fluid flow mechanisms, with strong couplings. In order to describe the thermal and chemical structure of the combustion front, a new experimental device, finely instrumented, allowing to carry out 1D experiments in co-current combustion was designed and developed. To validate the combustion cell, a porous medium model - a mix of charcoal/sand was used. This fixed bed down flow reactor is equipped with an original system that allows micro sampling gas within the combustion front.

For the experiments with the oil shale from Timahdit in Morocco, it was crushed and sieved into particle size at 500-1000 μm and mixed with sand. The combustion was carried out at air velocity of 0.024 m s^{-1} at STP. The front propagates at 6.13×10^{-5} m s^{-1} and its temperature peak is 1100 °C.

A mass balance was made based on a detailed chemical and physical characterization of the medium, its solid residue after combustion and flue gas. The organic matter is converted into ¼ of fixed carbon – which the oxidation reactions provide the energy to propagate the front - ¼ into pyrolysis gas and ½ into oil.

A two temperature numerical model developed by IMFT was validated. Combining, experimental and numerical approach made it possible *in fine* to evaluate the thickness of the different reaction zones: oil shale devolatilization, fixed carbon oxidation and $CaCO_3$ decarbonation.

A parametric study varying the air velocity and particle size is finally proposed.

Publication List

Papers

1. M.F. MARTINS, S. SALVADOR, J-F. THOVERT, G. DEBENEST. *Co-current combustion of oil shale – Part 1: Characterisation of the solid and gaseous products*. Submitted.

2. M.F. MARTINS, S. SALVADOR, J-F. THOVERT, G. DEBENEST. *Co-current combustion of oil shale – Part 2: Structure of the combustion front.* Submitted.

3. A. LAPENE, G. DEBENEST, M. QUINTARD, M.F. MARTINS, S. Salvador. *Numerical Simulation of Combustion in Reactive Porous Media.* International Review of Mechanical Engineering (I.RE.M.E.), Vol. xx, n. x. *Accepted*, 2008.

Conferences

1. M.F. MARTINS, S. SALVADOR, G. DEBENEST. *Pyrolysis and combustion of oil shale for oil recovery.* 18th International Symposium on Analytical and Applied Pyrolysis (PYR08). Lanzarote, Canary Islands, (Spain) 2008.

2. A. LAPENE, G. DEBENEST, M. QUINTAR, M.F. MARTINS, S. SALVADOR. *Heat and mass transport in a reactive porous medium: Application to oil shales and heavy oil combustion. 2007* Annual Meeting AIChE, Salt Lake City, Utah (USA), 2007.

3. M.F. MARTINS, S. SALVADOR, A. LAPENE, G. DEBENEST, J.-F. THOVERT, J.-M. COMMANDRE. *Thermochemical characterization of combustion front structure in reactive porous media: a new experimental device.* Seminários EUROTHERM. Reactive Heat Transfer in Porous Media - Ecole des Mines d'Albi (France), 2007.

4. A. LAPENE, M.F. MARTINS, G. DEBENEST, S. SALVADOR S, M. QUINTARD, *Numerical simulation of oil shale combustion in a fixed bed : modelling and chemical aspects.* Seminários EUROTHERM. Reactive Heat Transfer in Porous Media - Ecole des Mines d'Albi (France), 2007.

5. M.F. MARTINS, S. SALVADOR, M. QUINTARD, J.-F. THOVERT, J.-M. COMMANDRE. *Caractérisation thermochimique de la structure d'un front de combustion en milieu poreux réactif : nouveau dispositif expérimental.* Congresso SFT – Société Française de Thermique (France), 2007.

6. A. LAPENE, M.F. MARTINS, G. DEBENEST. *Modélisation numérique de la combustion en lit fixe de combustibles solides.* Congresso SFT – Société Française de Thermique (France), 2007.

Acknowledgments

Firstly I would like to express my faith by citing a proverb:

"In everything you do, put God first, and he will direct you and crown your efforts with success".

I would like to thank my family for encouraging me and giving me emotional support for this foreign adventure in France.

A very special thanks goes out to my wife and best friend, Fabienne Costa, for accompanying me and share with me this adventure and without whose love, encouragement, I would not have finished this thesis. I would like to highlight her expertise in English during the text corrections.

I must also acknowledge my supervisor, Prof. Sylvain Salvador. It was under his tutelage that I could improve my rigor in scientific research. He provided me with direction, technical support and became more of a mentor and friend, than a professor. He also introduced me Jean-Michel Commandré, a fantastic person that with his wife helped me a lot at the beginning… when I were still confused "chômage" with "chauffage".

I would like to thank Dr. Jean-François Thovert and Dr. Michel Quintard for the great scientific collaboration and interchange during the three years of PhD work. I would also acknowledge Dr. Gerald Debenest and Alexandre Lapene for helping me with the numerical model simulations.

I am very grateful for the technical staff of the laboratory: Bernard Auduc for helping me to develop five times "our" combustion cell and share with me a great friendship moments: "c'est pas Bena, c'est Berrrnarrd" – wonderful!!!. I would also like to acknowledge Denis Marty and Jean-Marie Sabathier for their technical support.

I am so happy to have as best Friend: Francisco Sepulveda, Mouna Chkir, Mr. & Mrs. Romaroson, Cristina Serbanescu, Marius Draga, Amigo Hassen (The "Argentine") and my colleague of office, Rondana.

In conclusion, I recognize that this research would not have been possible without the financial assistance of MENRT and INP Toulouse. I express my gratitude to those agencies.

“...Tudo o que se vê não é igual ao que a gente viu há um segundo
Tudo muda o tempo todo no mundo...”
Lulu Santos

Table of contents

Literature

Experimental devices and methods

Detailed characterization

Experimental results and discussion

1D numerical model

List of figures

List of Tables

Introduction and objectives

The propagation of a combustion front can be found in many cases in nature and industry. In both the propagation is initiated by some heat source. After ignited a combustion front is propagated to adjacent elements of neighbors. In certain aspects the propagation of a combustion front can be very useful. The advantages are some industrial applications as in-situ combustion or gasification, municipal solid waste (MSW) incinerations and biomass combustion in fixed bed. The propagation of a combustion front also has the negative side - fires in bulk materials, coal deposits and waste dumps.

The domains of petroleum, waste treatment and fire safety have stimulated considerable research. Previous studies approve the combustion front propagation as a complex procedure depending on chemical, thermal and physical processes. Due to this complexity, challenges still persist for investigation of combustion propagation both from numerical and from experimental perspective. In the following, some of these challenges will be summarized and the aims will be formulated for this thesis.

Heat transfer in reactive porous medium is a complex problem, caused by the interactions between the gas phase and solid phase, and between particles. The problem is further aggravated by the transportation of chemical species directly dependent on the porous medium composition, in which the combustion front is propagated. For a bed constituted by coal, the coal undergoes several transformations in different zones: heating, drying, pyrolyzing and burning, leaving ash. The chemical constitution of the bed becomes more complex when organic matter is associated with mineral matrix. This association adds disadvantages and advantages:

- Disadvantages, the interferences in the overall energy balance: it is commonly found in the mineral matter compounds such as carbonates, which at a high temperature release CO_2 in a strong endothermic reaction; the CO_2 released is found mixed in the flue gas.

- Advantages, it is known that after the combustion process the geometric stability of a particle bed undergoes a drastic shrinkage. For a bed constituted of charcoal particle, during the combustion process, the overall diameter of the bed decreases causing problems in relationship between the air flow rate imposed and its corresponding velocity on a cross section of the bed. Thus, when the organic matter is associated with the mineral matrix, the particle bed can preserve its geometric stability during the combustion process.

Two good examples of solid combustibles that gather both, geometric stability and complex reaction mechanism are bituminous sands and oil shales. For that reason, oil shale was chosen as porous medium in this work.

In addition, another challenge is presented: "How can one determine the thickness of the reaction zones?" Today, the contributions about this subject are mainly in the field of biomass combustion, MSW incineration and fire hazard. Thus, some propositions are made with the help of numerical models [Fatehi&Kaviany1994, Zhou2005 and Rein2006]. By contrast, the literature about oil shale combustion is very limited yet. Particularly in co-current situation which is useful in in-situ process for recovering hydrocarbons from oil shale.

Another interesting question remains a challenge: what is actually oxidizing during the propagation of a combustion front: the solid residue after devolatilization only or also part of the volatile matter? Some authors established that different regimes of combustion can be observed, and depending on the regime the volatile matter can be completely, partially or not oxidized. These regimes are commonly demonstrated using experimental setup in counter-current combustion configurations.

To obtain a better understanding of the dynamic behavior of co-current combustion front propagation in porous medium, the following aims were determined for this thesis:

- The development of a complete experimental device;
- The development of a new and original micro-sampling system to evaluate chemical structure of a combustion front: thickness of devolatilization zone, of the solid residue oxidation zone and of the mineral matrix decarbonation zone;

- To operate repeatable experiments in a controlled situation;

- To provide detailed physical, chemical and thermochemical characterization of the porous medium;

- To establish what is actually oxidizing during the process of reactive medium combustion;

- To establish overall mass balances of the combustion process;

- To answer the question: are the carbonates constituting the oil shale decarbonated at the passage of the front? There is indeed an important environmental issue in this question because the carbonation decomposition rate is directly linked with the CO_2 emissions;

- To validate a 1D numerical model that simulates the combustion front propagation. This tool was developed with two laboratories: Institut de Mécanique des Fluides de Toulouse (IMFT) and Laboratoire de Combustion et de Détonique (LCD) in cooperative group works during the thesis;

The present work is divided into five parts.

- In the first chapter is presented the oil shale and its characteristics. After that, some processes and technologies involving reactive porous medium combustion are presented. Then, a literature review of the main phenomena that take place during the propagation of a combustion front, and also a literature review of the most remarkable experimental works are made. Finally, is introduced a global vision of the numerical models used to investigate the propagation of a combustion front in a porous medium.

- The second chapter describes the experimental device developed to perform co-current combustion in a fixed bed. It is also described a new and original micro-sampling system to evaluate chemical structure of a combustion front. Various other experimental devices used during this thesis and their experimental protocols are presented as well.

- The third chapter is dedicated to perform a detailed characterization of the oil shale: physical, chemical and thermal properties. Then, is made a fine analysis of the devolatilization gases.

- The fourth chapter presents the results obtained using the experimental device developed. This chapter is subdivided into two main parts:

  - The first one presents the results from the experimental device filled with a "simple" medium used to calibrate the cell: mix charcoal/sand. A mass balance of the combustion process is described and validated.

  - The second part concerns the combustion of a mix of oil shale/sand. There, a reference case is exhaustively studied. It is described a general observation during and after combustion. The analyses of the solid residue after combustion and the flue gas are shown; some comments about the shale oil recovery are made. The mass balance validated previously with the "simple" medium is used to propose a mass balance of the oil shale combustion process. Finally, is presented the physical aspects of the propagation of a combustion front. In this section is proposed a study and evaluation of reactions zone thickness, based on the micro-sampling system developed specifically for this purpose.

- In the last chapter, a 1D two temperatures numerical model developed by IMFT/LCD is confronted with the experiments made in order to evaluate how far the combustion of oil shale can be described, and to gain information about the front structure. Firstly, a mathematical formulation and a solution method are presented. The model is completed using the physical, chemical and heat transfer properties determined experimentally. The case presented in the chapter IV is simulated. Eventually, is proposed a parametric study varying air velocity and particle size.

Chapter I

Literature

In first chapter is presented the oil shale and its characteristics. After that, some processes and technologies involving reactive porous medium combustion are presented. Then, a literature review of the main phenomena that take place during the propagation of a combustion front, and also a literature review of the most remarkable experimental works are made. Finally, is introduced a global vision of the numerical models used to investigate the propagation of a combustion front in a porous medium.

I.1 Oil shale

I.1.1 Definition

Oil shale is a sedimentary rock, Figure (I.1), containing a relatively large amount of organic matter (10 to 65%) called kerogen, from which a significant amount of liquid fuel and combustible gas can be extracted by pyrolysis/ combustion.

Figure (I.1) - Mined oil shale material

Historically, the oil shale has been mined as illustrated in Figure (I.2), by (Hamilton 2005). To extract any useable hydrocarbons from the shale, the rock must be crushed and then heated.

Figure (I.2) - Left: the 1947 photo of a Bureau of Mines experiment in Rifle, Colorado. Right: Queensland oil shale mine.

I.1.2 Deposits

Oil-shale deposits can be found in many parts of the world. They range in age from Cambrian to Tertiary and were deposited in a variety of depositional environments, including fresh-water to highly saline lakes, epicontinental marine basins and subtidal shelves, and in limnic and coastal swamps, commonly in association with deposits of coal. The deposits may occur as minor accumulations or giant deposits that occupy thousands of square kilometers and reach thicknesses of 700 m or more. In order to illustrate, Figure (I.3) by (Dyni 2005, 9) and Figure (I.4) by (Dyni 2005, 23) present the typical lithologic columns for two types of oil shales, respectively Brazil and Morocco.

In Figure (I.3), the oil shale occurs in two beds separated by barren shale and limestone. The upper and lower oil-shale beds are 6.5 and 3.2 m thick, respectively.

Figure (I.4) shows the stratigraphic section of Timahdit deposit in Morocco. This deposit is located about 250 km southeast of Rabat; it underlies an area about 70 km long and 4 to10 km wide within a northeast-trending syncline. This deposit consists of several layers (C, T, Y, X, M and S) and each one is subdivided into many sub-zones containing a different amount of organic matter (15 to 20%). The thickness of the oil shale layer ranges from 80 to 170 m. According (Bekri 1996) the highest amount of oil can be obtained by the sub-zone Y.

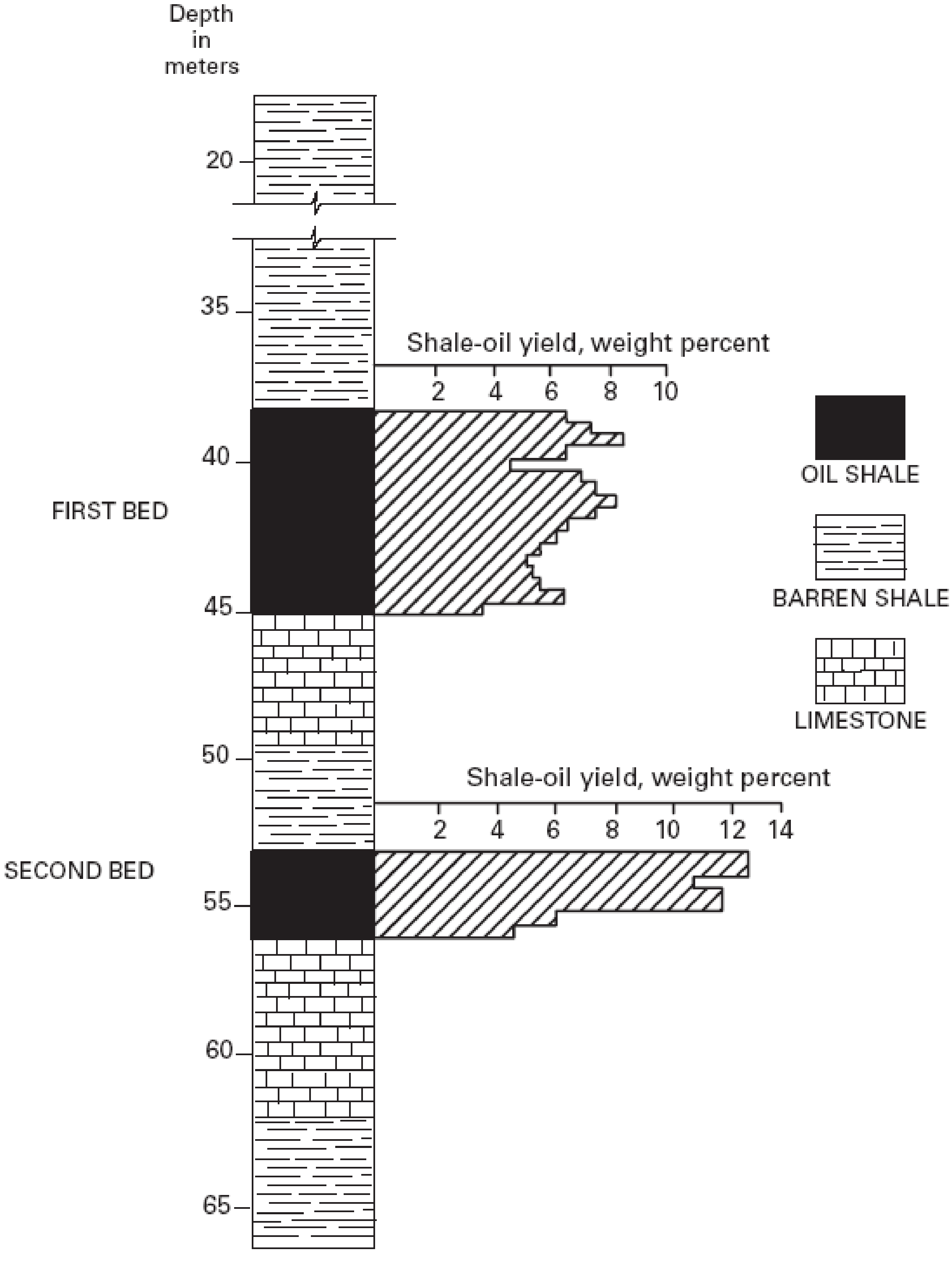

Figure (I.3) - Typical lithologic column of the Iratí oil shale at São Mateus do Sul, Brazil. by Petrobras

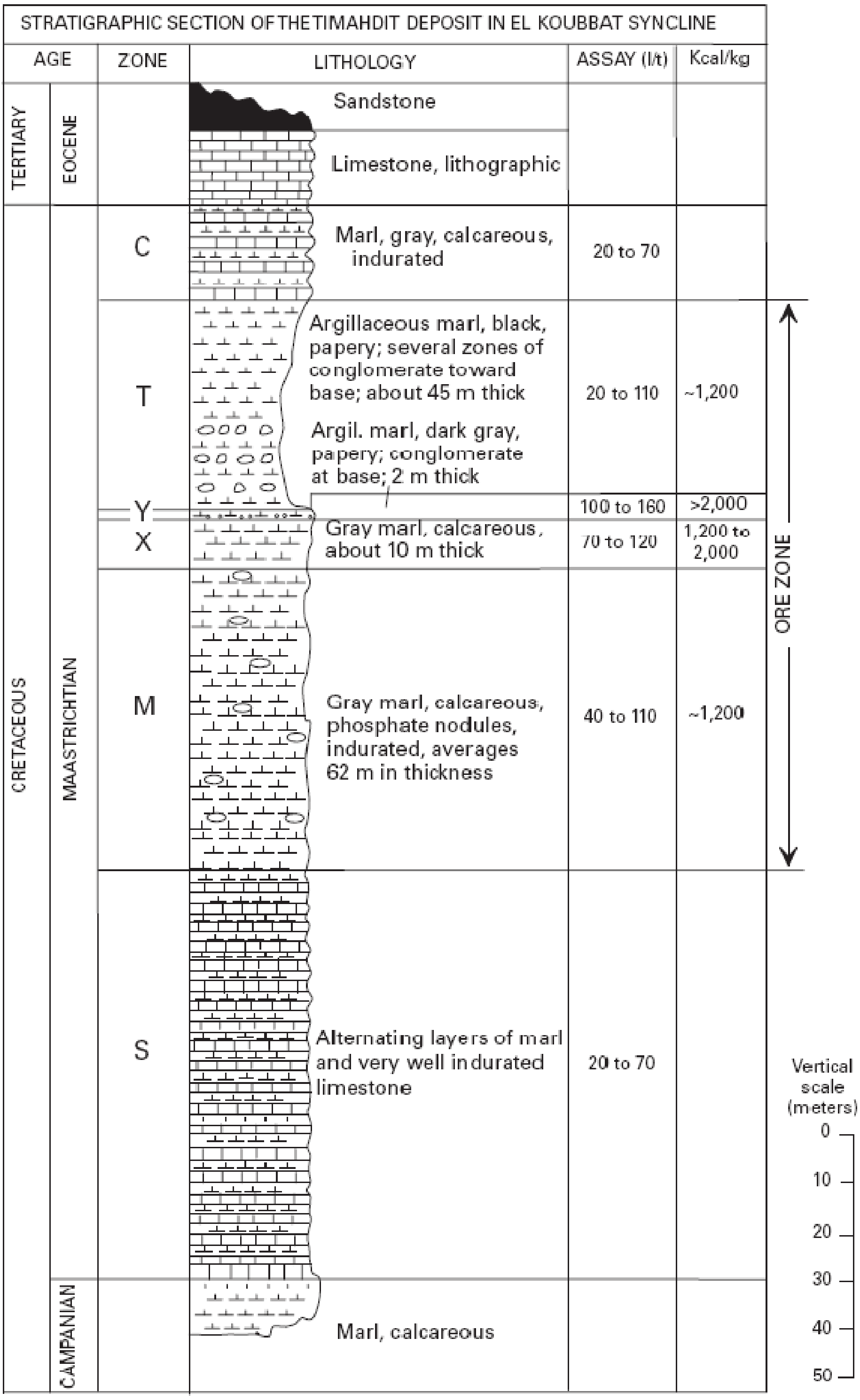

Figure (I.4) -Generalized stratigraphic section of the Timahdit oil-shale deposit in El Koubbat syncline, Morocco.

I.1.3 Composition and characteristics

The oil shale has two main compounds: organic matter and mineral matter.

- Organic matter in oil shale includes the remains of algae, spores, pollen, plant cuticle and corky fragments of herbaceous and woody plants, and other cellular remains of lacustrine, marine, and land plants. These materials are composed essentially of carbon, hydrogen, oxygen, nitrogen, and sulfur. In some kind of oil shales, the organic matter is unstructured and it is best described as amorphous (bituminite). Most of the organic matter in oil shale is insoluble in ordinary organic solvents. The organic matter of oil shale (which is the source of liquid and gaseous hydrocarbons) typically has a higher hydrogen and lower oxygen content than lignite and bituminous coal (Dyni 2005).

- In terms of mineral content, oil shales usually contain much larger amounts of inert mineral matter (60–90 %) (Dyni 2005). The mineral matter of some oil shales is composed of carbonates including calcite, dolomite, and siderite. In other kinds of oil shales, silicates including quartz, feldspar, and clay minerals are dominant and carbonates are a minor component. The general composition of oil shales is given in Figure (I.5) by (Altun, *et al.* 2006).

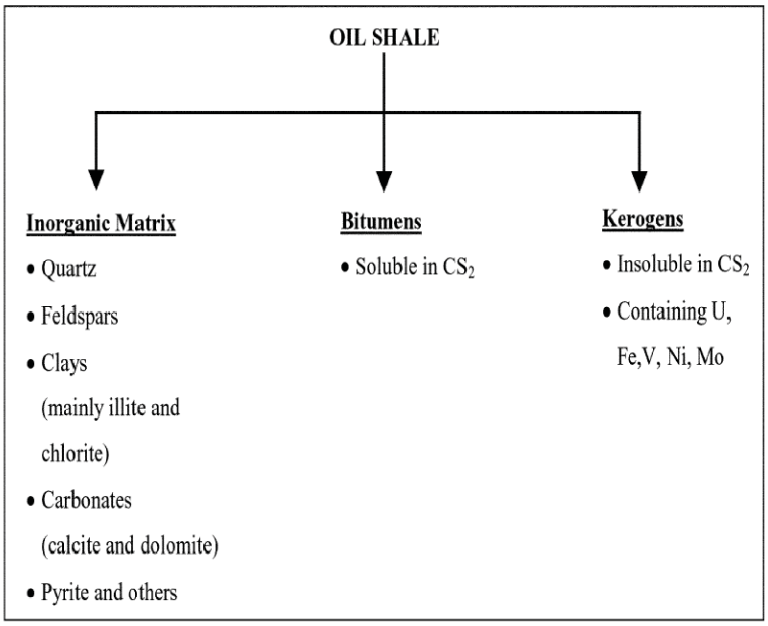

Figure (I.5) -General composition of oil shale.

A deposit of oil shale having economic potential is generally one that is at or near enough to the surface to be developed by open-pit or conventional underground mining, or by in-situ methods. Commercial grades of oil shale, as determined by their yield of shale oil, range from about 100 to 200 liters per metric ton (l/t) of rock. Total resources of a selected group of oil shale deposits in 33 countries are estimated at 409 billion tons of in-situ shale oil, which is equivalent to 2.8 trillion U.S. barrels of shale oil (Dyni 2005).

The gross heating value of oil shales on a dry-weight basis ranges from about 500 to 4000 kcal/kg of rock. The high-grade kukersite oil shale of Estonia, which fuels several electric power plants, has a heating value of about 2000 to 2200 kcal/kg. By comparison, the heating value of lignitic coal ranges from 3500 to 4600 kcal kg^{-1} on a dry, mineral-free basis (Dyni 2005).

Table (I.1) by (Altun, *et al.* 2006) presents some characteristics of several well-known oil shale deposits in world.

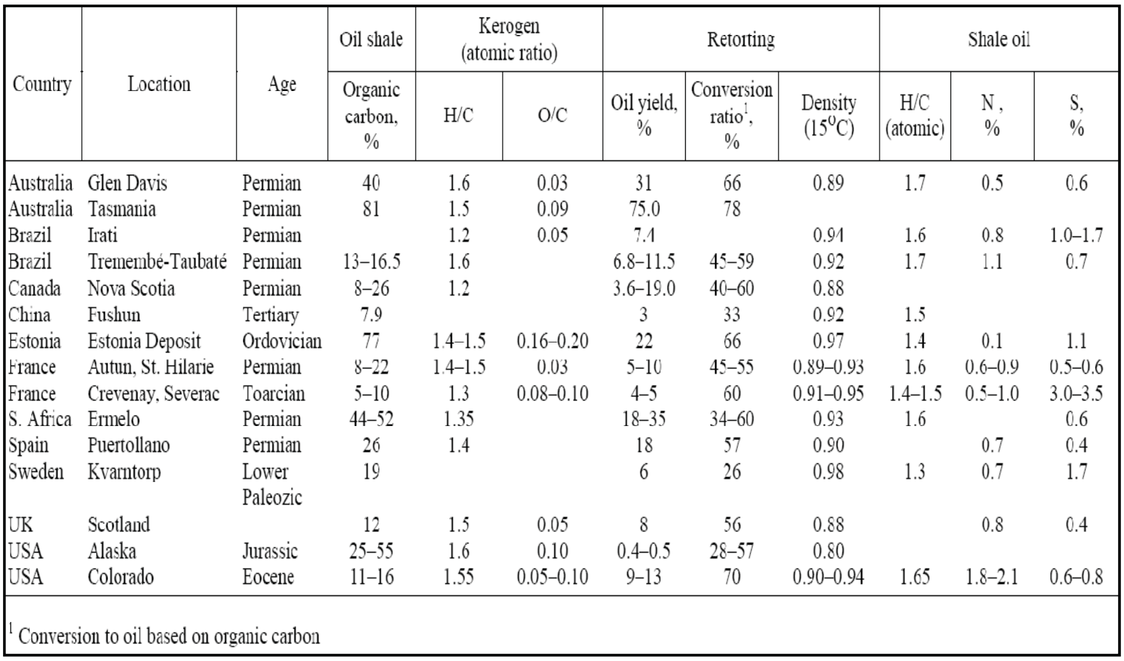

Country	Location	Age	Oil shale	Kerogen (atomic ratio)		Retorting			Shale oil		
			Organic carbon, %	H/C	O/C	Oil yield, %	Conversion ratio[1], %	Density (15^0C)	H/C (atomic)	N , %	S, %
Australia	Glen Davis	Permian	40	1.6	0.03	31	66	0.89	1.7	0.5	0.6
Australia	Tasmania	Permian	81	1.5	0.09	75.0	78				
Brazil	Irati	Permian		1.2	0.05	7.4		0.94	1.6	0.8	1.0–1.7
Brazil	Tremembé-Taubaté	Permian	13–16.5	1.6		6.8–11.5	45–59	0.92	1.7	1.1	0.7
Canada	Nova Scotia	Permian	8–26	1.2		3.6–19.0	40–60	0.88			
China	Fushun	Tertiary	7.9			3	33	0.92	1.5		
Estonia	Estonia Deposit	Ordovician	77	1.4–1.5	0.16–0.20	22	66	0.97	1.4	0.1	1.1
France	Autun, St. Hilarie	Permian	8–22	1.4–1.5	0.03	5–10	45–55	0.89–0.93	1.6	0.6–0.9	0.5–0.6
France	Crevenay, Severac	Toarcian	5–10	1.3	0.08–0.10	4–5	60	0.91–0.95	1.4–1.5	0.5–1.0	3.0–3.5
S. Africa	Ermelo	Permian	44–52	1.35		18–35	34–60	0.93	1.6		0.6
Spain	Puertollano	Permian	26	1.4		18	57	0.90		0.7	0.4
Sweden	Kvarntorp	Lower Paleozic	19			6	26	0.98	1.3	0.7	1.7
UK	Scotland		12	1.5	0.05	8	56	0.88		0.8	0.4
USA	Alaska	Jurassic	25–55	1.6	0.10	0.4–0.5	28–57	0.80			
USA	Colorado	Eocene	11–16	1.55	0.05–0.10	9–13	70	0.90–0.94	1.65	1.8–2.1	0.6–0.8

[1] Conversion to oil based on organic carbon

Table (I.1) -Properties of some important oil shale deposits.

These deposits are characterized by their age, the organic carbon wt. % of organic matter, and oil yield which the conversion to oil is based on organic carbon percentage. The atomic ratio H/C (hydrogen to carbon) of kerogen as a way to evaluate the quality of organic matter in source rocks. The organic matter in oil shale has been studied extensively and the composition of kerogen in oil shale is found to vary significantly from deposit to deposit. The fraction of kerogen converted into oil with increasing temperature depends upon the hydrogen content or organic matter;

oil yield increases with increasing hydrogen content. Because the density of the organic matter is significantly less than minerals in shale, oil shale density can be used to estimate oil yield by including a conversion factor for the transformation of kerogen to oil. This relationship is used to calculate oil shale reserves.

I.2 Processes and technologies used in porous medium combustion

Combustion is one of the oldest technologies of mankind. It has been used for more than a million years for different purposes. To avoid a imminent fuel crisis due to the increasing demand and depleting fossil fuel reserves, the performance of existing combustion systems needs to further improve and also to reduce the emissions levels to meet the international emission norms.

The literature about porous medium subject distinguishes two types of problems. The first one considers only combustion of the gas phase inside an inert solid porous medium. In second type, the solid phase reacts with the gas phase; chemical reactions such as pyrolysis of the solid and further oxidation of the residual carbon occur, accompanied by changes in physical structure of the solid phase. The media are called non-inert porous medium. This latter case corresponds to the combustion process considered in this work.

Oil shale must be heated to temperatures between 400 and 500°C to convert the embedded sediments to kerogen oil and combustible gases. This can be achieved by mining the shale and heating it in *surface retorts*, or by contacting and heating the oil shale *in-place (in-situ)*.

I.2.1 Surface retort process

Figure (I.6) presents one of the most successful vertical retorts found in world. An 11m vertical shaft Gas Combustion Retort (GCR) achieves high retorting and thermal efficiencies and requires no cooling water. A variation called Petrosix is operating in Brazil [(Johnson, Crawford and Bunger 2004) and (Lisbôa, Rombaldo and Rodrigues 2006)].

The main process steps in production of shale oil are:

- Crushed shale moves continuously downward by gravity;

- Recycled gases enter the bottom and are heated by retorted shale. Air is injected and mixes with the rising hot re-cycle gases;

- Combustion of gases and residual carbon from the spent shale heats the raw shale above the combustion zone to retorting temperature;

- Oil vapors and gases cooled by the incoming shale leave the top of the retort as a mist.

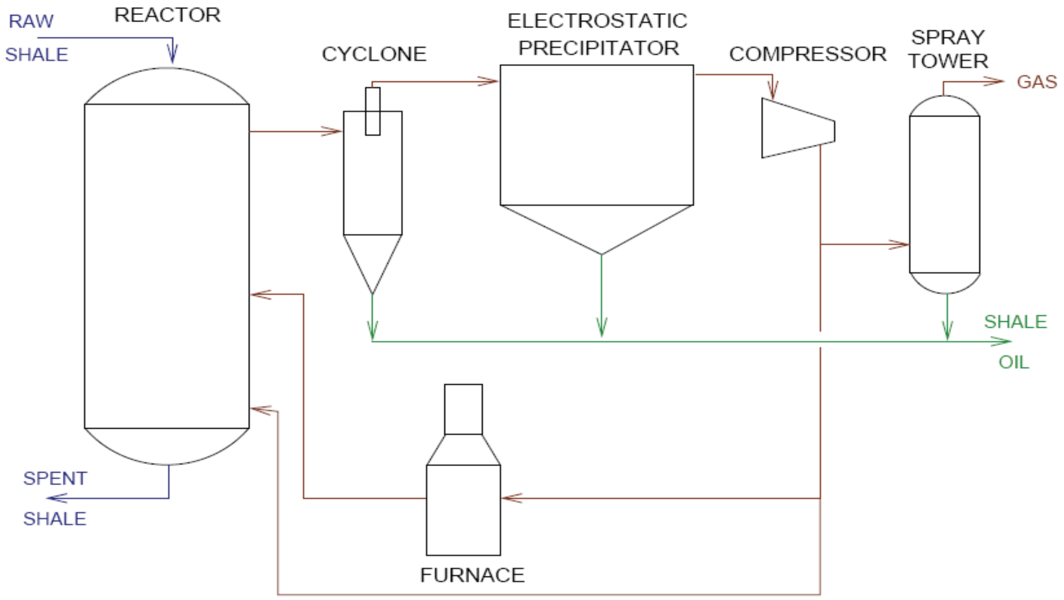

Figure (I.6) - General scheme for a Gas Combustion Retort of the type used by Petrobras in its Petrosix oil shale production process.

Petrobras uses a conventional production process in which the shale is mined, crushed to typically 1.2 to 7.5 cm and fed into a surface gas combustion retort for pyrolysis and processing, Figure (I.7) (Lisbôa, Rombaldo and Rodrigues 2006).

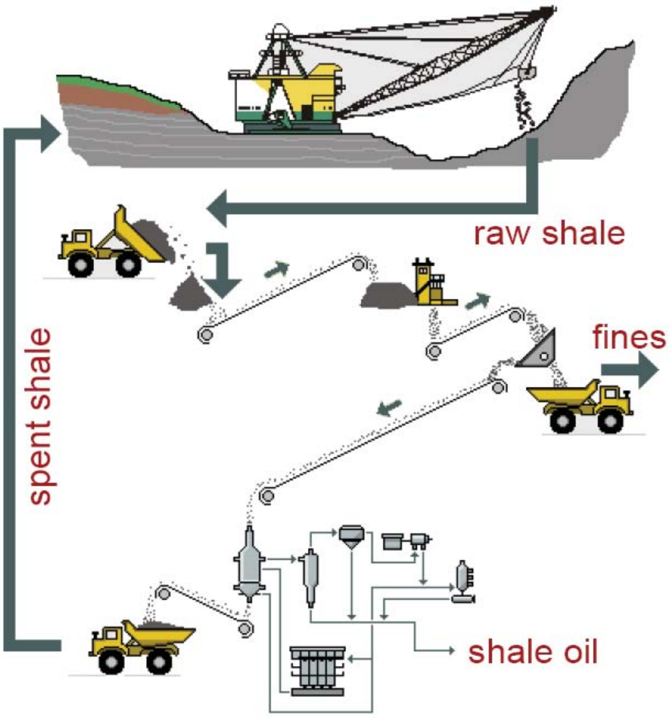

Figure (I.7) - Oil shale plant: the mine site, the solids preparation plant and the retorting unit.

I.2.2 In-Situ Process

In-situ processes can be technically feasible in deeper and richer deposits where the rock has natural permeability or where permeability can be created by fracturing. Among the most promising in-situ processes are: *True in-situ processes*, *Modified in-situ (MIS)* and other *"Modified True in-situ" process.*

- The True in-situ processes involve no mining, Figure (I.8) (Johnson, Crawford and Bunger 2004, 47). The rock is fractured, air is injected, then the oil shale is ignited to heat the formation, and shale oil moves through fractures to production wells. Difficulties in controlling the combustion front and the flow of oil can limit oil recovery, leaving areas unheated and some oil unrecovered.

- The MIS process may involve mining. An underground cavern is excavated and an explosive charge detonated to fill the cavern with broken shale rubble. The rock is heated by igniting the top of the target deposit and recovering fluids from ahead of or beneath the heated zone. Modified in-situ processes improve performances by heating more the oil shale, improving the flow of gases and liquids through the rock formation, and increasing volumes and quality of the oil produced.

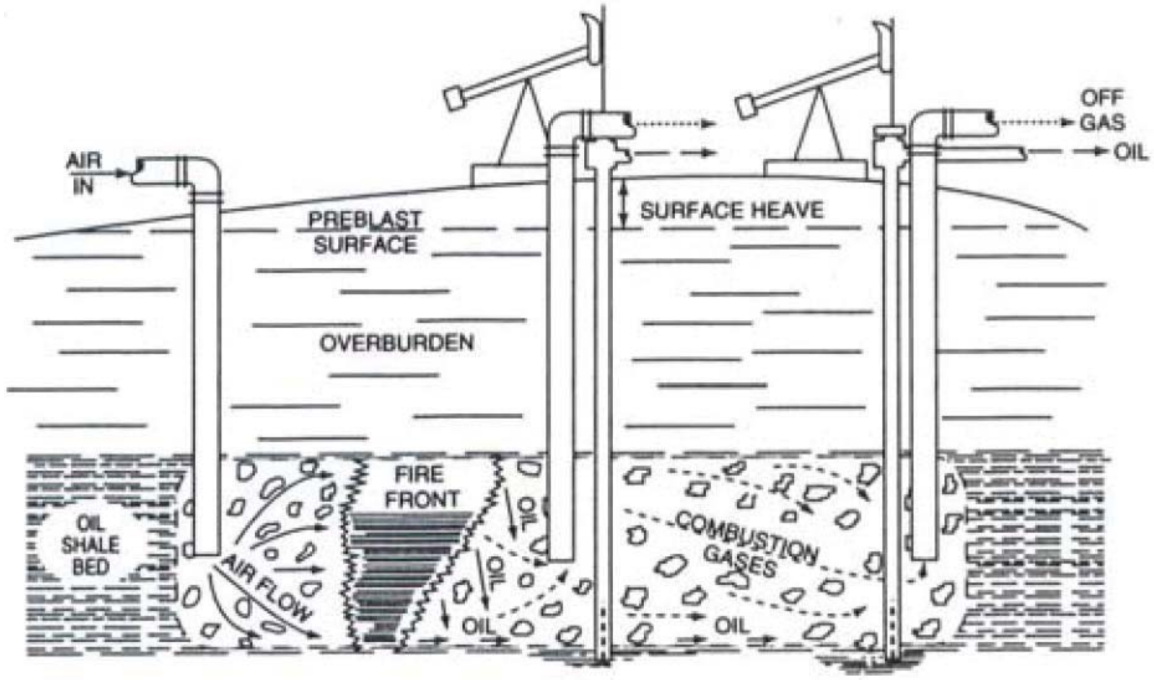

Figure (I.8) - True In-Situ Process schematic.

I.2.3 Other smoldering combustion processes

Beyond the processes to recover unconventional fuels described before, there are other processes where a combustion front is propagated in a reactive porous medium, i.e. the smoldering combustion processes. Smoldering combustion is described as an exothermic superficial heterogeneous-reaction that can propagate in interior of porous fuels, and is a self-sustaining reaction in which the heat released by surface oxidation causes pyrolysis of the unaffected fuel adjacent to the reaction zone, which in turn yields a rigid char, which that subsequently undergoes surface oxidation (Ohlemiller 1985).

Smoldering of coal seams, coal waste or storage piles are recognized to cause environmental and economical problems of global extent. In addition, such kind of coal fires represents one of the most challenging hazards for worldwide coal industries, Figure (I.9) (Countryman and McDaniel 2004).

Figure (I.9) - Fire erupts from the coal face. Blair Athol coal mine at Clermont, New South Wales, Australia.

Municipal solid waste (MSW) incineration and biomass combustion are process that also involving the combustion front in a reactive medium, Figure (I.10) (Winderickx s.d., 1), Figure (I.11) (CanREN 2001, 1) respectively.

In incinerator process, the waste is left by the garbage trucks in waste bunker of the incineration plant. By shifting and tumbling tiles the waste moves slowly down and burns. The combustion chamber is fed with air from the waste bunker. This stinking air cannot escape from the incineration plant and contains also oxygen (O_2) for the degasification and the combustion process. The temperature is around 950 °C and the retention time of the waste in furnace is 45 minutes to 1 hour.

The fundamental investigation of combustion characteristics of waste materials and their mixtures in a fixed bed is the key to understanding the combustion parameters as the ignition and burning rates in combustion performance.

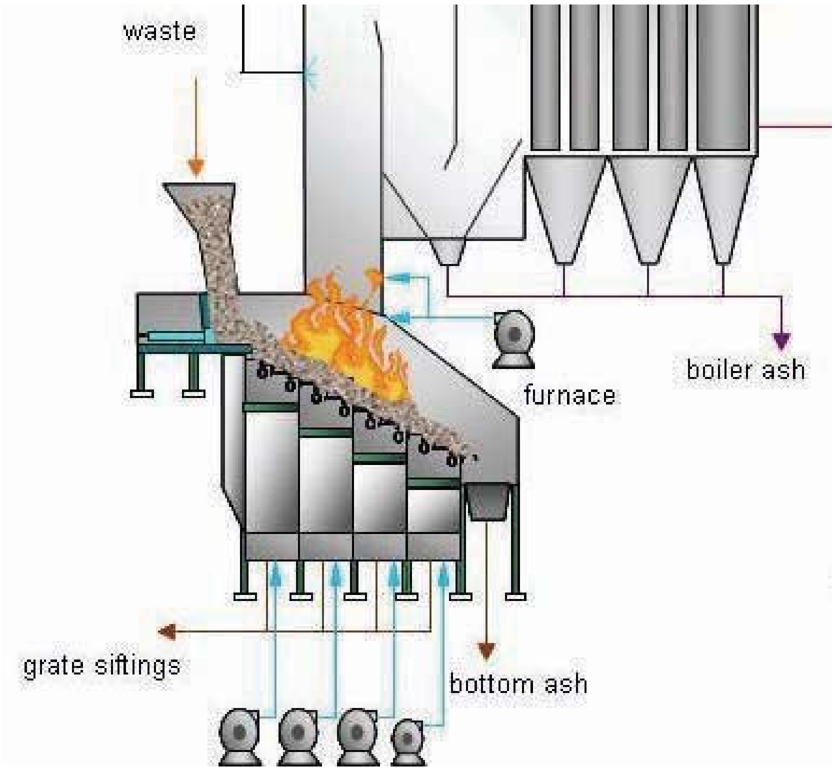

Figure (I.10) - Grate incinerator for domestic waste burning.

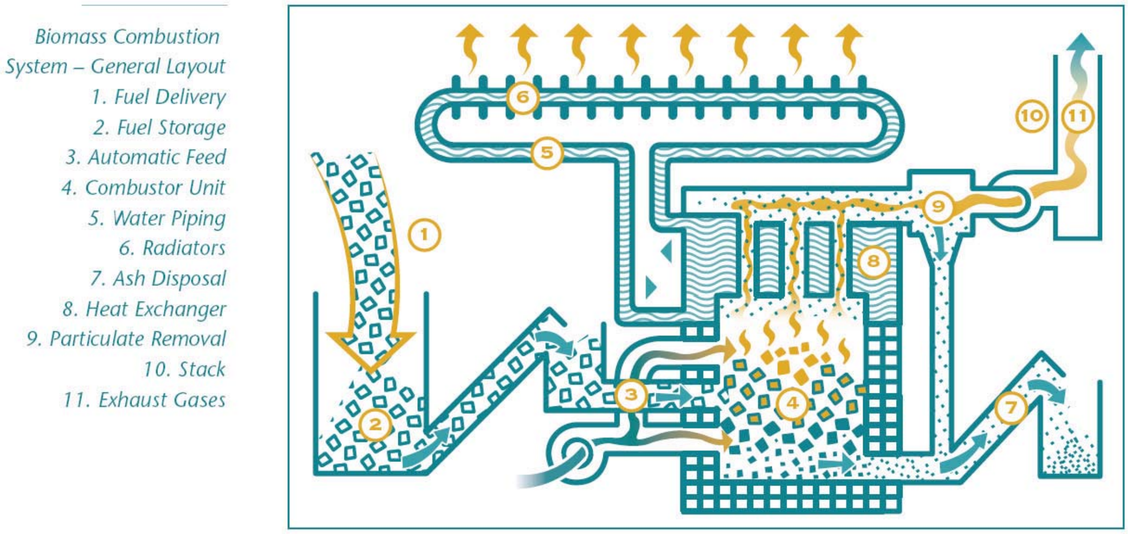

Figure (I.11) - Schematic of biomass combustion process.

The propagation of a combustion front in a reactive porous medium has a plurality of application and each one with its particular challenge. However, the investigation of each one of this phenomena show us some common aspects of the propagation of combustion front.

I.3 Combustion front propagation

As seen previously, the propagation of a combustion front occurs in a variety of situations and for different purposes, such as waste incineration, in-situ combustion or burning of solid fuels for other industrial applications. Description of the combustion front propagation in a reactive porous medium remains a challenge to science in terms of physicochemistry, and heat/mass transfer.

According to (Hobbs, Radulovic and Smoot 1993), the first great research effort in combustion front propagation dates from 1977 and 1979. Since then, familiar environmental problems and the search for alternative energy sources have motivated greater research on the subject. These efforts have focused on determining which parameters influence the progress and structure of a combustion front. To this effect, some authors have developed numerical models and experimental devices.

The present work focuses on the propagation of a combustion front in a reactive porous medium, (Hobbs, Radulovic and Smoot 1993) and (Fatehi and Kaviany 1994). In this type of problem, the solid phase reacts with the gas phase; chemical reactions occur, such as pyrolysis of the solid and further oxidation of the residual carbon, accompanied by extreme changes in physical structure of the solid phase. (Hallett 2005) proposed a scheme to illustrate these simultaneous complex processes, Figure (I.12).

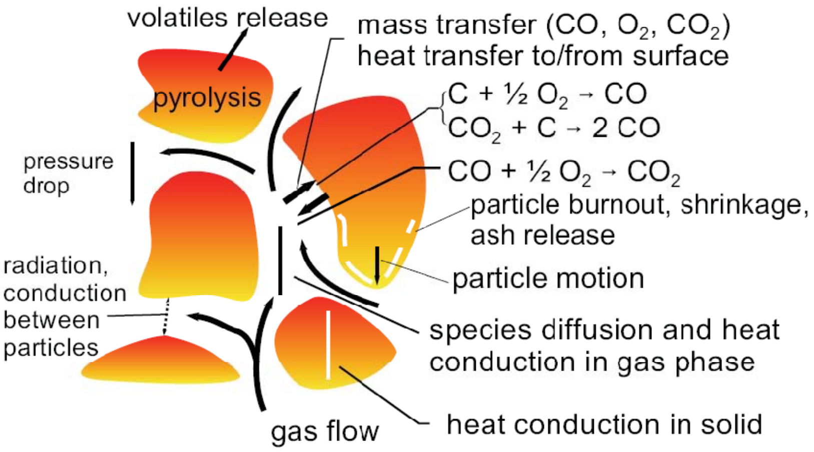

Figure (I.12) - Coupled phenomena of heat and mass transfer, flow and chemical reaction in a reactive porous medium.

In all the applications mentioned above it is possible to distinguish three global zones, Figure (I.13).

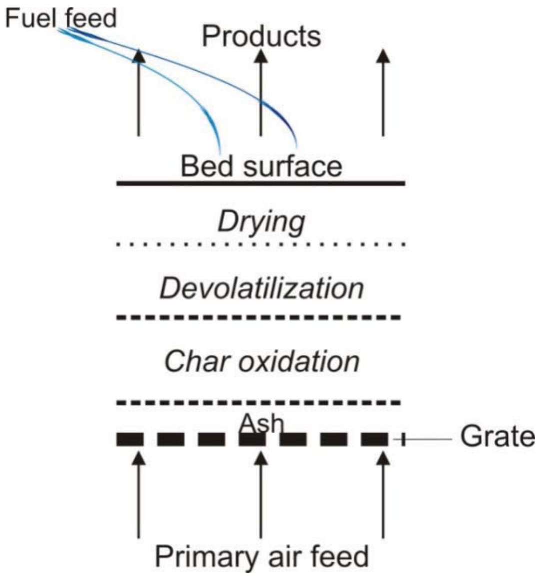

Figure (I.13) - Reactions zones

The each zone is characterized by one important step in process of conversion of the fuel. The processes inse three zones are commented below:

a) Drying zone: solid fuel is introduced into the reactor. As a result of heat transfer from the parts of the reactor, drying of the solid fuel occurs.

b) Pyrolysis Zone: at temperatures above 250 °C, the solid fuel starts pyrolyzing. The large molecules break down into medium size molecules and carbon (char).

c) Oxidation Zone: a burning (oxidation) zone is formed at the level where oxygen (air) is introduced. Reactions with oxygen are highly exothermic and result in a sharp rise of the temperature up to 1200 - 1500 °C.

Specifically for the oil shale, (Debenest 2003) proposed four main zones from since the entry to exit of the bed, Figure (I.14):

1. The entry zone, where the fuel is almost consumed, and where the temperature is insufficient to maintain any chemical reaction. The air that flow through this zone is preheated by the bed and carries heat in reaction zone.

2. The pyrolysis zone, downstream the reaction front, where the temperature reached a sufficient value to crack organic matter from the grains. This cracking produces

gaseous species (light hydrocarbons). The pyrolysis process is endothermic.

3. The reactions zone, where the temperature is high and where oxygen carried by the fluid meets the carbon residue left by pyrolysis. The oxidation reaction is exothermic, consumes oxygen and produces gaseous species (CO and CO2).

4. The last zone, where the porous medium has not received heat and where the flow moves and involving gaseous species, which traverse it without interact with the solid matrix.

Those zones were created by the reactions. The mechanism of oil shale combustion has not been studied in detail in literature. Most of the previous works are focused on the combustion of carbon, char, coke, devolatilized coal and coal particles. However, the oil shale combustion is complicated by several reactions, which include both organic and inorganic types.

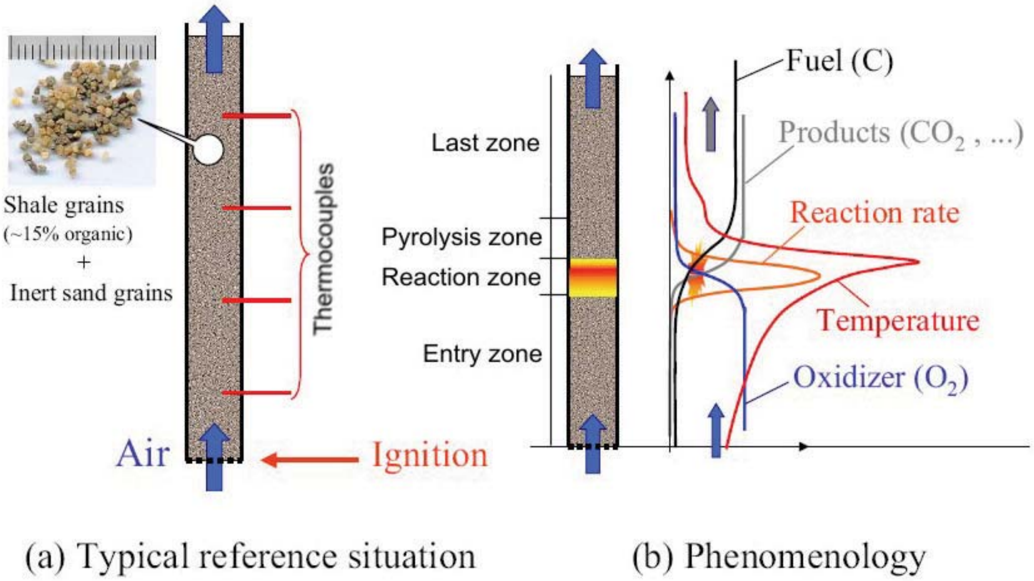

Figure (I.14) - Reaction zones in crushed oil shale bed

Among the various solid fuels, coal, MSW and other biomass, the oil shale present an intermediate difficulty level. From the chemical point of view, oil shales are more complex than coal, but simpler than MSW. The oil shale contains organic compounds, which are not well characterized, and devolatilization reactions coexist with oxidation reactions during heating. On the other hand, the presence of a significant fraction of inert matter in rock induces a major simplification - the bed geometrical structure is only marginally affected by the smoldering process, unlike for example the coal, which contains a small portion of non heat-degradable material, and undergoes a drastic shrinkage.

(Debenest 2003) proposed three reactions to represent oil shale decomposition in a fixed bed. As seen previously, the chemical composition of oil shale is very complex, often misunderstood, variable depending on their origin. The chemical processes involved include many stages and different species.

$$\mathrm{ker}ogen + heat \rightarrow C_{(s)} + volatile \qquad \text{r. 1}$$

$$C_{(s)} + O_2 \rightarrow CO_2 + heat \qquad \text{r. 2}$$

$$CaCO_3 + heat \rightarrow CaO_{(s)} + CO_2 \qquad \text{r. 3}$$

The kerogen is converted into fixed carbon and volatile gases. Fixed carbon is then oxidized into CO_2, and calcite into CO_2.

I.3.1 Co-current and counter-current configurations

The propagation of a combustion front can occur in two elementary combustion situations:

- Counter-current combustion (or opposed combustion), where ignition front and feed of primary air occur on opposite sides of the fuel batch, Figure (I.15-a). The counter-current air supply is normally found in fixed-bed combustion processes. The typical application of counter-current combustion is the incineration of MSW [(Ryu, *et al.* 2006), (Yang, Ryu, *et al.* 2005a), (Yang, Ryu, *et al.* 2005b) and (Khor, *et al.* 2007)].

- In second case, Figure (I.15-b), co-current combustion (or forward combustion), both combustion front and feeding of primary air, take place on the same side of the combustion cell [(Wang, Chao and Kong 2003), (Thunman and Leckner 2003) and (Bar-Ilan, Rein, *et al.* 2004)].

This last case is investigated in this work. The best example of co-current combustion can be found in-situ combustion for oil recovery [(Castanier and Brigham 2003) and (Akkutlu and Yortsos 2003)].

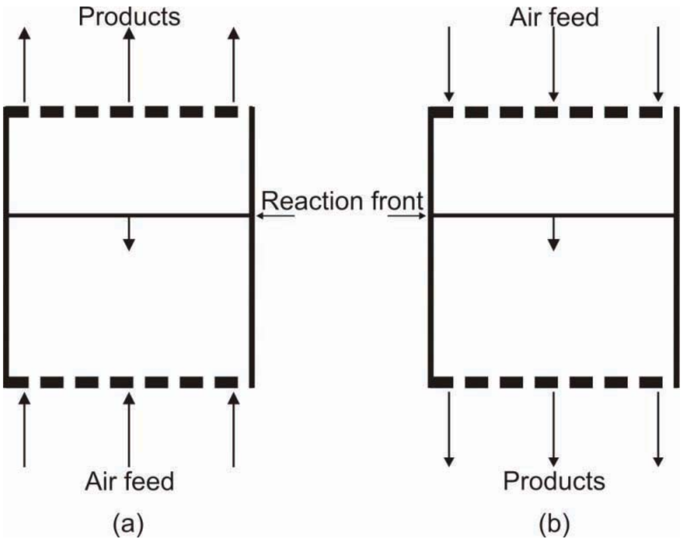

Figure (I.15) - Arrangements: (a) counter-current, (b) co-current.

I.3.2 Reactions zones thickness

As seen in previous topic, the front contains three elementary zones that can be distinguished, and the investigation about its chemical structure have been investigated by [(Bousaid 1987), (Fatehi and Kaviany 1994), (Yang, Yamauchi, *et al.* 2003) and (Rein, *et al.* 2006)] using a numerical model.

(Fatehi and Kaviany 1994) cite: "the front thickness was defined as the length of the medium across which the reaction rate was equal or greater than 1/10 of its maximum value". The thickness of the front increases linearly with air pore velocity.

(Yang, Yamauchi, *et al.* 2003) inir work on MSW and wood chips combustion, defined the reaction zone thickness as the physical distance in flame front where the bed temperature rises from 30 °C to the peak value. They found that this thickness is almost an inversely linear function of the moisture level. The reaction zone thickness ranges from 20 to 50 mm for wood chips and MSW.

For drying zone and devolatilization, (Yang, Ryu, *et al.* 2005b) demonstrated the moisture evaporation rate distribution inside the bed as a function of time for the particle diameter between 10 and 35 mm. For the 10 mm particle size, evaporation zone lies about 50 mm below the bed top and the zone extends 70 mm downward. The devolatilization zone moves away from the bed top as the combustion proceeds and reaches a maximum 40 mm below the bed top line.

(Rein, *et al.* 2006) studied the front structure of forward smolder and opposed smolder in polyurethane foam. For the forward smolder, the pyrolysis front arrives first to the virgin foam and is then followed by the oxidation front.

As far as the structure of the combustion front in an oil shale crushed bed is concerned, only one little literature is available.

(Bousaid 1987) in his work about in situ combustion, says that the front thickness dependent on pressure and temperature. The front thickness increases as the reaction temperature increases.

(Debenest, Mourzenko and Thovert 2005a) during an experiment, a reaction front propagates upwards. They could follow visually the front progress, with a glowing layer about 3 times the particle diameter.

I.3.3 Smoldering combustion and flaming

Another challenge remaining is to establish what is actually oxidizing during the propagation of a combustion front: the solid residue after devolatilization only or also part of the volatile matter?

Smoldering is a slow, low-temperature, flameless form of combustion, sustained by the heat evolved when oxygen directly attacks the surface of a condensed-phase fuel. The propagation of a combustion front can also involve phenomena related to the ignition of a homogeneous gas phase reaction that is induced by a heterogeneous surface reaction (smolder) that acts both as the source of gaseous fuel (pyrolyzate, CO, etc.) and the source of heat to initiate the homogeneous reaction, this situation is called flaming. Thus, an important event can occur and affect the form of the combustion front, the transition from smoldering to flaming. The transition is more likely to occur when the heat released by the reactions (heterogeneous reaction and homogeneous gas phase reaction) is larger than the heat losses to the surrounding environment (Bar-Ilan, Putzeys, *et al.* 2005). This author presents an experiment where the smolder propagation and the transition to flaming are assisted by reducing heat losses to the surroundings and increasing the oxygen concentration.

(Ohlemiller 1985) reported that the char oxidation is the principal heat source in most self-sustained smolder propagation processes; the potential for smoldering combustion thus exists with any material that forms a significant amount of char during thermal decomposition. He presented experimental characteristics of smolder propagation from seven different references. The smolder velocity for vegetable fiber board in natural convection was 0.25 cm min^{-1}; for rolled paper, also in natural convection, it varied from 0.3 to 0.5 cm min^{-1}. Cigarettes of tobacco shreds 0.8 cm diameter in intermittent natural convection and forced draw (30 cm s^{-1}) presented a smolder front velocity of 0.27 cm min^{-1}. Ohlemiller also reported that depending on the material, the transition from smolder to flaming in bed occurred at airflow velocities above about 0.9 to 1.7 m s^{-1}. For these materials, flaming did not develop when the mean particle size was less than 1 mm.

The configuration in which transition from smoldering to flaming is more likely to occur is in forward combustion. Thus, the oxidizer reaches the reaction zone after passing through the hot char left behind by the propagating smolder reaction, and the transition to flaming may occur by vigorous oxidation of this char; the transition has strong links with the highly exothermic char and residue (secondary char) oxidation reactions [(Bar-Ilan, Putzeys, *et al.* 2005) and (Rein, *et al.* 2006)].

I.3.4 Pore-scale problems

When the medium is examined in small scale, questions in relation to the different phases present in medium can appear:

(i) One of them is if the temperatures of the gas phase and solid phase within porous are locally the same, i.e. the gas and solid are in *local thermal equilibrium*. When this condition occurs, a single temperature can be used to describe a heat transfer process in a multiphase system [(Whitaker 1991) and (Quintard and Whitaker 1995)]. *Thermal non-equilibrium* implies that there is a temperature of difference between the phases [(Quintard and Whitaker 1993) and (Batsale, Gobbe and Quintard 1996)]. This is believed to be one of the major causes of the discrepancy between model predictions and experimental results.

(ii) Concerning the chemical processes in porous medium combustion, (Oliveira and Kaviany 2001) reported that these processes have different phenomenological length and time scales resulting in different transport and reaction regimes, and leading to thermal and chemical non-equilibria. In Figure (I.16) by (Oliveira and Kaviany 2001) are described three situations: smoldering combustion, solid and condensed-phase combustion synthesis and gasless combustion synthesis.

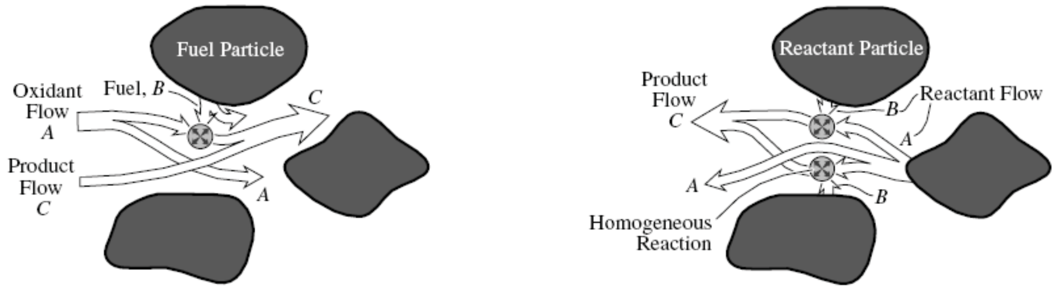
(c) Homogeneous Reaction with Transport Controlled Fuel Supply

(d) Homogeneous Reaction with Transport Controlled Oxidant and Fuel Supply

(e) Homogeneous and Heterogeneous Reaction with Transport Controlled Oxidant Supply or Product Removal

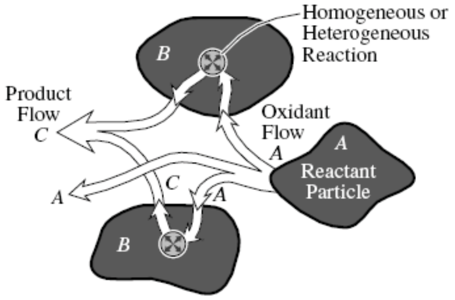

Figure (I.16) - Distribution and transport of reactants in chemical nonequilibrium processes.

- Figure (I.16-c) presents the case in which the fuel is provided from the pyrolysis of the solid, as in solid combustion or smoldering. In this case, called *homogeneous reaction with transport controlled fuel supply*, the rate of pyrolysis may control the reaction. The reaction could also occur inside the solid phase (not depicted) and controlled by the transport of oxidizer or products.

- Another case, Figure (I.16-d), is called homogeneous reaction with transport controlled oxidant and fuel supply. Here both the reactants come from the solid particles (of different materials), with the reaction occurring in gas phase. The reactants mixing may be controlled by the rates of generation or by mass transfer.

- Finally, the case called homogeneous and heterogeneous reaction with transport controlled oxidant supply or product removal, Figure (I.16-e). In this case, the reaction occurring inside one of the reactant particles. The reactants mixing are controlled by the transport in pore space (by diffusion or capillarity) and within reactant B particle (by diffusion). The product may be in solid phase, growing around the reactant B particle, or in liquid phase, later nucleating and growing as a solid phase.

There are some cases where a mix these situation occur. To better control the geometry of the medium and the processes occurring there, a fundamental understanding of the interaction among the various processes and scales is needed.

In traditional combustion applications such as a flame, the peak temperature inside a combustion zone is directly related to the energy content of the unburned air/fuel mixture. The theoretical maximum temperature is predicted by the chemical equilibrium of an adiabatic process and is thus called the adiabatic equilibrium temperature. However, in some configurations, heat is transferred from the hot combustion products to preheat the unburned air/fuel mixture, which produces peak temperatures that can exceed by far the adiabatic equilibrium temperature, thus the term “Superadiabatic” combustion [(Babkin, *et al.* 1983) and (Aldushin 1993)]. Superadiabatic temperatures have been observed earlier in a combustion zone propagating in a packed bed of solid fuel (Pinjala, Chen and Luss 1988). This temperature augmentation is due to the large interstitial surface area of the porous media which allows for highly effective heat transfer between the filtrated gas and the reticulated solid (Howell, Hall and Ellzey 1996).

I.3.5 Heat and mass transfer in porous medium

(Hobbs, Radulovic and Smoot 1993) made a brief description of qualitative physical and chemical processes that occur during the fixed-bed combustion.

The description of the heat and mass transfer interaction between gas and solid phase, and between particles themselves are decrypted in Figure (I.17), as follows:

1. Conduction through solid particles;
2. Conduction between the solid particles in contact;
3. Radiation between the solid particles;
4. Convection from the solid particles to the fluid;
5. Radiation from the solid particles to the fluid;
6. Conduction through fluids;
7. Radiation through fluids;

8. Fluid mixing;
9. Conduction from the solid particle to the wall of the reactor;
10. Radiation from the solid particle to the wall of the reactor;
11. Convection from the solid particle to the wall of the reactor;
12. Radiation from fluid to the wall of the reactor;

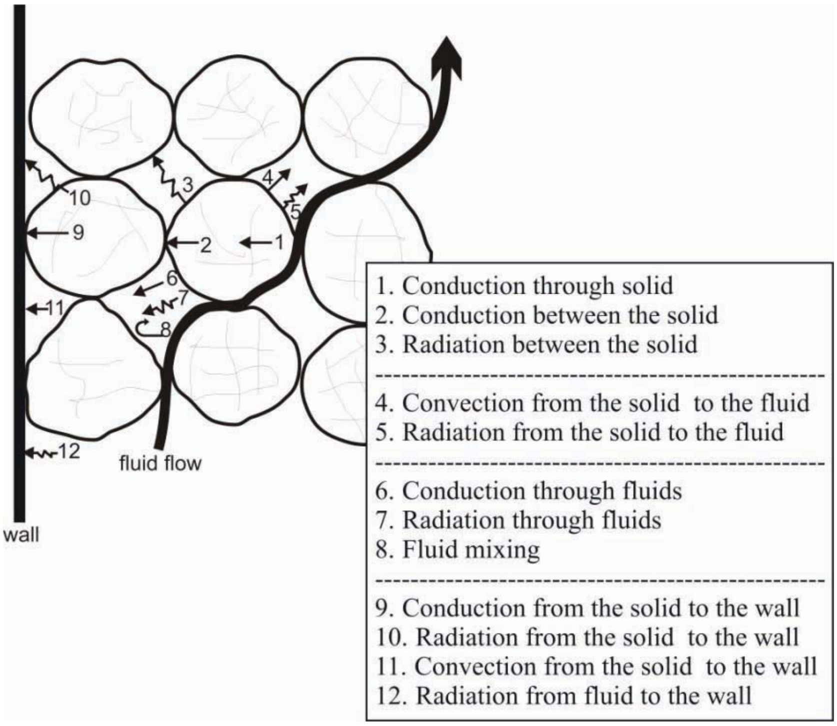

Figure (I.17) - Iterations intra and inter phases, adapted from (Hobbs, Radulovic and Smoot 1993).

I.3.6 Flow in porous medium

This process is coupled with heat and mass transfer. From the point of view of physical problem, the process is of great interest and it has a large number of practical applications in many fields of science. Most often mentioned is the relation to the oil industry where the flow of oil, gas and water in reservoirs are of great technological importance.

In relation to flowing, porous medium consists of a matrix with a large amount of microscopic pores and throats which are typically narrow tubes where fluid can pass through. The description of flow in porous media is extremely difficult because of the complexity of the medium. There are two important quantities describing the properties of a porous medium: the porosity ε and the permeability κ. The porosity of a porous medium is defined as pore volume/ matrix volume, Figure (I.18). Where the pore volume denotes the total volume of the pore space in matrix and the matrix volume is the total volume of the matrix including the pore space. Thus, $0 \le \varepsilon \le 1$. Often the porosity can be chosen as constant for the whole medium.

The permeability κ describes the ability of the fluid to flow through the porous medium and depending on the geometry of the medium. For porous media composed of granules that are not spherical, the average granule diameter, dp, can be taken as:

$$dp = 6\, A_p /\ V_p \qquad \text{(I.1)}$$

where A_p and V_p are the surface area and the volume of the granule, respectively.

The fluid flow through a porous medium can be described by the phenomenological Darcy equation, eq. . Then the velocity "*U*" of the fluid trough the medium is given by Darcy's equation:

$$\vec{U} = -\frac{k}{\mu}\left(\vec{\nabla} P - \rho\, \vec{g}\right) \qquad \text{(I.2)}$$

where "μ" is the fluid viscosity, ∇P is the pressure gradient across the matrix, "g" denotes the acceleration due to the gravitational forces and "ρ" is the density of the fluid.

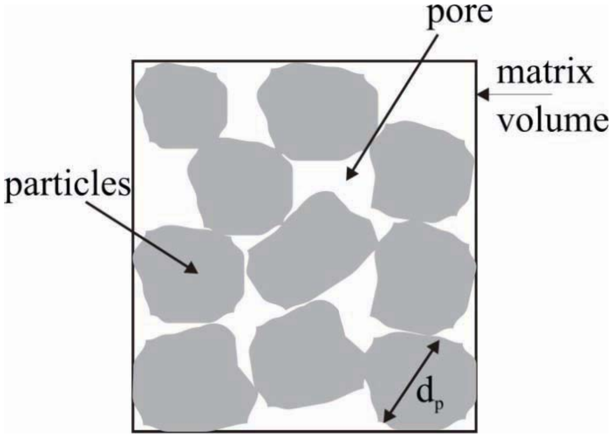

Figure (I.18) - Porous medium representation

To investigate the combustion front propagation in its various situations, several experimental devices were developed. The next topic will present some of them, to highlight the possibilities of such experiment and the difficulties encountered.

I.4 Review of the experimental works in a fixed bed

Only a handful of experimental works on co-current combustion have been carried out until now. (Wang, Chao et Kong 2003) presented an experimental study of smoldering combustion in horizontally forced forward condition. Two cases are considered: one is adiabatic smoldering, where no heat is lost to the environment, and the other one is non-adiabatic smoldering combustion, where convective heat losses to the environment through the walls of the cell are taken into account. For the adiabatic case, it was shown that the smoldering propagation rate and the smoldering temperature both increase with the flow rate of air. Results from the non-adiabatic analysis showed a similar trend.

The experiments in co-current and counter-current combustion were studied by (Thunman and Leckner 2003). The work is focused on differences between the co-current and the counter-current arrangements. Thus, were investigated the effect of time to ignition, total time of conversion, position of the different phases of the conversion (drying, devolatilization and char combustion) in time and along the height of the bed.

(Vantelon, *et al.* 2005) made an experimental study on the forward combustion of a bed of tires and refractory briquettes. The author found that the combustion process is influenced by the airflow rate through the reactor. An oxygen limit combustion reaction moves from a rate-limited regime to a heat transfer-limited regime. The rate-limited regime is characterized by high production of residual oil and low propagation velocities. The heat transfer-limited regime reduces the production of oil, but it results in a much faster conversion of the fuel. Two other different regimes are also observed as a function of the mass fraction of tires.

- For mass fractions of tires less than 70 %, the final tire conversion rate and temperature are proportional to the mass fraction of tires. In this regime the volumetric energy density dominates the combustion process.
- For a mass fraction of tires greater than 70 %, the conversion rate is independent of the amount of fuel and it is initially much slower than for lower

fuel concentrations. These two regimes could be described in a qualitative manner by a simple energy balance.

With regard to the case of counter-current combustion, several experimental devices have been developed for the investigation of combustion front propagation and structure. Although this configuration will not be studied here, its results may be interesting for the present work.

The effects of various solid fuel properties and operating conditions on the ignition and burning rates have been reported in literature for different authors.

(Gort, Valk et Brem 1995) studied the influence of the superficial air velocity and moisture content on three fuels: coke, wood and shredded municipal waste. The experiments were carried out in a laboratory grate furnace. He suggested three reaction regimes:

(i) partial gasification where, after oxygen depletion, there is still some solid material left, which might be partially consumed by gasification by H_2O and CO_2;

(ii) complete gasification where air flow rate is high enough to convert all ignited material, but there is not enough oxygen available for complete combustion of unburnt gases;

(iii) combustion regime where initially some CO is observed, but this is oxidized quickly. Concentrations fluctuate strongly. The reaction layer is thin.

(Shin and Choi 2000) proposed a similar concept on the counter-current propagation of a combustion front. The combustion of solid fuel in a fixed bed was investigated using one-dimensional experiments. The effects of air supply rate, fuel particle size, and the calorific value are discussed. Two modes of combustion in bed can be distinguished, based on the availability of oxygen. They proposed a schematic, Figure (I.19), to show how the combustion depends on the air supply rate.

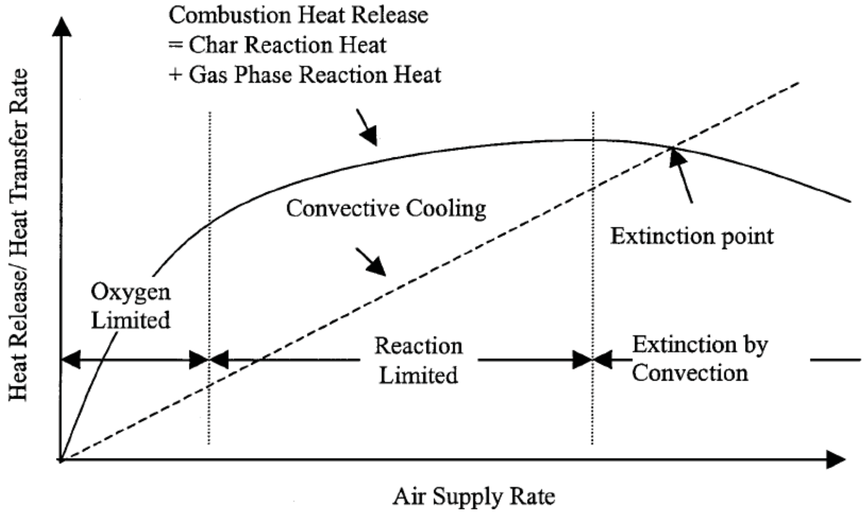

Figure (I.19) - Effect of air supply rate on the combustion of a bed

- *oxygen-limited* combustion: At low rates of air supply, the oxygen is completely consumed by the char and the reacting volatile material. In this case, the reaction rate of the fuel is determined by the oxygen supply rate.

- *reaction-limited* combustion: If the air supply is increased, combustion is further enhanced, but the limit of the combustion rate of the bed material causes an increased oxygen concentration at the exit. In this case, the reaction rate cannot increase further owing to the limit of the reaction rate and the increased convective cooling by the air.

(Saastamoinen, *et al.* 2000) studied the effect of the air flow rate, moisture, particle size, density, and wood properties on the ignition front velocity, and the maximum temperature in bed, and interpreted by a quasisteady- state modeling.

[(Thunman et Leckner 2005), (Yang, Ryu, *et al.* 2005a) and (Ryu, *et al.* 2006)] identified two distinct periods using the measurements of temperature, gas composition and mass loss histories: *ignition propagation period* and *char oxidation period*. During the *ignition propagation period*, the mass of the bed decreases with a constant slope. Then, the mass loss slows down as the *char oxidation period* commences.

[(Yang, Yamauchi, *et al.* 2003), (Yang, Sharifi and Swithenbank 2004), (Yang, Ryu, *et al.* 2005a), (Yang, Ryu, *et al.* 2005b) and (Ryu, *et al.* 2006)] investigated the effect of air flow rate, moisture and fuel devolatilization rate on the ignition rate and other parameters for combustion modeling of simulated wastes and biomass.

(Liang, *et al.* 2008) reported another important aspect concerning the heterogeneity of the composition of the solid particles. For the sample extracted in different parts of corn straw, the concentration of CO and NO are clearly different. According to the author, corn straw combustion occurred in two stages: ignition front propagation and char oxidation. Both stages were identified by [(Thunman et Leckner 2005), (Zhou, *et al.* 2005) and (Ryu, *et al.* 2006)] previously mentioned.

All work cited previously use a vertical cylinder with internal diameter between 15 cm and 24.4 cm and a height of chamber between 30 cm and 150 cm, and all surround with a thickness of insulating materials. The temperature measurements are carried out using thermocouples placed at the axis and at different heights. The mass of the bed is sometimes measured using a weighing scale. The flue gases are analyzed commonly at the cell exit.

The French Standards Association (AFNOR) published the standard NF M03-049, which deals with characterization of solid combustibles in a fixed bed in counter-current flow. The norm is based on the measurement of front velocity, combustion rate, pressure drop and temperature. According to the norm, the reactor should preferably have a cylindrical shape with a diameter of not less than 25 cm, in order to avoid excessive influence of the wall on the results.

I.5 Review of the oil shale characterization using thermal analysis

This section is dedicated to oil shale characterization methods using the most common thermal analysis method: ThermalGravimetric Analysis (TGA) and Differential Scanning Calorimetriy (DSC). Today, a lot of works about it are available [(Ziyad, Garnier and Halim 1986), (Chanaa, Lallemant and Mokhlisse 1994), (Kök et Pamir 1995), (Kok and Pamir 1998), (Kok, Sztatisz and Pokol 1999), (Jaber and Probert 1999), (Williams and Ahmad 1999), (Kök and Pamir 2000), (Bruan, *et al.* 2001), (Saoiabi, Doukkali, *et al.* 2001a), (Saoiabi, Doukkali, *et al.* 2001b), (Sadiki, *et al.* 2003), (Sonibare, Ehinola and Egashira 2005), (Kök, Guner and Bagci 2008)]. These methods are commonly used to determine the global composition of oil shale and kinetics of oil shale degradation reactions, as well the influence of heating rate on the pyrolysis and oil yield in oil shale samples.

(Taulbee, *et al.* 1982) investigated oil shale samples in a thermogravimetric analyzer in relation to heating rate in range of 4.0–55 K min^{-1}. Higher heating rate resulted in oil being evolved at higher average temperatures; hence a smaller fraction of the oil is found in liquid phase. Oil in liquid phase is subjected to two competing processes: vaporization, which leads to oil production, and coking, which leads to a carbonaceous residue.

(Nazzal 2002) studied oil shale samples in a thermogravimetric analyzer also in relation to heating rate. The oil shale was crushed to a grain size of 1.32–3.33 mm and dried at 105 °C. He reported that the oil yield was increased as the heating rate was increased from 2 to 10 K min^{-1}. Increasing the heating rate up to 30 K min^{-1} caused a slightly reduction in oil yield. Increasing the heating rate from 2 to 30 K min^{-1} also caused a slight increase in evolved gas. This indicates that heating rate played a small role in gas evolution under both pyrolysis atmospheres (oil pyrolyzed under nitrogen and nitrogen/steam).

(Barkia, Belkbir and Jayaweera 2004) studied the influence the heating rates using four values ranging from 5 to 40 K min^{-1}. Thermal decomposition started at 200 °C and reached a maximum rate at around 420 °C for the slowest heating rate, moving to higher temperatures with increasing heating rate. The total organic matter (low- and high-volatile hydrocarbons plus residual carbon) in oil shale for each heating rate was determined after heating all samples in nitrogen flowing atmosphere to 500 °C and keeping for 1h at this temperature. Air was then introduced to obtain quantity of organic carbon remaining in shale. The activation energies were also determined using the Coats-Redfern method. Results show a change in reaction mechanism at around 350 °C. Below this temperature, the activation energy was 41.3 kJ mol^{-1} for the decomposition of Timahdit, and 40.5 kJ mol^{-1} for Tarfaya shale. Above this temperature the respective values are 64.3 and 61.3 kJ mol^{-1}. Still concerning the determination of kinetics parameters, (Barkia, Belkbir et Jayaweera 2006) carried out experiments using the residual carbons (fixed carbon) from kerogen extracted from two Moroccan oil shales (from Timahdit and Tarfaya), where the samples were oxidized in air. The oxidations were studied by isothermal thermogravimetry. Several kinetic models for mechanisms of the reactions were tested to fit the experimental data. Oxidation of the fixed carbon derived from Timahdit oil shale followed a two-third order reaction with activation energy of 58.5 kJ mol^{-1}, whilst that from Tarfaya oil shale was a half order reaction with activation energy of 64.1 kJ mol^{-1}.

(Kök and Pamir 2000) reported that the thermogravimetric analysis of oil shale samples has been extensively used as a means of determining the characteristics of devolatilization and the related kinetic parameters. Thermal methods providing information about net results of mass loss and calculation of kinetic parameters are based on simplifying assumptions. In another paper, (Kok and Pamir 1998), they used differential scanning calorimeter (DSC) to determine the combustion kinetics of three oil shale samples by ASTM and Roger & Morris methods. On DSC curves two reaction regions were observed on oil shale sample studied. In DSC experiments higher heating rates resulted in higher reaction temperatures and higher heat of reactions. Distinguishing peaks shifted to higher temperatures with an increase in heating rate. Activation energies were 18.5-48.8 kJ mol^{-1} for Rogers & Morris method.

(Cinar, Castanier and Kovscek 2008) developed an iso-conversional methods of crude oil reaction kinetic analysis, to provide a model-free procedure to find activation energy as function of conversion. The method developed was applied to in-situ combustion kinetics. They observed two reactions during combustion of oil in porous media: low temperature oxidation (LTO), where are produced of little or no carbon oxides and high temperature oxidation (HTO), where the reactions are heterogeneous and include reactions of oxygen with fuel producing carbon oxides and water. The activation energy for both LTO and HTO were determined. These both reactions were also observed the some previous work [(Barkia, Belkbir and Jayaweera 2004), (Barkia, Belkbir et Jayaweera 2006), (Kok and Pamir 1998), (Kok, Sztatisz and Pokol 1999) and (Kök, Guner and Bagci 2008)].

I.6 Numerical models background

On the other hand of the experimental devices, one can find a numerous works dedicated to the numerical study of the combustion process, in both co-current and counter-current situations.

I.6.1 Numerical models

The numerical models can be divided in macroscale and microscale models.

Macroscale models

Models at macroscale [(Ohlemiller 1985), (Kiehne, Wilson and Matthews 1990), (Moallemi, Zhang and Kumar 1993), (Fatehi and Kaviany 1994), (Akkutlu and Yortsos 2003), (Oliveira and Kaviany 2001), (Biyikoglu and Sivrioglu 2004), (Yang, Sharifi and Swithenbank 2004), (Zhou, *et al.* 2005), (Ryu, *et al.* 2006), (Rein, *et al.* 2006)] enable numerical simulations at the Darcy-scale, i.e. a description as a continuous medium of the effective properties (conductivity, heat capacity) and averages variables (temperature, concentrations). The various effective parameters involved, when applicable, are by no means trivial, and their validity is an open question in many cases.

The classical approach is the principle of local volume average temperature, described by (Whitaker 1977) and (Kaviany 1995). Considering the case of isotropic porous medium, where the radiation effects, the viscous dissipation and the work accomplished by changes on the pressure field are neglected, the energy conservation equations to solid (*s*) and fluid (*f*) phases are given by:

$$(\rho C_p)_s \frac{\partial T_s}{\partial t} = \nabla.(K_s \nabla T_s) + h_c(T_s - T_f) + \ddot{q}_s \qquad (I.3)$$

$$(\rho C_p)_f \frac{\partial T_f}{\partial t} + (\rho C_p)_f \vec{V}.\nabla T_f = \nabla.(K_f \nabla T_f) + h_c(T_f - T_s) + \ddot{q}_f \qquad (I.4)$$

Cp is the specific heat; *K* is the thermal conductivity; *q* is the heat generation term per unit volume.

Based on local volume averaging, (Whitaker 1977) and (Kaviany 1995) the eq. (I.3) and (I.4) can be written as:

$$(1-\varepsilon)(\rho C_p)_s \frac{\partial \langle T_s \rangle}{\partial t} = (1-\varepsilon)\nabla.(K_s \nabla \langle T_s \rangle) + (1-\varepsilon)\left[\langle \ddot{q}_s \rangle + h_c\left(\langle T_s \rangle - \langle T_f \rangle\right)\right] \qquad (I.5)$$

$$\varepsilon(\rho C_p)_f \frac{\partial \langle T_f \rangle}{\partial t} + \varepsilon(\rho C_p)_f \vec{V}.\nabla \langle T_f \rangle = \varepsilon\nabla.(K_f \nabla \langle T_f \rangle) + \varepsilon\left[\langle \ddot{q}_f \rangle + h_c\left(\langle T_f \rangle - \langle T_s \rangle\right)\right] \qquad (I.6)$$

where ε is the porosity and $<T_{s,f}>$ represents the local volume averaged temperature to solid and fluid, respectively.

- Assuming that there is a perfect contact between solid and fluid phases, one can make the hypothesis of local thermal equilibrium between the phases:

$$\langle T_f \rangle = \langle T_s \rangle = \langle T \rangle \qquad (I.7)$$

Adding the eq. (I.5) and (I.6) and using the eq. (I.7) gives:

$$(\rho C_p)_{eff} \frac{\partial \langle T \rangle}{\partial t} + \varepsilon(\rho C_p)_f \vec{V}.\nabla \langle T \rangle = \nabla.(K_{eff} \nabla \langle T \rangle) + \langle \ddot{q}_{eff} \rangle \qquad (I.8)$$

where:

$$(\rho C_p)_{eff} = (1-\varepsilon)(\rho C_p)_s + \varepsilon(\rho C_p)_f \tag{I.9}$$

$$K_{eff} = (1-\varepsilon) K_s + \varepsilon K_f \tag{I.10}$$

$$\langle \ddot{q}_{eff} \rangle = (1-\varepsilon)\langle \ddot{q}_s \rangle + \varphi \langle \ddot{q}_f \rangle \tag{I.11}$$

are respectively, the overall thermal capacity (effective) per unit volume, the overall thermal conductivity (effective) and global heat generation per unit volume of the medium.

To simplify the analysis other assumptions were proposed by (Schult, *et al.* 1995):

a) radiation heat transfer is modeled by a diffusion approximation;

b) the solid phase is stationary and non deforming;

c) Fick's law describes the diffusion of oxidizer through the gas with the quantity $D_{\rho g}$ (gas diffusivity) constant;

d) the flow resistance through the porous sample is small enough that pressure is essentially constant;

e) the sample is sufficiently long that end effects are negligible and do not influence the transport of heat or oxidizer;

f) the activation energy of the reaction involved during combustion is large;

- Under certain circumstances, the local average temperature assumption appears to be too restrictive and fails to be valid. This leads to macroscopic models which are referred to as non-equilibrium (Quintard and Whitaker 1993) and (Batsale, Gobbe and Quintard 1996). It is possible to develop separate transport equations for each phase writing a monodimensional system equation including:

    - two equations for energy (one for solid and another for fluid);
    - an equation for the conversion rate of fuel;
    - two equations for the mass conservation (oxidant and fuel);
    - an equation governing the gas flow;

- a few other thermodynamic equations.

Microscale models

To answer some questions, by examining the details of the processes, some numerical simulation tools based on a microscopic scale were developed by [(Lu and Yortsos 2005), (Oliveira and Kaviany 2001), (Debenest, Mourzenko and Thovert 2005a) and (Debenest, Mourzenko et Thovert 2005b)]. Here, the local equations are solved in a detailed discretized image of the microstructure and make it possible the investigation of situations that cannot be properly described by macroscale models.

The scheme in Figure (I.20) is a zoom on a microstructure and summarizes the different mechanisms considered by (Debenest 2003).

The gas flow path between grains of the bed carries all chemical species and heat. The heat is also conducted in solid phase. The combustion is supposed to be a heterogeneous reaction on the surface of grains and pyrolysis does not happen in this reaction area. The fixed carbon content in grains is supposed to sell out upstream of the reaction front, as well the oxygen concentration downstream of the front.

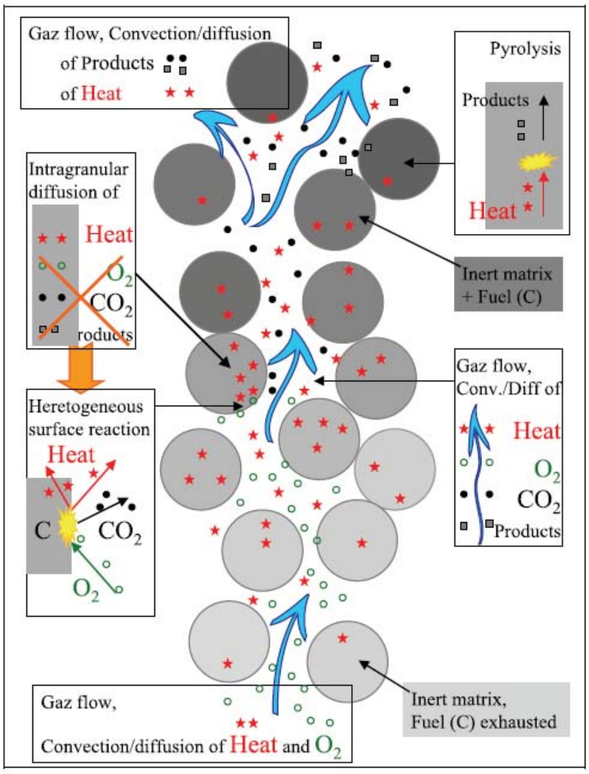

Figure (I.20) - Close-up of the bed microstructure, and illustration of the mechanisms included in microscopic formulation of the problem.

I.6.2 Simple analytical solutions

Using a one-dimensional single-temperature model, approximate analytical expressions can be obtained for determination of the front propagation velocity and the maximum temperature at the combustion front [(Schult, *et al.* 1995), (Aldushin, Rumanov and Matkowsky 1999), (Debenest 2003)]. This analytical solution is based on a series of hypotheses proposed by (Schult, *et al.* 1995).

The concentration of oxygen is characterized by values upstream and downstream from the front, $[O_2]_{in}$ and $[O_2]_{out}$, and the same for the fixed carbon concentration $[C]_{in}$ and $[C]_{out}$. Considering the stationarity hypothesis one can say that the differences between the oxygen concentrations $[O_2]_{in}-[O_2]_{out}$ and carbon concentrations $[C]_{in}-[C]_{out}$ are constants, and linked to its stoichiometry. This relationship can be written as follows:

$$\varepsilon \cdot v^*\left([O_2]_{in}-[O_2]_{out}\right)=(1-\varepsilon)\cdot U_f\left([C]_{in}-[C]_{out}\right) \tag{I.12}$$

Where v^* is the interstitial gas velocity, and U_f is combustion front velocity given by:

$$U_f=\frac{\varepsilon}{1-\varepsilon}\frac{[O_2]_{in}-[O_2]_{out}}{[C]_{in}-[C]_{out}}v^* \tag{I.13}$$

Assuming a frame of reference anchored to the reaction front, the energy equation can be written as:

$$\begin{gathered}\varepsilon\rho_g Cp_g+(1-\varepsilon)\cdot\rho_s Cp_s\frac{\partial T}{\partial t}+(\varepsilon\rho_g Cp_g v^*-(\varepsilon\rho_g Cp_g+(1-\varepsilon)\cdot\rho_s Cp_s)U_f)\frac{\partial T}{\partial x}\\ -\lambda^*\frac{\partial^2 T}{\partial x^2}=\delta_{X_F}H_S\end{gathered} \tag{I.14}$$

where, λ^* is the effective conduction coefficient, H_S is a heat source located at the reference (reaction front) and function of δ_{X_F} Dirac's delta.

By linking the heat source with the front velocity gives:

$$H_S=(1-\varepsilon)\cdot\left([C]_{in}-[C]_{out}\right)\cdot U_f\cdot\Delta h_C=\varepsilon\cdot\left([O_2]_{in}-[O_2]_{out}\right)v^*\Delta h_C \tag{I.15}$$

where, Δh_C is the enthalpy reaction for $C+O_2\rightarrow CO_2$.

The adiabatic temperature can be obtained by the relationship between the heat production by the oxidation reaction and global volumetric heat capacity.

$$T_{ad} = \frac{(1-\varepsilon)\cdot\left([\mathrm{C}]_{\mathrm{in}} - [\mathrm{C}]_{\mathrm{out}}\right)\cdot \Delta h_C}{\varepsilon\rho_g Cp_g + (1-\varepsilon)\rho_s Cp_s} \tag{I.16}$$

Noting that is equal $\hat{D} = \dfrac{\lambda^*}{\varepsilon\rho_g Cp_g + (1-\varepsilon)\rho_s Cp_s}$, the eq. (I.14) can be written as:

$$\frac{\partial T}{\partial t} + \left(\frac{\varepsilon\rho_g Cp_g v^*}{\varepsilon\rho_g Cp_g + (1-\varepsilon)\rho_s Cp_s} - U_f\right)\cdot\frac{\partial T}{\partial x} - \hat{D}\cdot\frac{\partial^2 T}{\partial x^2} = \delta_{X_F}\cdot U_f\cdot T_{ad} \tag{I.17}$$

The stationary solution of the eq. is said to be piecewise constant, where the constant is an exponential function as $-\left|\dfrac{x}{\Lambda}\right|$.

where,

$$\Lambda = \frac{\hat{D}}{U_f\left|1-\Delta\right|} \tag{I.18}$$

and

$$\Delta = \frac{\varepsilon\rho_g Cp_g v^*}{\varepsilon\rho_g Cp_g + (1-\varepsilon)\rho_s Cp_s U_f} = \frac{(1-\varepsilon)\rho_g Cp_g}{\varepsilon\rho_g Cp_g + (1-\varepsilon)\rho_s Cp_s}\frac{\left([\mathrm{C}]_{\mathrm{in}} - [\mathrm{C}]_{\mathrm{out}}\right)}{\left([\mathrm{O_2}]_{\mathrm{in}} - [\mathrm{O_2}]_{\mathrm{out}}\right)} \tag{I.19}$$

It is important to note that the value of Δ is not a function of the energy release rate, but only of the heat capacities of the solid and gas and its concentrations.

Three types of travelling combustion front structures were identified in previous work [(Rabinovich et Gurevich 1984), (Aldushin 1990), (Aldushin 1993) and (Schult, *et al.* 1995)]. (Aldushin, Rumanov and Matkowsky 1999) presented a scheme to illustrate the three combustion structures, Figure (I.21).

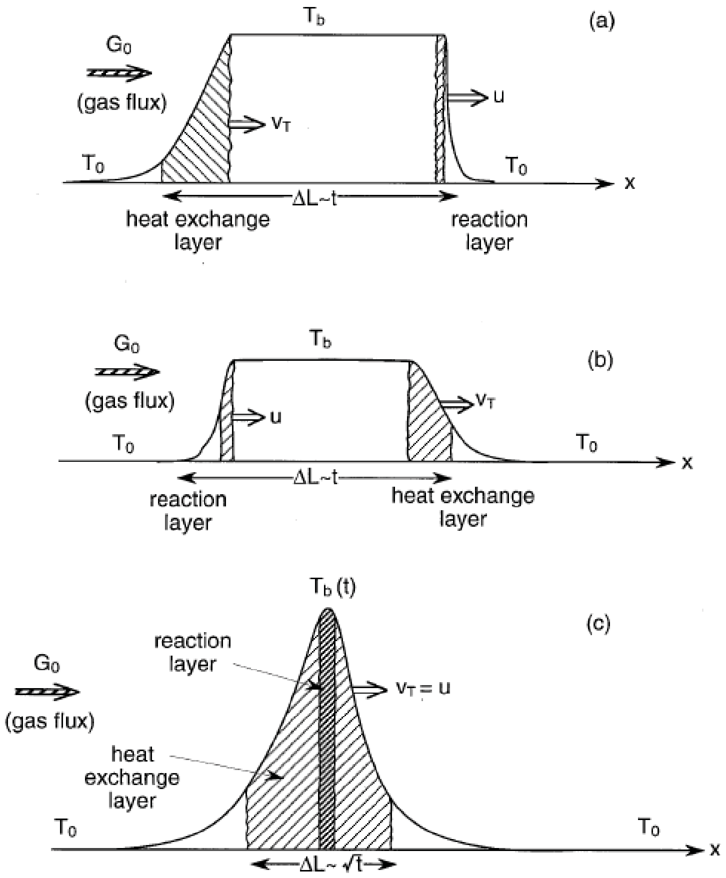

Figure (I.21) - Forward front of combustion: $\Delta < 1$, reaction leading structure; $\Delta > 1$, reaction trailing structure; and $\Delta = 1$, wave with maximal energy accumulation.

The first one, if $\Delta < 1$, where the combustion zone precedes the heat transfer zone, in which the solid gives up heat to the incoming cold fresh gas, to carry it into thermal equilibrium with the solid. Since the processes in two zones are independent, each progress with its own velocity. In this type of structure the reaction zone progress faster and therefore ahead of the heat transfer zone; this type of structure is called *reaction leading structure*. The second called *reaction trailing structure*, if $\Delta > 1$, the heat transfer zone precedes the reaction zone. Experimental observations, of both cases, presented superadiabatic effect. The case $\Delta = 1$ separates the two structures and corresponds to a combustion temperature T_b which is infinite, i.e. solutions in form of travelling combustion front are no longer possible - travelling combustion front analysis breaks down. However, this situation corresponds to conditions where the superadiabatic effect manifests itself most strongly.

I.7 Synthesis

To perform a careful study on literature about the propagation of combustion front in co-current flow, it was necessary investigate the combustion in a counter-current configuration and also some works inrmal analysis. This showed that numerous challenges, as presented in introduction, still need research.

Concerning the experiments

There are:

- In majority of reactors with a little diameter implicated in an important heat losses;
- In all of them solid particles with unstable geometry, such as biomass, MSW, foam, etc ;

Concerning the models

- Choices in formulation of eq. have to be made;
- Determination of macroscopic parameters not trivial;
- Need development;

The literature about the combustion front propagation in a fixed bed of the oil shale is very limited. Thus, the opportunity to develop new devices and numerical model applied to study oil shale combustion are open.

Chapter II

Experimental devices and methods

In this thesis two principal devices were used: a combustion cell and a horizontal tubular reactor. The combustion cell, which was especially developed for this thesis is presented first with its experimental protocol. The horizontal tubular reactor was used to perform accurate thermochemical characterization of the oil shale. Other devices supports were used to complete the characterization in terms:

- Thermogravimetric;
- Elemental;
- Ultimate;
- Of physical analysis;

The gas analyzers used are also described in this chapter. It will also be presented the experimental methods of samples preparation.

II.1 Combustion cell

An experimental device was developed to enable 1D co-current experiments; see Figure (II.1). It consists of a vertical cylindrical combustion chamber of 91 mm internal diameter and a height of 300 mm. The diameter was chosen to be wide enough to limit heat losses through the walls, but narrow enough to avoidthe preparation of large sample quantities, and also to facilitate treatment of flue gas. It is made of a 2 mm-thick stainless steel material, surrounded by two types of insulating material: a 3 mm thick layer of wool (Superwool 607 blanket, Thermal Ceramics, k = 0.28 $Wm^{-1}K^{-1}$ at 982 °C) and a 50 mm thick layer of refractory fiber bloc (Kaowool HS 45 Board, Thermal Ceramics, k = 0.21 $Wm^{-1}K^{-1}$ at 1000 °C).

A grate is located at the bottom of the chamber and consist of a stainless-steel mesh. It is supported by an inner ring, which in turn is supported by the lower cone of the reactor. At the bottom of the cell is placed a copper tube to start cooling the flue gas before contact with the flexible silicone tube connected to reservoirs to condense and collect liquid oil. The air entry is designed to supply uninterrupted airflow in a symmetrical way; see Figure (II.2). Gas analyzers can be momentarily connected at the exit of the condensers to analyze.

The pressure at the top of the reactor and the total mass of the particle bed are continuously recorded.

The reactor is finely instrumented. A group of six in-line thermocouples 0.96 mm in diameter (T1, T2, T3, T10, T11, T12) are located at $Z = 0$, 45 , 90 and 180, 225 and 270 mm (from top to bottom of the reactor), making it possible to measure the temperature along the axis of the cell at different heights. A crown of six thermocouples, identical to the ones previously mentioned, makes it possible to measure the temperature over a horizontal cross section (at approximate middle height, $Z = 135$ mm) 11 mm away from the walls: this will reveal whether the combustion front progresses or not as a horizontal surface.

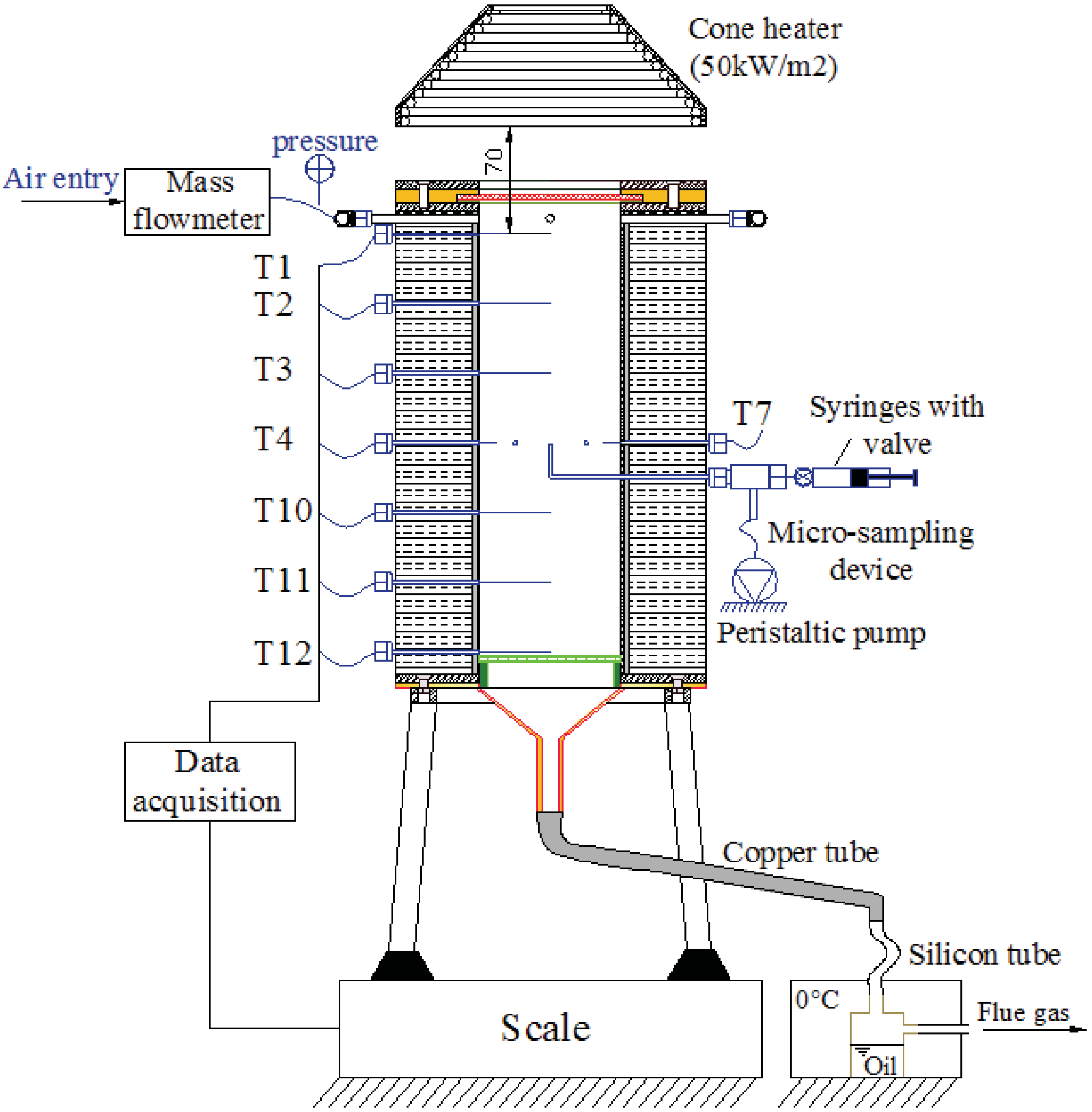

Figure (II.1) - Cell of combustion in porous medium, with micro-sampling system.

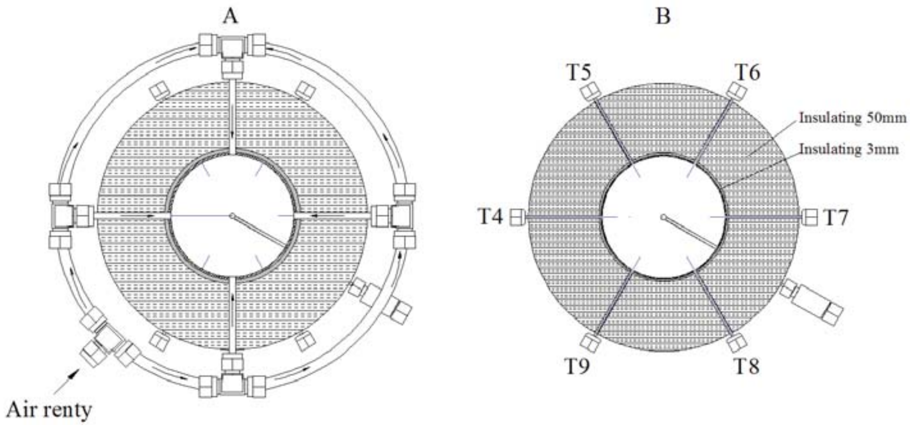

Figure (II.2) - Horizontal cut on the level of the air entry. (B) Horizontal cross-section at middle height of the cell (details: micro sampling system and crown thermocouple).

II.1.1 Ignition of the combustion

To start the combustion with a view to achieving a plane front, a sophisticated ignition device is used, called Cone Calorimeter. On the ignition time, the radiant conical heater temperature is adjusted to 845 °C to impose a heat flux of 45 to 50 kW m^{-2} over the top surface of the oil shale; see Figure (II.3). This radiative flux is generated by a metal surface called a cone heater, heated at high temperature (in our case); it has previously been calibrated using a water-cooled fluxmeter. The radiative flux crosses a quartz porthole that ensures the sealing of the closure, as shown in Figure (II.4). The time of irradiation was 220 s, controlled by opening/closing the insulator shield.

Because of the mechanical and thermal constraints on the top of the cell (steel flange), it was necessary to increase the distance between the cone and the surface of the sample, 25 mm in standard (ISO 5660) to 70 mm, resulting in a non-uniform radiative heat flux at the sample surface illustrated in Figure (II.5).

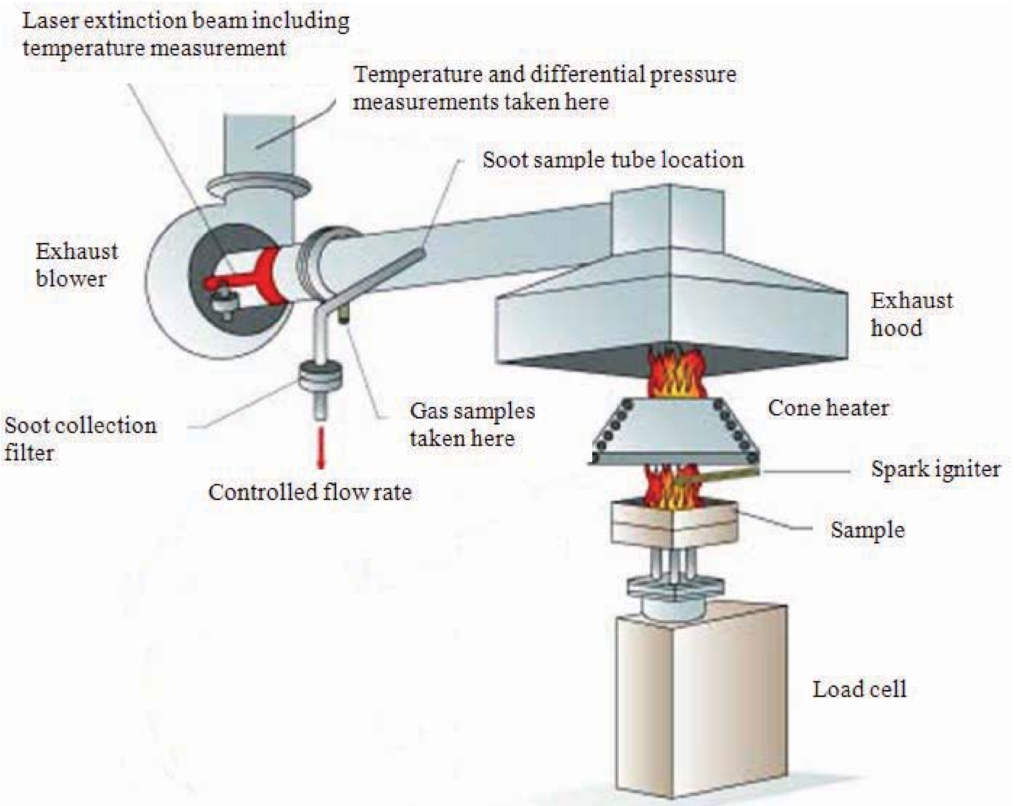

Figure (II.3) - Original schematic diagram of the cone calorimeter.

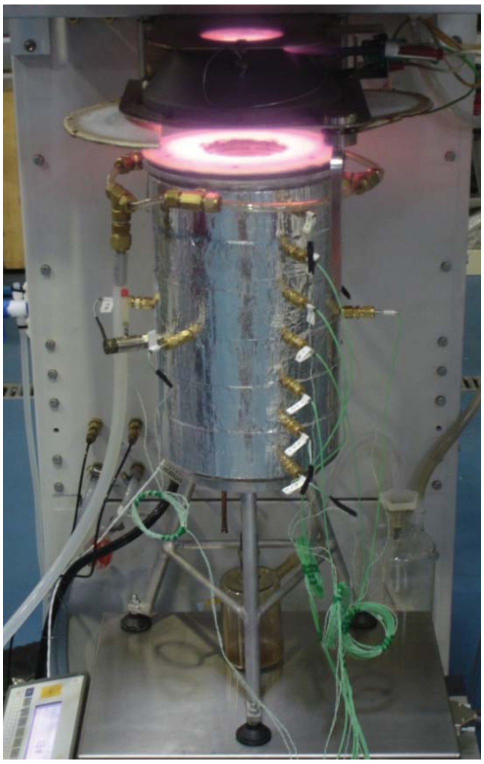

Figure (II.4) - Photograph at the time of irradiation of the oil shale surface.

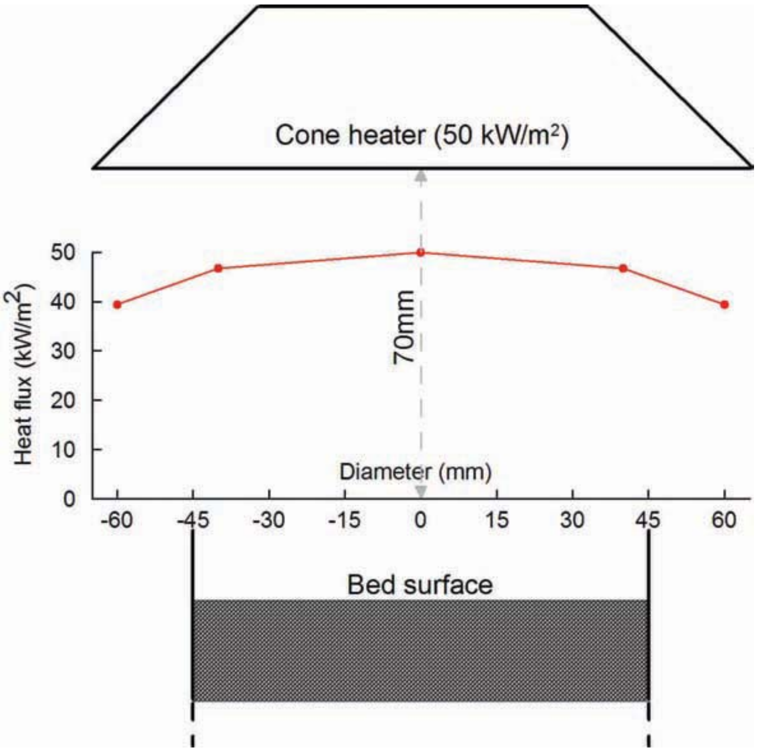

Figure (II.5) - Radiative heat flux profile at the oil shale bed surface.

II.1.2 Micro-sampling system

A new and original device was developed and set up to improve the physicochemical investigation of the structure of the front. This micro-sampling device is shown in Figure (II.1) and Figure (II.2). Its originality lies in its ability to micro sample gas at a fixed point inside the chamber before, during and after the passage of the combustion front.

A peristaltic pump sucks the gas out of the reactor through a 1.6 mm internal tube. The flow rate is fixed at 2.0 ml min^{-1} at 20 °C, corresponding approximately to isokinetic sampling inside the bed, Figure (II.6), in order to minimize the perturbation of the front. The sampled gas is driven to an automatic septum. The dead volume of the sampling tube (1.6 mm internal diameter, 166 mm long) and of the septum was 0.8 ml. Syringes of 0.25 ml (250 µl) with valves are used to sample gas inside the dead volume. A sample is taken every 30 s; during that period, the front progresses by 1.25 mm approximately, which gives an optimistic evaluation of the spatial resolution of the system. The components CO and CO_2 are analyzed a posteriori by gas chromatography, Figure (II.7). Unfortunately, the gas chromatograph setup available did not enable quantifying O_2.

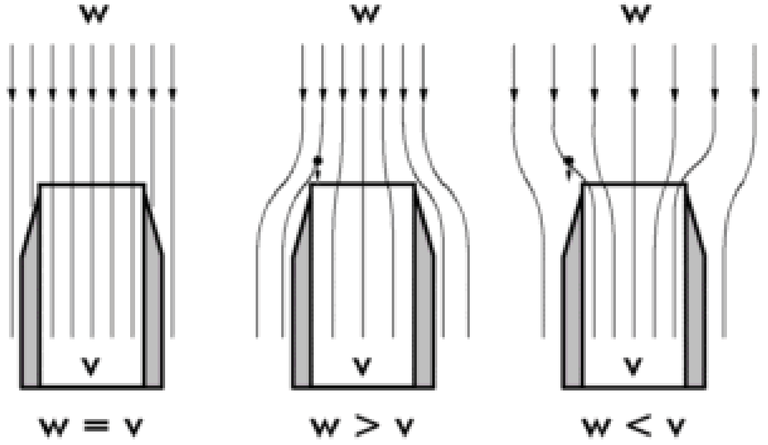

Figure (II.6) - (w = v) Isokinetic case; (w > v) Sampletaking velocity is too low; (w < v) Sampletaking velocity is too high.

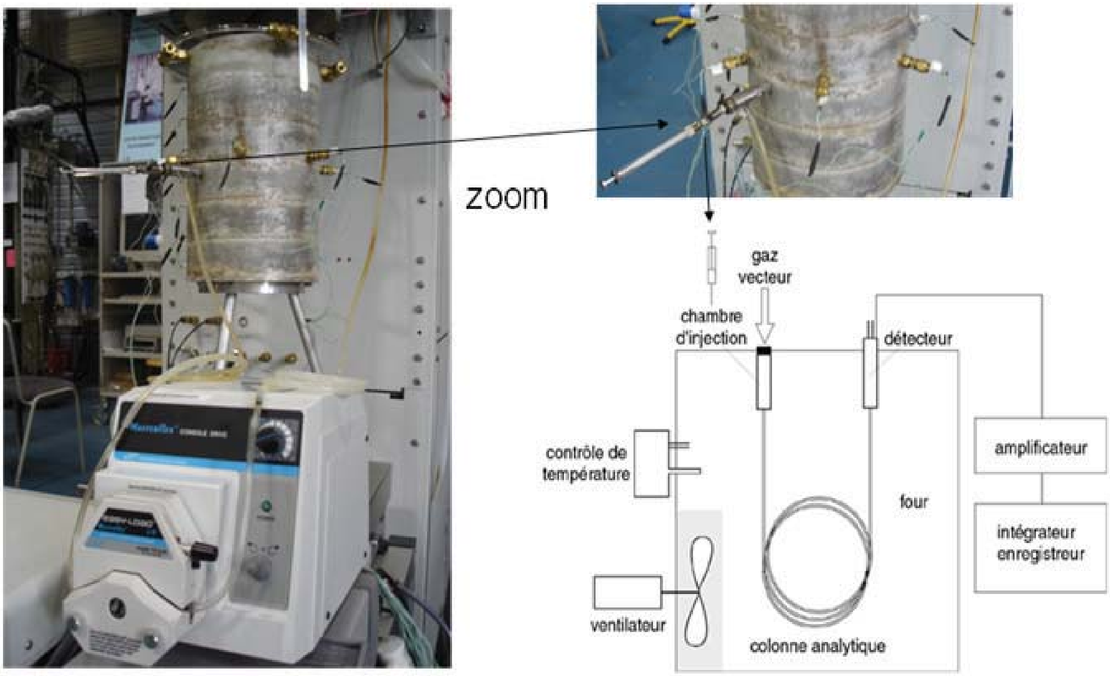

Schematic of a gas chromatography

Figure (II.7) - Micro-sampling apparatus: Peristaltic pump, syringe with valve.

II.1.4 Oil shale samples

The fuel used in the experiments were the Timahdit oil shales deposits, located in the mountains of the Middle Atlas (Morocco), spread over an area of 1000 km^2, [Saoiabi2001]. A consignment of 400 kg of oil shale blocks shown in Figure (II.10-a) was delivered.

The oil shale blocks pass through crushing and then through grinding operations to reduce the size. In the crushing stage the rocks are reduced to about 0.5 to 2 cm, after grinding to obtain particles equal or inferior 2 mm Figure (II.8).

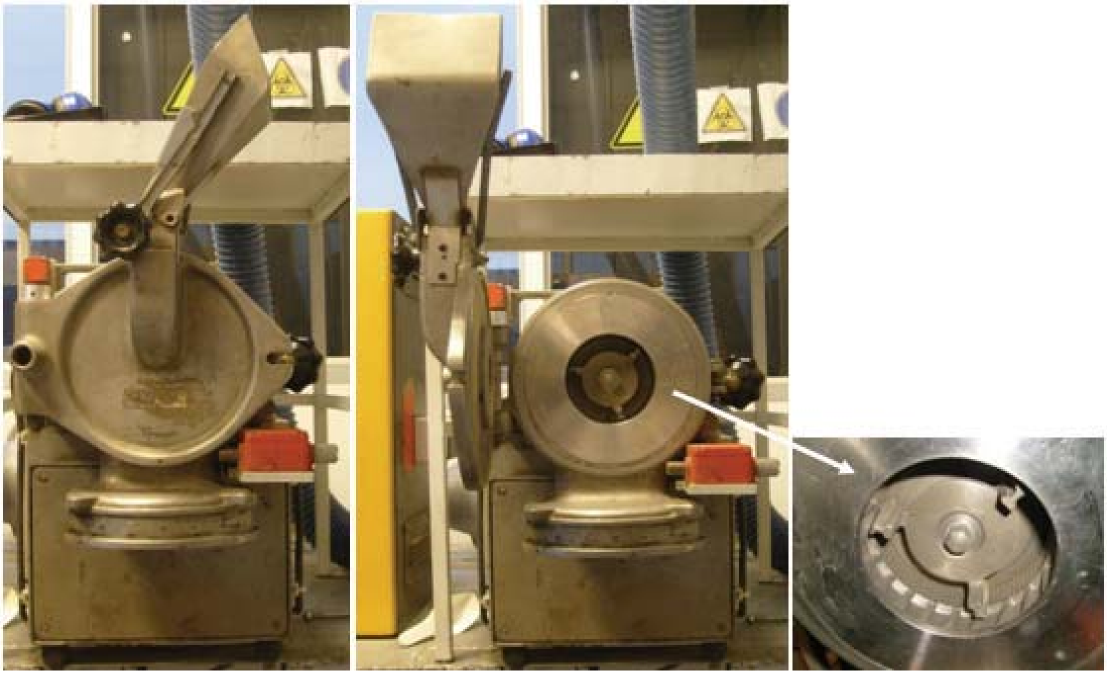

Figure (II.8) - Rock grinding device used to reduce the size particle.

The particles are then sieved into four particles size ranges:

- < 315 µm;
- 315-500 µm;
- 500-1000 µm;
- >1000 µm.

The particle size range distributions are shown in Figure (II.9).

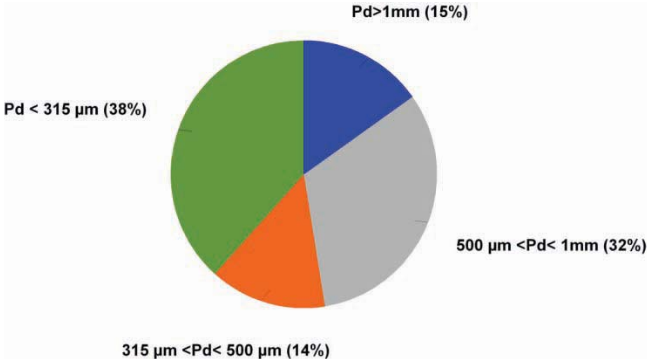

Figure (II.9) - Particle diameters distribution after grinding and sieving.

In order to avoid the deterioration of the reactor wall, the oil shale samples were added with sand are carefully mixed before the experiments, Figure (II.10-c). The sand particle size ranges were also 315- 500 µm, 500-1000 µm and 1- 2 mm.

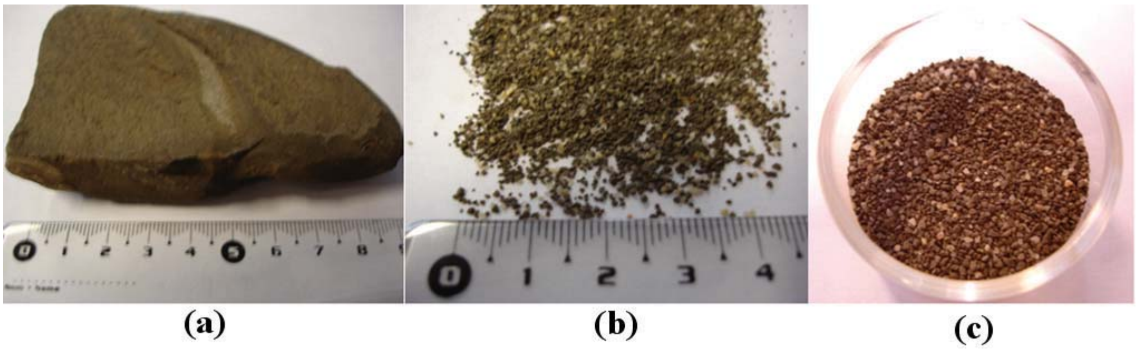

Figure (II.10) - (a) Oil shale block 10 cm, (b) crushed oil shale (500-1000 µm) and (c) mix oil shale/sand, respectively.

II.1.5 Charcoal samples

The combustion cell was validated using a mix of charcoal and sand. The initial material for charcoal preparation consisted of maritime pine wood chips. The charcoal samples were prepared by CIRAD laboratory. The pyrolysis was carried out in an externally heated pyrolysis screw reactor, with a residence time of one hour at 750 °C. The flow rate of char production was 15 kg h^{-1}.

The sample was prepared by pyrolyzing wood chips, grinding the chips, and then selecting the particle size in the range 500-1000 µm. To obtain a homogeneous mix of charcoal particles with sand, it was necessary to prepare a kind of mortar by wetting the mix of charcoal and sand, before intensively mixing the mortar, then placing it into the combustion cell before drying it overnight. It was confirmed that after drying, the charcoal particles - collected from the dry mortar – contained more than 91.6 % of carbon. The mass proportion of carbon was 3.6 %, corresponding to experiments done later with the mix of oil shale and sand. This was obtained by introducing 2256 g of sand and 84.3 g of charcoal (dry base) in the cell.

II.1.6 Procedures before and after an experiment

Procedure of mixing oil shale and sand

After the sieving steps described previously, the range elected (500-1000 µm) is mixed with sand. In the sample mixture the proportion of sand was 25 % and oil shale 75 %. The mixture was agitated until the sample obtains a uniform color, Figure (II.10-c).

Filling the cell

The cell was filled with small quantities of mixture and some strokes were given using a plastic hammer, in order to arrange the particles in the cell (this procedure is repeated until the cell is full and obtains a stable volume of the particle bed).

Centering the cell below the cone heater

Once the cell was filled, the quartz window was placed and fixed to ensure the sealing. After that, the cell was centered in relation to the cone heater center line, Figure (II.5).

Measures before start out

These were the quantities measured:

- Pressure at the top of the bed;
- Mass of the bed.

Measures after the experiment

These were the quantities measured:

- Pressure at the top of the bed;
- Final mass of the bed;
- Bed shrinkage;
- Color of the bed;
- Mass of oil recovered.

II.2 The horizontal tube furnace

The reactor, illustrated in Figure (II.11), consists of a quartz cylinder with 70 mm internal diameter and 1210 mm length, Figure (II.12). The section heated by the furnace has 620 mm length. The sample is put inside a 45 mm diameter mobile spoon (made in steel) and set at the end of a quartz handle of 850 mm length. A thermocouple is located inside the sample. A manometer is placed at the inlet to measure the pressure inside the reactor.

The heating rate of the sample can be controlled inserting more or less rapidly the quartz handle. Figure (II.12) and Figure (II.13) presents the photograph of its respective parts.

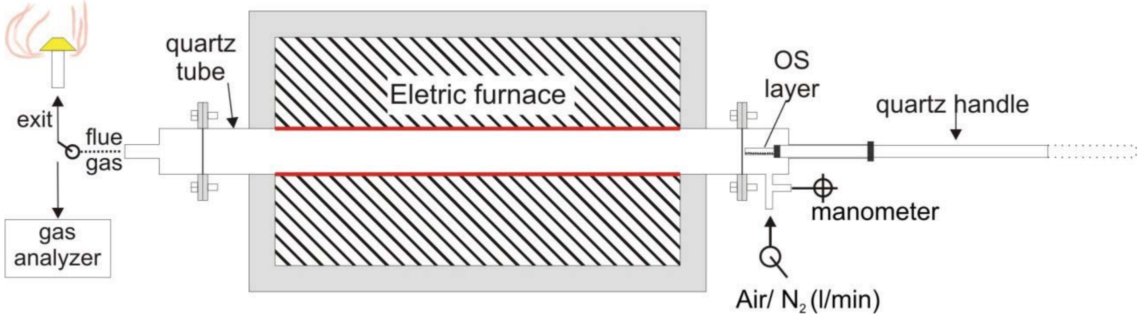

Figure (II.11) - Scheme of horizontal tube furnace.

Figure (II.12) - Horizontal tube furnace.

Figure (II.13) - Spoon inside the quartz tube.

Experimental protocol

Before beginning the experiment, the tests of sealing and atmosphere control were carried out. To ensure that the assembly is sealed and the atmosphere is controlled, nitrogen was first injected inside the reactor at 6 l min^{-1} at STP. The reactor exit was linked to a gas analyzer to ensure that there is no oxygen inside the reactor.

a) Measurement of volatile matter and fixed carbon amounts

At the beginning of the experiment, the furnace temperature was adjusted (550 °C or 900 °C); a layer of oil shale sample (approximately 1 mm) was placed inside the spoon. The spoon was placed in the extremity of the quartz tube (zone not heated) to avoid starting the oil shale degradation.

The atmosphere was chosen according to the type of trial – N_2 for pyrolysis and air for oxidation. After that, the spoon was introduced into quartz tube and the heating rate undergone by the sample was estimated from the temperature measurement, Figure (II.14). The solid residue was then collected and weighed accurately.

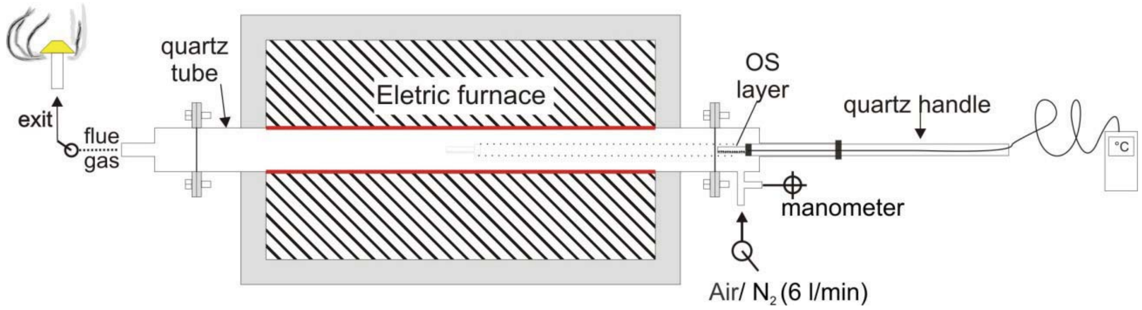

Figure (II.14) - Furnace configuration for pyrolysis and oxidation trials to determine oil shale composition.

b) Analysis of volatile-matter

Initially, the furnace temperature was adjusted at 550 °C; a layer of oil shale sample (approximately 1 mm) was placed inside the spoon. Then the spoon was placed in the extremity of the quartz tube (zone not heated) to avoid starting the oil shale degradation. Under inert atmosphere, N_2 (3 l min^{-1} at STP), the spoon was introduced into quartz tube; the pyrolysis gas was collected in a gas sampling bag. The time during the bag-filling operation was fixed to 5 minutes (a period adequate to complete the pyrolysis process). After that, the gas was analyzed. Figure (II.15) illustrate the furnace configuration used.

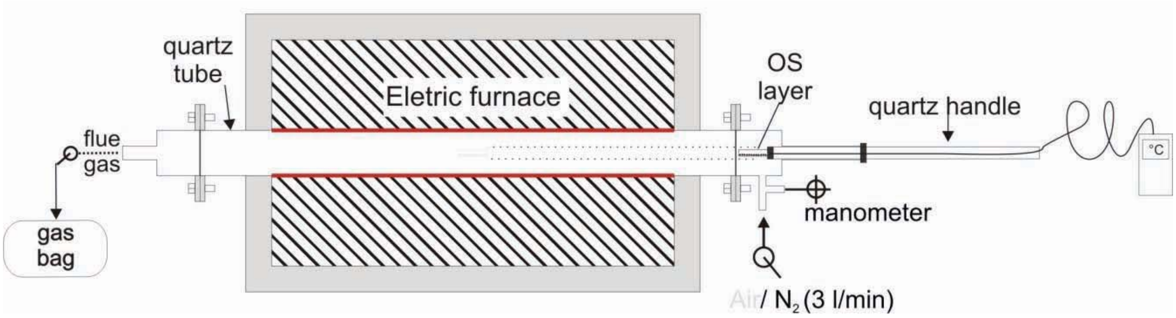

Figure (II.15) - Pyrolysis and filling the sampling bag.

II.3 Laboratory apparatus

II.3.1 The gas analyzers

During the experiments (b) described previously, the gas samples were sent and distributed toward five types of analyzers, Figure (II.16):

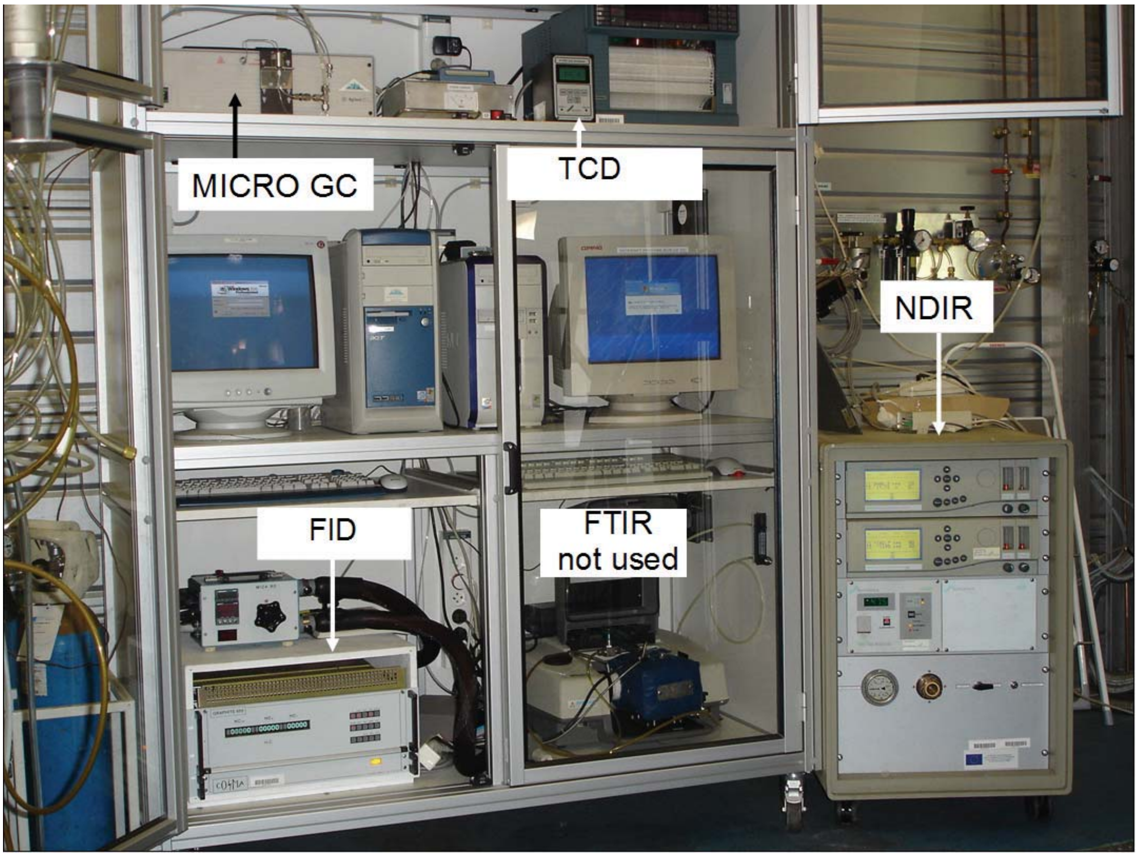

Figure (II.16) - Rack mount gas analyzers.

- a Total hydrocarbon analyzer (two Flame Ionization Detectors - FID, COSMA Graphite 655) quantifying CH_4 and Non-Methane Hydrocarbon (NMHC) ;

- a NDIR technology analyzer (SERVOMEX) capable of measuring CO, CO_2, SO_2, NO and NO_x;

- a Paramagnetic O_2 analyzer (SERVOMEX);

- a Thermal Conductivity Detector (TCD) measuring H_2;

- a Micro GC Agilent 3000 capable of measuring compounds from C_1 to C_{12} and permanent gases (H_2, O_2, N_2, CO, CO_2);

II.3.2 Gas chromatography for analysis of micro-samples

The gases collected from micro-sampling device were analyzed using a GC-6890N equipped with a thermal conductivity detector (TCD) and GS-Carbon PLOT capillary column (30 m × 0.32 mm ID, 3.0 µm, Agilent Tec.). Parameters for analyzing the compounds by GC-TCD are listed in Table (II.1).

GC - 6890

INJECTOR

Mode	Split
Gas	He
Heater (°C)	180
Split ratio	150:1

COLUMNS

Mode	Const. flow
Flow (ml/min) at 35°C	1,8
Average velocity (cm/s)	30

OVEN

°C/min	Next °C	Hold min.	Run time
	35	4	
60	150	1	
			6,92

TCD DETECTOR

Heater (°C)	150
Reference flow (ml/min)	15

Table (II.1) - Parameters for analyzes of micro-samples.

Two species were chosen to be separated:

- CO, which represents one gas formed only by oil shale devolatilization and char oxidation;

- CO_2 that is formed during oil shale devolatilization, by char oxidation and also by decarbonation.

Figure (II.17) shows the calibration curves for both CO and CO_2. Unfortunately, O_2 could not be separated from N2 and analyzed.

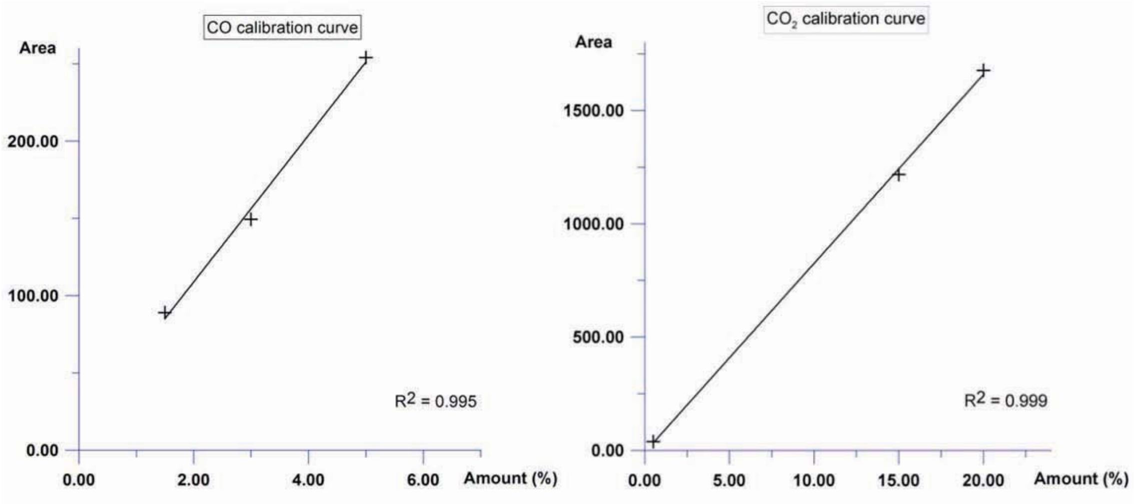

Figure (II.17) - Calibration curves.

Figure (II.18) shows an example of signal for CO and CO_2 with its respective retention times.

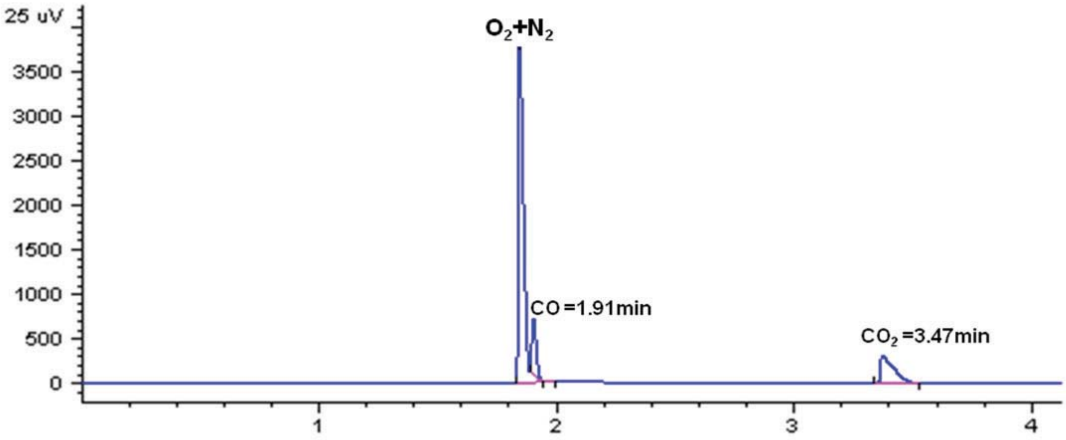

Figure (II.18) - A typical chromatogram of flue gas analysis.

II.3.3 TGA and DSC Instruments

TG and DSC experiments were carried out. The oil shale sample was sieved to obtaining particles between 500-1000 µm diameters. The sample mass were between 30 to 60 mg.

- The thermogravimetric measurements were conducted on a SETARAM TGA 92 instrument. The analyses were performed using both nitrogen and oxygen atmosphere, in the temperature range 25-900 °C, and at the two heating rates of 3 K min^{-1} and 10 K min^{-1}.

- The DSC experiments were carried out using a SETARAM TG-DSC 111 Instruments. Scans were performed from 30 to 800 °C at three different heating rates: 3, 10 and 20 K min^{-1}. The analyses were performed using both nitrogen and oxygen atmosphere.

Table of experiments

Table (II.2) presents the experiments parameters made during this thesis. Each one of the experiments was numerated to facilitate the identification in the text.

	Sand (%)	Air velocity (m/s)	N°	Particle diameter
Charcoal experiments	95	0.024	1	500-1000 µm
			2	
			3	
	96,4	0.024	4	500-1000 µm
			5	
			6	
Oil shale experiments	***25***	***0.024***	7	***500-1000 µm***
			8	
			9	
			10	
			11	
			12	
			13	
		0.042	14	315-500 µm
			15	
			16	500-1000 µm
			17	
			18	1000-2000 µm
			19	
		0.062	20	500-1000 µm
			21	
	50	0.042	22	500-1000 µm
			23	
	65		24	500-1000 µm
			25	

Table (II.2) - presents the experiments parameters made during this thesis. Each one of the experiments was numerated to facilitate the identification in the text.

The charcoal experiments were firstly made to validate the combustion cell. The reference experiment for the oil shale combustion is indicated in bold characters; it was repeated seven times. The other experiments with oil shale were made for the parametric study presented at the end of the document.

Chapter III

Detailed characterization

This chapter is dedicated to perform a detailed characterization of the oil shale: physical, chemical and thermal properties. Then, a fine analysis of the devolatilization gases is made.

III.1 Physical characterization

The oil shale was received as hard dark grey blocks, typically 10 to 20 cm long and 10 to 20 cm wide, and several centimeters thick. The real density is 2257 kg m^{-3} from H_e pycnometer measurement. Mercury intrusion tests indicated a value of 2244 kg m^{-3}, while measuring a cubic block and weighing it gave 2214 kg m^{-3}. The value of 2214 kg m^{-3} was adopted in this work. The blocks do not have a particular smell and do not dirty the fingers when manipulated.

The particle size range 500-1000 µm was obtained after grinding. This range was retained for the analysis and experiments reported here.

From the mass of the oil shale bed in the reactor, the apparent density of a bed was calculated at 1172 kg m^{-3}. The inter-particle porosity of a bed is then 47.0 %.

In order to avoid the deterioration of the reactor wall, a mixture of oil shale and sand 75/25 wt. was used in the experiments. The sand particle size range was also 500-1000 µm; it was checked that the Loss On Ignition (LOI) of the sand heated at 1000 °C was negligible: 0.26 %. The apparent density of the packed bed mixture OS/sand was 1168 kg m^{-3}. The porosity of the bed was consequently 47.2 % (the real density of sand was 2447 kg m^{-3}).

III.2 ThermoGravimetric Analysis (TGA) and Differential Scanning Calorimetry analysis (DSC)

A variety of reactions brought about by the application of heat. For example, (Rajeshwar, Nottenburg, & Dubow, 1979) reported that the presence of a wide variety of minerals in the oil shale matrix significantly complicates thermal behavior. In general, the following reactions can be identified:

(a) evolution of water and gases;

(b) conversion of kerogen to bitumen;

(c) alteration of bitumen;

(d) dissociation of bitumen from oils, gases and other compounds;

(e) vaporization of oils;

(f) burn-off of fixed carbon;

(g) decomposition of organic residues and inorganic minerals.

The TGA experiments were carried out using samples of approximately 30 mg, with a heating rate of 3 K min^{-1} up to 900 °C. The decomposition of the oil shale sample under both, inert atmosphere and air, are presented in Figure (III.1).

Under atmosphere (N_2) several stages can be observed:

a) Water evaporation, occurring at temperatures between 50 and 150 °C;

b) Kerogen decomposition into volatile matter - including condensable oil - and into solid fixed carbon in the temperature range 150 - 550 °C;

c) Thermal decomposition of carbonates, which can be assumed to be essentially limestone ($CaCO_3$), into quick-lime (CaO) and carbon dioxide (CO_2), in the temperature range 550- 770 °C.

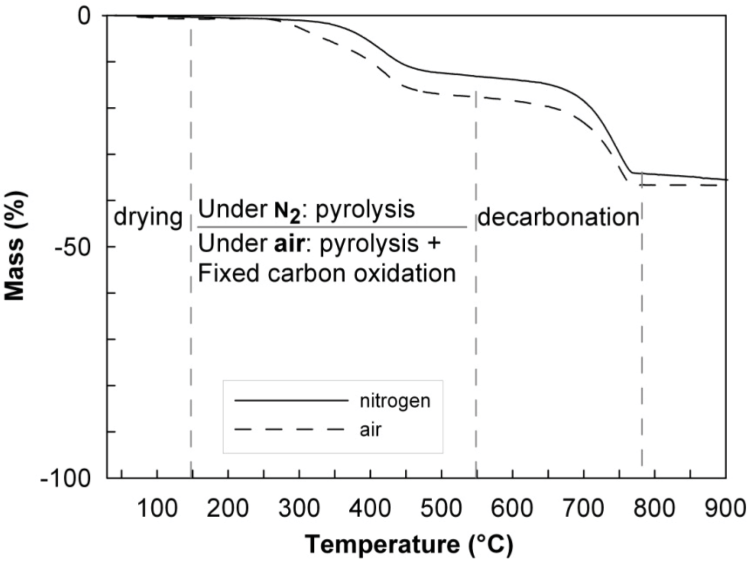

Figure (III.1) - TGA of oil shale under air and under nitrogen - heating at 3Kmin^{-1}.

During TGA under air, the same sequence is observed, but the mass loss between 150- 550 °C additionally includes the oxidation of fixed carbon. There is no clear separation between the two stages of pyrolysis and decarbonation along the test. For this reason, it was not possible to determine with any accuracy the amount of organic matter: in the same way as mass difference between the dry oil shale and oil shale after oxidation. The difference between the two mass curves after pyrolysis (around T= 550 °C) gives the amount of 4.8 % for fixed carbon. It is worth noting that the difference between the two curves decreases along the decarbonation process. This means that for the experiments under N_2, the amount of fixed carbon decreases during decarbonation, and even after completion of decarbonation. It is difficult to give a physical explanation to this observation. The total mass loss of the oil shale sample heated to 900 °C under air is 36.7 %.

Figure (III.2) shows the first derivative curve as a function of temperature, giving the Differential Thermogravimetry (DTG) of oil shale under air at the heating rate of 3 K min^{-1}.

There exist two peaks at 310 °C and 420 °C corresponding to the devolatilization of oil shale and the oxidation of fixed carbon respectively, and one peak around 770 °C corresponding to decarbonation. When the heating rate is increased to 10 K min^{-1}, a peak appears at 60 °C. This phenomenon was also clearly observed during all experiments in the combustion cell (cf. IV.2.2.A), where can be seen a plateau in temperature at precisely 60 °C for all thermocouples. It was attributed to an endothermic phase change that was not identified, but probably not drying of the oil shale.

The results from DSC tests are reported in Figure (III.3). The experiment under air shows two exothermic reactions, which occurs in the interval of 250- 550 °C. The first peak at 291 °C is due to the oxidation of part only of the volatile matter (Kok and Pamir, 1998) and the second at 411 °C is the oxidation of the carbonaceous residue (fixed carbon). Indeed, these two peaks do not appear when the DSC is performed under N_2. The origin of the second peak was confirmed by performing a similar analysis with a sample of oil shale previously pyrolyzed under inert atmosphere: only the second peak appears. For the two exothermic reactions which occur in an interval of 250 – 550 °C – that cannot be clearly separated - the reaction heat is + 3700 kJ kg^{-1} oil shale.

Around 770 °C, under both air and nitrogen atmosphere the endothermic peak of decarbonation appears. The measured endothermic reaction heat was – 589 kJ kg^{-1} oil shale.

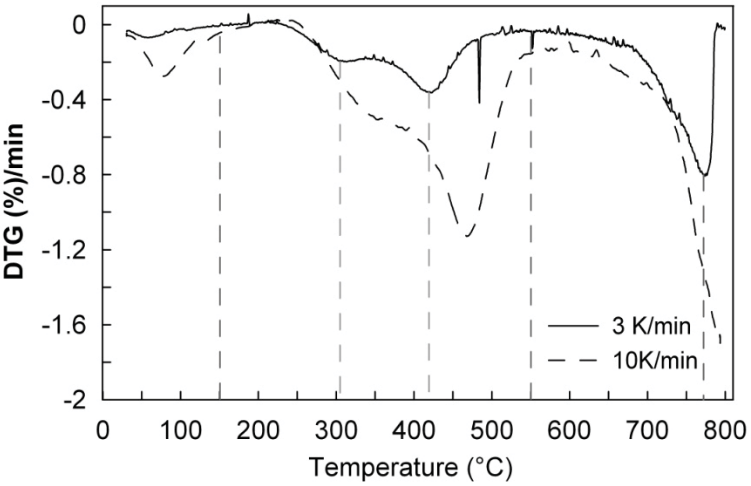

Figure (III.2) - DTG curves of oil shale under air - heating at 3 and 10K min^{-1}.

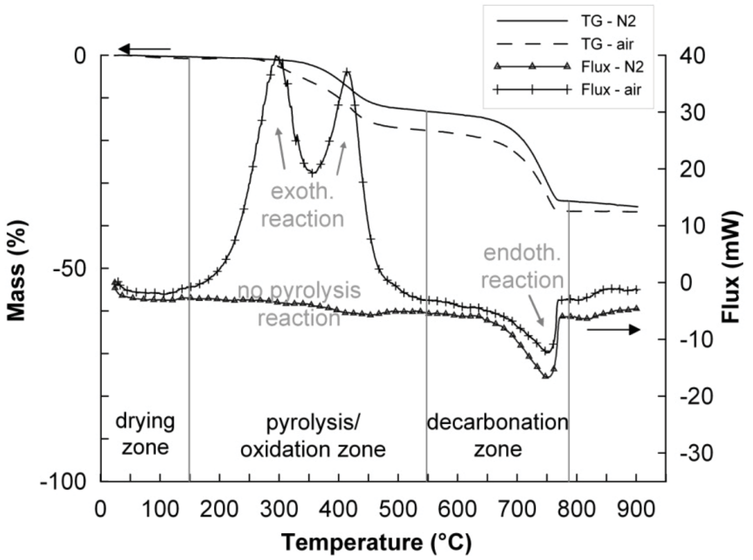

Figure (III.3) - TGA/ DSC of oil shale under air and under nitrogen – heating at 3 K min^{-1}.

III.3 Determination of the Arrhenius parameters

Arrhenius parameters for char oxidation reaction

Char oxidation has been studied extensively, the mechanisms by which these oxidation reactions occur remain poorly understood. For the purposes of this thesis, it was adopted the notation of [(Schult, *et al.* 1995), (Akkutlu and Yortsos 2003) and (Lapene, et al. 2007)] considering simple one-step reaction model on the form:

$$C + [\frac{fr}{2} + (1 - fr)]O_2 \rightarrow fr\ CO + (1 - fr)CO_2 \qquad \text{r.4}$$

where the term fr is the [CO2]/[CO] oxidation reaction molar ratio.

To determine the Arrhenius parameters for fixed carbon oxidation it was used the results from DSC experiment of oil shale.

The DSC or quantitative differential thermal analysis is the most commonly used technique for analyzing kinetic parameter. In this experiment, not only the heat of reaction but also the reaction kinetics can be evaluated. The Kissinger method [(Kissinger 1957), (Kök and Pamir 2000) and (Kowhakul, et al. 2006)] with a variable heating rate, which depend on the peak maximum in the DSC were employed. The activation energy (E) can be calculated from the results.

Kissinger suggests a method, which relates the logarithm of (β/T_P^2) with the inverse of the peak temperature, Figure (III.4), through the following expression:

$$-\ln\left(\frac{\beta}{T_P^2}\right)=\frac{E}{RT_P^2}-\ln\left(\frac{k_0R}{E}\right) \tag{III.1}$$

simplifying eq. (III.1) gives:

$$\ln\left(\frac{T_p^2}{\beta}\right)=\frac{E}{RT_p^2}+C_1 \tag{III.2}$$

Where β is heating rate, E is the activation energy, C_1 is a constant linear coefficient and R is the gas constant (8.314 $\mathrm{Jmol^{-1}K^{-1}}$).

Thus, activation energy and pre-exponential factor were calculated using the following equations:

$$E_a=R\frac{d\ln(\beta/T_p^2)}{d(1/T_p)} \tag{III.3}$$

$$A_p=\frac{\beta E_a}{RT_p}e^{(E_a/RT_p)} \tag{III.4}$$

Using this method the determined activation energy and pre-exponential factor were E= 52.4 kJ $\mathrm{mol^{-1}}$ and A= $0.0546\mathrm{x}10^4$ $\mathrm{min^{-1}}$.

Finally the kinetics model determined was:

$$\frac{d\alpha}{dt}=0.0546\times10^4\exp^{-\frac{52400}{RT}} \tag{III.5}$$

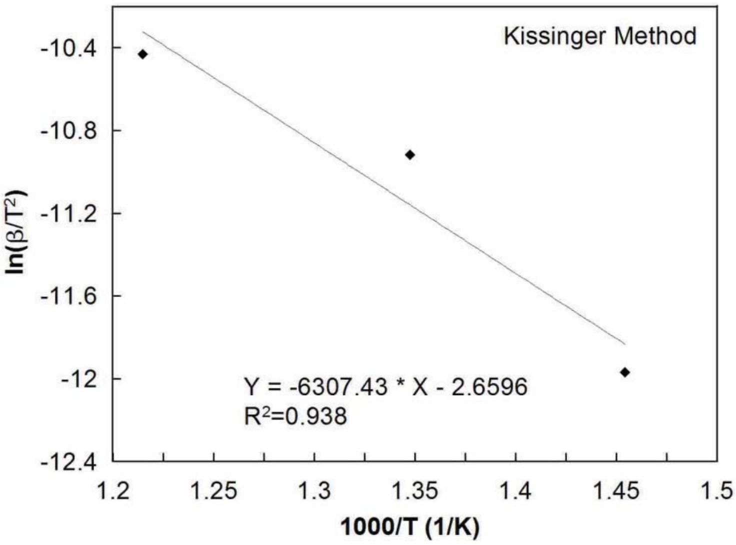

Figure (III.4) - Kissinger plot for oil shale samples at 3, 10 and 20 Kmin^{-1}.

(Kok 2001) in his work about oil shale combustion on DSC experiments, reported that on DSC combustion curves of oil shale samples, two reaction regions were observed – the same for the present work – the "shoulder" on the high temperature side of the reaction region was attributed to the possible swelling of the sample, resulting in an impermeable mass that reduced the oxygen accessibility, causing a decrease in the reaction rate.

Arrhenius parameters for calcite decarbonation reaction

A differential method for sample at a single heating rate was employed. This method has been employed to calculate Arrhenius parameters of decarbonation reaction from TG/DTG experiments [(Dollimore, Tong et Alexander 1996), (Samtani, Dollimore and Alexander 2002) and (Yang, et al. 2000)].

To obtain the kinetic parameters, a combination of equations is used which include the following:

$$\frac{d\alpha}{dt} = k \cdot f(\alpha) \tag{III.6}$$

$$\ln k = \ln A - \frac{E}{RT} \tag{III.7}$$

where, α is the fraction reacted, *da/dt* the rate of the reaction and *f(a)* the mathematical expression in α , table "*f(a)*".

Combining eqs. (III.6) and (III.7) gives:

$$\ln\left[\frac{d\alpha/dt}{(1-\alpha)^n}\right] = \ln A - \frac{E}{RT} \tag{III.8}$$

The differential form of α gives:

$$\frac{d\alpha}{dt} = \frac{dw_t/dt}{w_i - w_f} \tag{III.9}$$

The function dw_t/dt can be obtained directly from the (DTG) plot, and the rate of the reaction can be calculated using Eq. (III.9). This value of *da/dt* obtained from Eq. (III.9) is substituted into Eq. (III.8) and finally a plot of ln[(*da/dt*)/*f(a)*] versus 1/T is constructed.

Type	$f(\alpha)$
Order equation	
Zero order	1
First order (F1)	$1-\alpha$
Second order (F2)	$(1-\alpha)^2$
Geometric	
Contracting area (R2)	$2(1-\alpha)^{1/2}$
Contracting volume (R3)	$3(1-\alpha)^{2/3}$
Sigmoid curve	
Avrami–Erofeev (A1.5)	$1.5(1-\alpha)(-\ln(1-\alpha))^{1/3}$
Avrami–Erofeev (A2)	$2(1-\alpha)(-\ln(1-\alpha))^{1/2}$
Avrami–Erofeev (A3)	$3(1-\alpha)(-\ln(1-\alpha))^{2/3}$
Avrami–Erofeev (A4)	$4(1-\alpha)(-\ln(1-\alpha))^{3/4}$
Prout–Tompkins (B1)	$\alpha(1-\alpha)$
Diffusion	
1D diffusion (D1)	$1/2\alpha$
2D diffusion (D2)	$-(\ln(1-\alpha))^{-1}$
3D diffusion (D3)	$1.5(1-(1-\alpha)^{1/3})^{-1}(1-\alpha)^{2/3}$
Ginstling–Brounshtein (D4)	$1.5(1-(1-\alpha)^{1/3})^{-1}$
Power law, $m > 1$ (P1)	$m(\alpha)^{(m-1)/m}$

Table (III.1) - The mathematical models for the reaction mechanisms.

From the eq. (III.8) and plotting ln[(*da/dt*)/*f(a)*] *vs.* 1/T, one can obtain the activation energy *E* and the pre-exponential factor *A* from the slope and the intercept of the regression line respectively. The linear regression plot for this sample is illustrated in Figure (III.5).

It was found by [(Samtani, Dollimore and Alexander 2002)] that calcite supposedly decompose via a zero order mechanism, indicating f(α)= 1, see Table (III.1). The activation energy and pre-exponential factor were E= 135.1 kJ mol^{-1} and A= 2.68x10^{4} min^{-1} which is in good agreement with the results obtained by [(Maciejewski 2000) and (Samtani, Dollimore and Alexander 2002)] reported E= 180 kJ mol^{-1} and 175.05 kJ mol^{-1} respectively.

Finally the kinetics model determined was:

$$\frac{d\alpha}{dt} = 2.68\times10^{4}\exp^{-\frac{135100}{RT}} \quad \text{(III.10)}$$

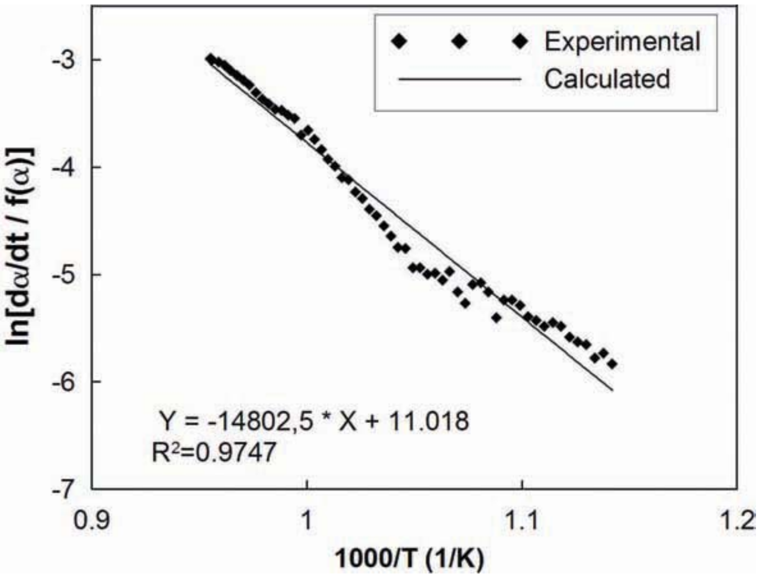

Figure (III.5) - The Arrhenius plot for calcite decomposition at 3 K min^{-1}, (sample 31.66 mg) using an *f(a)*-value of 1 which corresponds to a zero order mechanism.

III.4 Chemical characterization

The oil shale was analyzed by standard elemental analysis (CHONS) using a DIONEX ICS 3000 analyzer. Table (III.2) shows the compound amounts. It may be noticed that the quantified oxygen amount corresponds with the organic matter only, because the analyzer does not detect the oxygen contained by mineral matters that is released as CO_2 due to the decarbonation of carbonates.

	C	H	N	S	O
Oil shale (wt.%)	15,9	1,5	0,24	1,5	10,5
Oil shale residue (wt.%)	1,8	0,1	0	0,68	1,1

Table (III.2) - CHNSO analysis of oil shale

The standard proximate analysis of oil shale is shown in Table (III.3). The devolatilization of oil shale yields 2.5 % moisture and 26.9 % volatile matter, while 6.9 % of fixed carbon is produced.

Oil shale			
Ash (wt%)	**Volatile (wt%)**	**Fixed carbon (wt%)**	**Moisture**
63,7	26,9	6,9	2,5

Table (III.3) - Standard proximate analysis of oil shale.

It is clear that the results of proximate analysis depend on the conditions used in the procedure. In particular, the heating rate may affect the results. Since the values obtained from this analysis will be instrumental in establishing a mass balance of the combustion process, detailed proximate analyses were carried out using the horizontal tube furnace (cf. II.2.a). This apparatus enables the heating rate to be controlled and guarantees an efficient removal of volatile matter from around the particles. When repeating the trials, the repeatability for a mass loss determination was indeed very good: better than 0.4 %.

In this section, the oil shale is seen as a mix of inert materials, carbonates, organic matter and water, as illustrated in Table (III.4).

From the observation of the thermogravimetric curves, it was decided to operate tests at two temperatures:

(i) at 550 °C, in order to obtain:

- first, the thermal decomposition (or devolatilization) of the oil shale by operating under N_2;
- secondly, the oxidation of the fixed carbon, shifting the atmosphere to air.

At this temperature the decarbonation of the carbonates is not achieved.

(ii) at 900 °C, in order to obtain the same reactions as in the case of 550 °C testing, but with the occurrence of decarbonation during the thermal decomposition under N_2.

- The oil shale decomposition at 550 °C under inert and oxidizing atmospheres makes it possible to determine the amounts of volatile matter and fixed carbon respectively. As illustrated in Table 3a, the amount of volatile matter plus water was a+a' = 17.2 %, from which the volatile matter amount is calculated at 14.7 % since the amount of water was 2.5 %. The amount of fixed carbon was b-a-a'= 4.7 %. This value is very similar to that determined using TGA (4.8 %). The value obtained during proximate analysis is higher, at 6.9 %. This can be attributed to the fact that during the test, the volatile matter was maintained in contact with the sample inside the test crucible, causing the repolymerization of some volatile matter into solid pyrolytic carbon; this value will not be retained.

- At 900 °C, along with the thermal degradation of organic matter, the decarbonation process occurs. The difference d–c-c' gives the amount of fixed carbon, determined at 1.2 %. It is worth noting that this value is different from that found at 550 °C. This result remains difficult to explain, but confirms the observation made during TG experiments: heating the pyrolyzed oil shale to high temperature (900 °C) under inert atmosphere leads to a progressive decrease in the amount of fixed carbon.

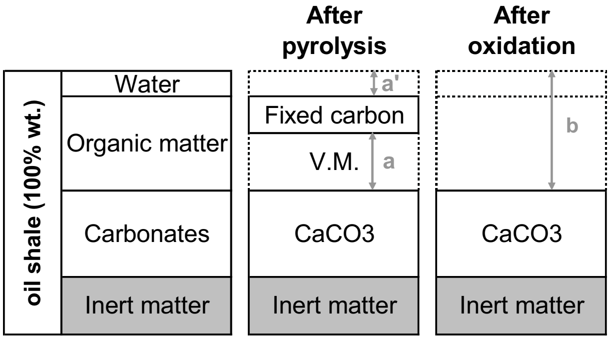

(a) At 550°C - without decarbonation

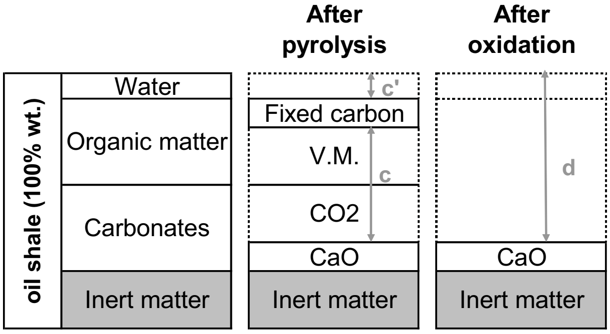

(b) At 900°C - with decarbonation

Table (III.4) - Detailed proximate analyses. (-) solids; (....) gas.

Subtracting d – b it is possible to determine the amount of CO_2 produced by decarbonation: about 15.9 %. Carbonates can be assumed to be essentially limestone. Considering the decomposition of limestone ($CaCO_3$) into quick-lime (CaO) and carbon dioxide (CO_2) according to the reaction (1), one can determine the amount of $CaCO_3$ at 34.6 %.

$$CaCO_{3(s)} \rightarrow 0.56CaO_{(s)} + 0.44CO_{2(g)} \qquad \text{r.5}$$

This value is similar to the thermogravimetry analysis result, which gave 36.7 %.

According to (Williams and Ahmad 1999), the heating rate has an influence on the product yield in the range between 5 to 40 K min^{-1}. As will be shown later, the oil shale undergoes heating rates in the range 70 to 90 K min^{-1} along combustion inside the combustion cell. Therefore, using the horizontal tube furnace, the effect of heating rate on the mass loss was investigated. The tests presented above were carried out at a heating rate of 170 K min^{-1}. Two additional tests were carried out at heating rates of 50 and 900 K min^{-1} under N_2. Again, two final temperatures were used: 550 and 900 °C. Table (III.5) summarizes the results obtained in the range 50 to 900 K min^{-1}: the heating rate does not affect the mass loss due to pyrolysis (results at 550 °C) and to pyrolysis plus decarbonation (results at 900 °C). Consequently, the amount of fixed carbon was not affected by the heating rate.

	Heating rate (K/min)		
Furnace temperature (°C)	**50**	**170**	**900**
550	16,5%	17,2%	-
900	36,7%	37,1%	35,9%

Table (III.5) - Mass loss of oil shale after heating at 550 °C and 900 °C under N_2, in the horizontal tube furnace following three heating rates.

Table (III.6) presents a summary of the main results achieved in this work with some comparison with the literature for Timahdit oil shale. The results are similar to those of other authors regarding the composition of oil shale. The values adopted here were: kerogen 21.9 %, $CaCO_3$ 34.6 % and Inert matter 43.5 %.

Composition (wt.%)	**"spoon furnace" (170K/min)**	**TGA (3K/min)**	**(Saoiabi *et al.* 2001a)**	**Sadiki *et al.* (2003)**
Kerogen	21,9	18,0	24,4	24,3
Carbonates ($CaCO_3$)	34,6	42,3	40,1	35,5
Inert matter	43,5	39,7	35,5	40,5

Table (III.6) - Summary of composition results of oil shale.

Analysis of the devolatilization gases

In specific experiments using the horizontal tube furnace (cf. II.2.b), the composition of the permanent gases (non-condensable fraction of volatile matter) was established. The species CO, CO_2 and H_2 were analyzed using a gas chromatographer. A two FID detectors analyzer were used to quantify methane and total non-methanic hydrocarbons (NMHC, in equivalent CH_4), while SO_2 was quantified using a NDIR analyzer. The results were expressed first in g/g oil shale, then in g/g of organic matter, as shown in Figure (III.6). Concerning NMHC, a molar mass of 16 g mol^{-1} was assumed for this species (expressed in equivalent mole of carbon). In figure, the mass fractions of fixed carbon in oil shale and in the organic matter - as determined previously - were added. A fraction of oil was also added infigure to recover a total of 100 % organic matter; this amount is 53 % of the organic matter.

A quarter of organic matter is found as fixed carbon; only one quarter of the organic matter is converted into gases, and approximately half of the organic matter is found as oil, including some water. NMHC represents approximately 10 % of the organic matter initial mass. CO_2 and SO_2 each represent approximately 5 %. The species CO represents only 1 % of initial organic matter mass, and H_2 is present in negligible quantities. These results will be used further to establish a mass balance of the front propagation process.

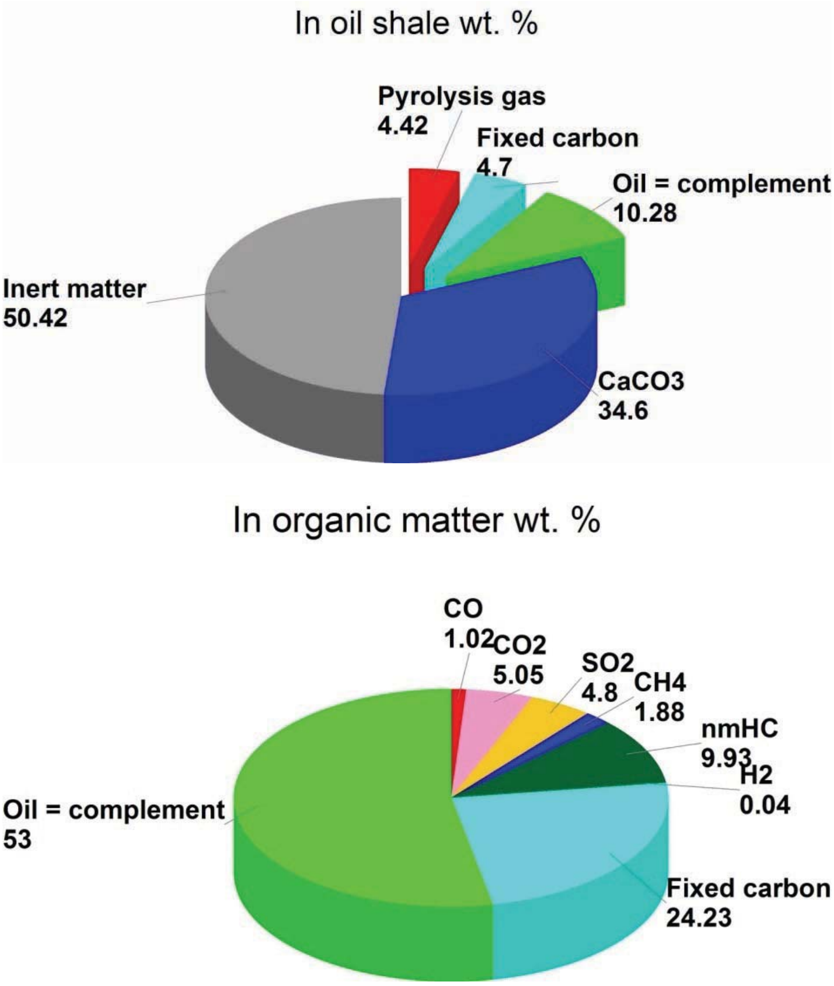

Figure (III.6) - Pyrolysis gas.

III.5 Heat transfer properties

Three heat transfer properties were determined: thermal conductivity, heat capacity and heat transfer coefficient between gas and solid.

III.5.1 Thermal conductivity and heat capacity

These properties were determined for oil shale and sand using the hot disk method, which can be used to analyze material with a thermal conductivity between 0.005 and 500 $Wm^{-1}K^{-1}$ and covering a temperature range of -255 °C to 700 °C. These were the samples:

- oil shale blocks 25 mm x 40 mm x 50 mm: the blocks were machined to obtain a regular shape, Figure (III.7).

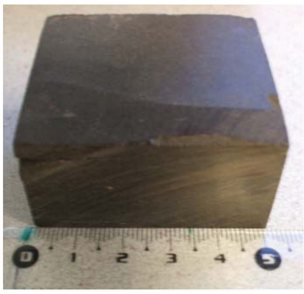

Figure (III.7) - Machined oil shale piece.

- The crushed oil shale was sieved to obtain the following particles diameters: 315-500 µm, 500-1000 µm and 1000- 2000 µm;
- sand with particles diameters between 500-1000 µm.

During the measurement, the hot disk sensor was sandwiched between two pieces parts for the crushed oil shale and sand, Figure (III.8), and between two oil shale blocks.

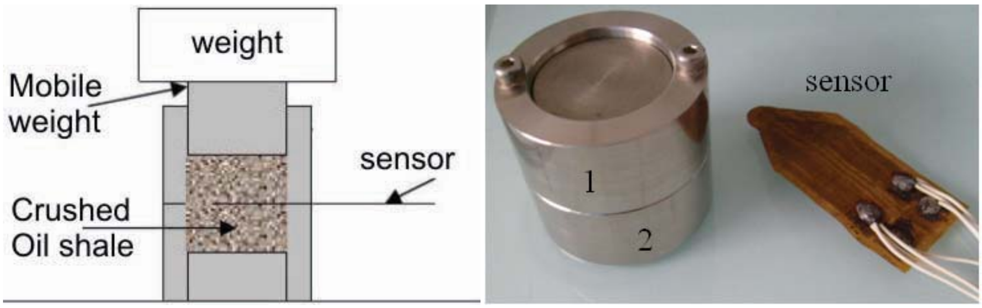

Figure (III.8) - Hot disk apparatus.

Table (III.7) presents the results. At a given temperature, crushed oil shale conductivity increases with increasing particle size. The sand conductivity at 200 °C is about 1.6 times the oil shale conductivity (500-1000 µm). The oil shale blocks present the opposite behavior: the thermal conductivity decreases when increasing the temperature.

	Crushed oil shale					**Sand**
	315-500µm		**500-1000µm**	**1000-2000µm**		**500-1000µm**
T (°C)	λ (W/m K)	ρ Cp (MJ/m^3 K)	λ (W/m K)	λ (W/m K)	ρ Cp (MJ/m^3 K)	λ (W/m K)
20	0.185	1.0	0.194	0.232	1.2	0.270
80	-	-	0.216	-	-	0.321
100	0.205	1.2	-	0.252	1.3	-
140	-	-	0.226	-	-	0.373
200	0.208	1.3	0.24	0.275	1.4	0.395

	Oil shale block
T (°C)	λ (W/m K)
20	0.898
80	0.899
100	-
140	0.857
200	0.831

error for λ: ± 5.0%
error for ρ Cp: ± 5.0%

Table (III.7) - Heat transfer properties for crushed oil shale, sand and oil shale block.

III.5.2 Heat transfer coefficient ($\Gamma_{s,g}$)

Solving the heat balance eq. (III.11) and (III.12) for the gas and solid, requires the description of the heat exchange between the two phases: $\Gamma_{s,g}$.

- Gas phase energy balance

$$\epsilon_g \left(\rho C_p\right)_g \frac{\partial T_g}{\partial t} + \left(\rho C_p\right)_g v_g \frac{\partial T_g}{\partial x} = \frac{\partial}{\partial x}\left(\lambda_g^* \frac{\partial T_g}{\partial x}\right) + \Gamma_{s,g}\left(T_g - T_s\right) + Q_g \tag{III.11}$$

- Solid phase energy balance

$$\epsilon_s \left(\rho C_p\right)_s \frac{\partial T_s}{\partial t} = \frac{\partial}{\partial x}\left(\lambda_s^* \frac{\partial T_s}{\partial x}\right) + \Gamma_{g,s}\left(T_s - T_g\right) + Q_s \tag{III.12}$$

where the subscript *s* and *g* are respectively solid phase and gas phase.

In the literature, $\Gamma_{s,g}$ can be calculated using:

$$\Gamma_{s,g} = \frac{\lambda_g}{d_p} \cdot \left(2 + 1.1 \cdot \mathrm{Re}^{0,6}\, \mathrm{Pr}^{1/3}\right) \tag{III.13}$$

where λ_g is the gas conductivity, d_p average particle size, *Re* is the Reynold number and *Pr* is the Prandtl number.

Nevertheless, it is known that such a calculation can lead to large errors. $\Gamma_{s,g}$ was evaluated from specific experiment and fitting a numerical model to the results. The medium was heated to 45 °C overnight. An air flow of 16.5 l min^{-1} at STP ambient temperature was then forced through the medium, while the bet temperature was measured.

The mathematical model is based in the eq. (III.11) and (III.12). The following assumptions were used:

1) The inlet fluid temperature is uniform. The particles and fluid temperatures in the porous medium vary only along the flow direction and with time, so the system can be analyzed with a one-dimensional transient analysis;

2) The porous medium is isotropic and has a uniform porosity;

3) The fluid flow is incompressible and its thermophysical properties vary with temperature;

4) the air in the porous channel is a continuum.

Noting that the heat transfer coefficient can be expressed using:

$$\Gamma_{s,g} = A_{factor} \cdot \frac{\lambda_g}{d_p} \cdot \left(2 + 1.1 \cdot \mathrm{Re}^{0,6}\, \mathrm{Pr}^{1/3} \right) \qquad \text{(III.14)}$$

A_{factor} is the adjust factor used to fit the model.

The equations were solved using a numerical modeling developed and presented in detailed in chapter V.

Figure (III.9) shows the temperature evolution in the bed for the thermocouple placed at Z = 170 mm in the reactor. Using the value A_{factor}= 55 a good agreement between the experimentally measured temperature and the computed temperature is obtained. It is interesting to note that the rate between $\Gamma_{s,g}$ from literature and $\Gamma_{s,g}$ determined from experiment is a high as 55. This value will be used as an input data in the numerical modeling developed and described in chapter V.

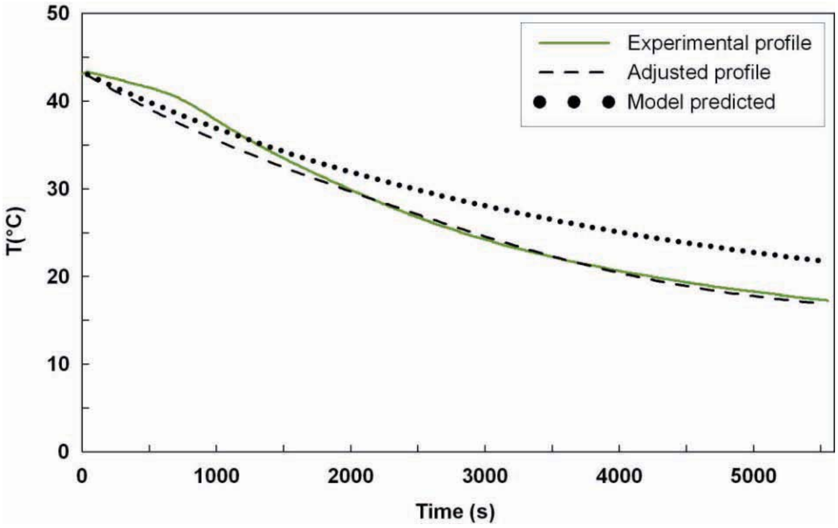

Figure (III.9) - temperature evolution at Z = 170 mm inside a bed of particles preheated at 45 °C.

Chapter IV

Experimental results and discussion

The fourth chapter presents the results obtained using the experimental device developed. This chapter is divided into two main parts:

- The first one presents the results from the experimental device filled with a "simple" medium used to calibrate the cell: charcoal/sand mix. A mass balance of the combustion process is described and validated.

- The second part concerns the combustion of an oil shale/sand mix. There, a reference case is exhaustively studied. It is described a general observation during and after combustion. The analyses of the solid residue after combustion and the flue gas are shown; some comments about the shale oil recovery are made. The mass balance validated previously with the "simple" medium is used to propose a mass balance of the oil shale combustion process. Finally is presented the physical aspects of the propagation of a combustion front. In this section is proposed a study and evaluation of reactions zone thickness, based on the micro-sampling system developed specifically for this purpose.

IV.1 Combustion of model porous medium: Charcoal in sand

Oil shale is a complex reactive medium; its combustion involves drying, devolatilization, fixed carbon oxidation and carbonates decarbonation. Therefore, it was decided firstly to validate the combustion cell using as "simple" a model porous medium as possible. To simulate the fixed carbon, charcoal particles were used and mixed with sand. After combustion, the axial shrinkage of the bed was 16 %, which is not negligible.

A mass of 2340g of mix 3.6/96.4 wt. charcoal/sand was introduced in the cell. The experiments were run with an air flow rate of 9.5 l min^{-1}. This corresponds to a flow rate of 1461 l min^{-1} for $1m^2$ of section, and to a Darcy velocity of 0.024 m s^{-1} at 20.0 °C, or 0.108 m s^{-1} at 1000 °C.

IV.1.1 Thermochemical aspects

IV.1.1.A Chemical characterization of Charcoal

The char particles size is smaller than 10 mm. The granulometry and properties of the charcoal samples are given in Table (IV.1), by (Tagutchou, 2007). The particles were then ground to 500-1000 μm.

Properties		**Values**	**observations**
Granulometry	Size	2.5 < dp < 12.5mm	Measured
	Thickness	0.5 < e < 7mm	Measured
porosity		0.75	Measured
Solidy phase density		1600 kg m^{-2}	Measured
Apparent density		400 kg m^{-2}	Measured
BET surface area		87.11 m^2 g^{-1}	BET analysis
Micropore surface area		45.81 m^2 g^{-1}	Measured by mercure intrusion method
Specific surface area		25.51 m^2 m^{-3}	

Table (IV.1) - Granulometry and morphological properties of charcoal particles.

Proximate and elemental analyses of the sample are given in Table (IV.2). The charcoal contains approximately 92 % of carbon. The residual volatile matter of the prepared char was approximately 5.0 %.

Proximate analysis (%wt.)				**Ultimate analysis (%wt.)**				
Moisture	**VM**	**Ash**	**FC**	**C**	**H**	**O**	**N**	**S**
1,6	5,5	1,3	91,6	92	1,4	5,1	0,3	0,1

Table (IV.2) - Proximate and ultimate analyses of the charcoal from maritime pine.

IV.1.1.B Exit gas analysis

During the experiments with the cell of combustion, the composition of the flue gas at the cell exit was established. The species O_2, CO, CO_2, SO_2 and NO were analyzed using a NDIR analyzer, Figure (IV-1).

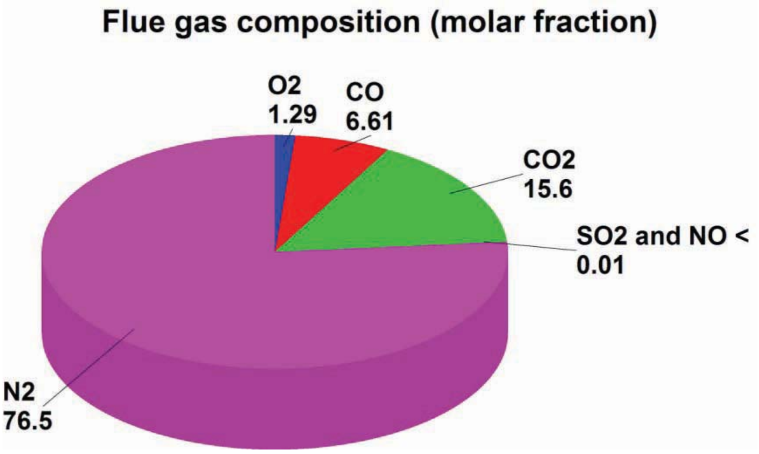

Figure (IV-1) - Flue gas composition at the cell of combustion exit.

The fixed carbon is converted into CO and CO_2. According to the analysis of the solid residue, no more carbon was present (less than 0.05 % in the mix solid residue + sand). In this case, all the fixed carbon was oxidized. Approximately 1.3% of O_2 remains in the exit gas. The gas species SO_2 and NO from volatile matter are present in negligible quantities. These results will be used further to establish a mass balance of the front propagation process.

IV.1.2 Physical aspects

IV.1.2.A Temperature of the bed

Figure (IV-2-a) shows the temperature evolution at several locations inside the bed for two experiments in the same conditions. For thermocouple T1, a peak close to 610 °C was observed. For the other thermocouples placed along the axis (T2, T3, T10, T11, T12), temperature peaks were observed near to 1050 °C.

On the horizontal cross section at mid-point of the height of the bed (T4 to T9), one can see that the temperature peak has fallen to 930 °C: the temperature difference compared to the axis of the bed is about 120 °C. This reveals significant heat losses through the walls.

The peak temperature is reached at the same time for all thermocouples of the crown, indicating that the front propagated as a horizontal surface. Moreover, the peak time for all thermocouples of the crown is midway between T3 and T10 peak time. This indicates that the front was a plane surface.

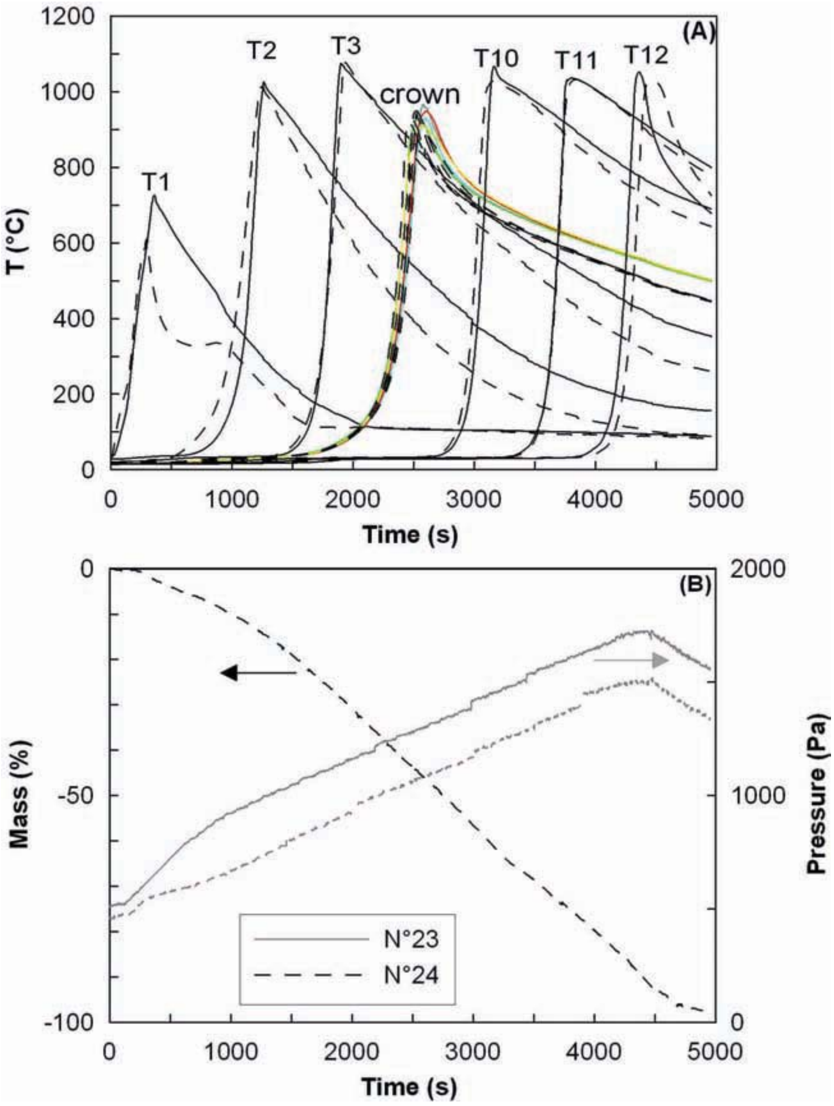

Figure (IV-2) - (a) Temperature evolution of the thermocouples placed along the axis and placed a horizontal cross section. (b) Mass and pressure evolution in the bed.

IV.1.2.B Pressure evolution at the top of the bed

Figure (IV-2-b) shows the temporal evolutions of the pressure at the top of the particle bed for two experiments. The pressure increased almost linearly along the experiment, and decreased slightly at the end. An explanation might be that the permeability of the bed decreases as the charcoal particles are oxidized, leading to the rearrangement of the particles inside the bed. Another explanation might be that the average temperature level inside the bed increases with time, increasing the gas velocity and viscosity.

IV.1.2.C Front propagation velocity

The velocity of the front was determined from the data of passage at each thermocouple on the axis of the cell. A quadratic polynomial function giving the position of the combustion front versus time was fitted to the experimental points, as illustrated in Figure (IV-3-a). The r^2 was better than 0.995. The time derivative of this function is the velocity of the combustion front, as shown in Figure (IV-3-b). As indicated by the plots, the velocity of the front increased from 3.21 mm min^{-1} at the beginning of the experiment to 4.84 mm min^{-1} by the end.

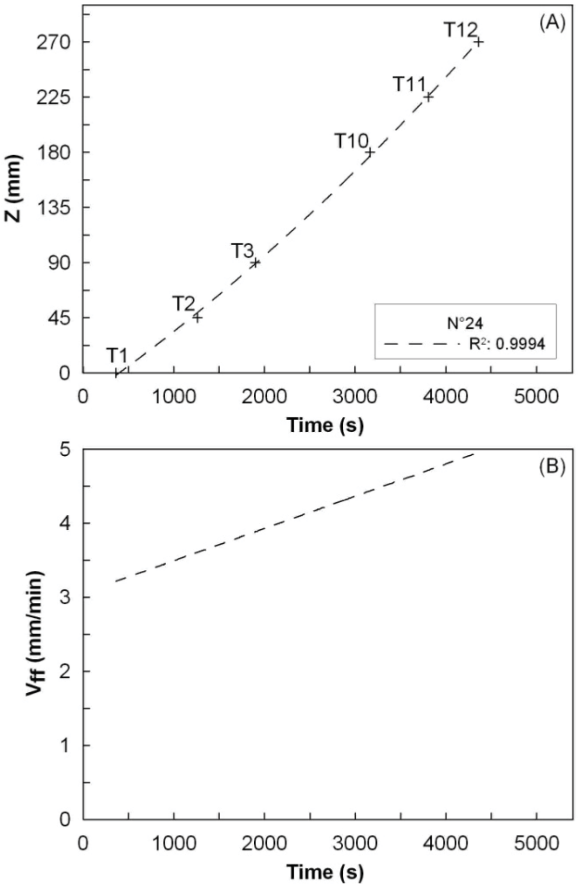

Figure (IV-3) - (a) Curve fitting with its 1st derivative at time. (b) Combustion front velocity.

As a synthesis of these validation tests, its can be concluded that the cell enables to follow the front progress. The shape of the front was a plane surface propagating horizontally. Flue gas analysis was possible and repeatable. Regarding the pressure at the top of the bed and the bed mass was successful.

IV.1.2.D Instantaneous mass balance

An instantaneous mass balance of the combustion process was established. One can expect two types of results from an instantaneous mass balance:

(i) To check that a mass balance of carbon species is closed;

(ii) To determine the respective proportions of CO and of CO_2 resulting from carbon oxidation.

The mass balance established here consists in calculating the composition of the flue gas out of the cell. Detailed of the calculation are given in Appendix A. The calculated values will be compared with the values measured experimentally. It was assumed that there was no volatile matter in the charcoal (measurements show less than 5.0 %). The flue gas contains:

- the N_2 flow of the inlet air flow;
- the O_2 flow of the inlet airflow that was not oxidized;
- CO_2 and CO resulting from the oxidation of the charcoal, following the reaction (r.4) presented in chapter III (III.3).

During the experiment, and at time t = 1914 s, the front was located at Z= 90 mm (thermocouple 3), gases were sampled and analyzed. The front velocity was 3.89 mm min^{-1}. From this:

molar (%)	Experiments	Mass balance
N_2	76,50	76,66
CO	6,61	6,10
CO_2	15,60	15,68
O_2	1,29	1,56

Table (IV.3) - Mass balances results.

Results

Fixing the f_r coefficient at 0.28, the fractions of CO and CO_2 calculated from the mass balance are in very good agreement with the experimentally measured fractions. It can be concluded that the front propagation is sustained by the oxidation of all the fixed carbon. Moreover, 28 % of this carbon is finally retrieved as CO, while the rest is converted to CO_2.

IV.2 Combustion of oil shale

A mass of 2127 g of mix 75/25 wt. oil shale/sand was introduced in the cell. The experiments were run with an air flow rate of 9.5 l min^{-1} at STP; this corresponds to a flow rate of 1461 l min^{-1} at STP for 1 m^2 of section, and to a Darcy velocity of 0.024 m s^{-1} at 20 °C, or 0.108 m s^{-1} at 1000 °C.

IV.2.1 Products of the combustion

After combustion, the solid residue was recovered and the flue gases were analyzed.

IV.2.1.A Observation and analysis of the solid residue

Solid residue

The solid residue (of oil shale + sand) homogeneously occupies all the volume of the cell; its apparent density was 956.9 kg m^{-3}. No liquid oil deposited at the surface of the grains or impregnating the grains was observed. The particles were not sticky and were odorless, while the flue gases had a very strong smell.

Detailed analysis of the solid residue mix was carried out.

- The LOI under air at 550 °C was found at 0.622 %, corresponding to the residual fixed carbon amount.

- At 1000 °C the LOI - including residual fixed carbon oxidation and decarbonation of the residual carbonates - was 3.5 %. The mass loss of CO_2 was then 2.879 %, which is equivalent to a residual amount of $CaCO_3$ of 6.543 %.

A synthesis of these results is presented in Figure (IV-4). On the left-hand side, the composition of only oil shale is re-stated. The two vertical bars at the centre establish a link between the masses of components in 100 g of oil shale/sand mix before combustion, which lead to 74.5 g of solid residue after combustion. On the right-hand side, the composition of only the oil shale residue is given, i.e. excluding sand. It can be calculated that the front, at its passage:

- dries the oil shale integrally, which was expected as a trivial result;
- devolatilizes the organic fraction integrally;
- oxidizes 88.2 % of the fixed carbon that is formed (4.7 % of the initial oil shale);
- decarbonates 83.2 % of the initially present carbonates (34.66 % of oil shale).

The final mass loss of the oil shale was 33.0 %. The oil shale residue after combustion contained 0.84 % of fixed carbon, 8.82 % of CaCO3, 24.4 % of CaO and 65.82 % of inert.

Ultimate analyses were then performed on the solid residue. The amount of C was 1.8 %, which is compatible (taking measurement errors into account) with the value of 0.84 % determined previously. H was found at 0.1 % and O at 1.1 %, confirming that devolatilization was completed. Less than 0.05 % N and 0.68 % S were found. The O content is 1.1 %. Again the O contained by the residual CaCO3 is not taken into account by the measurement.

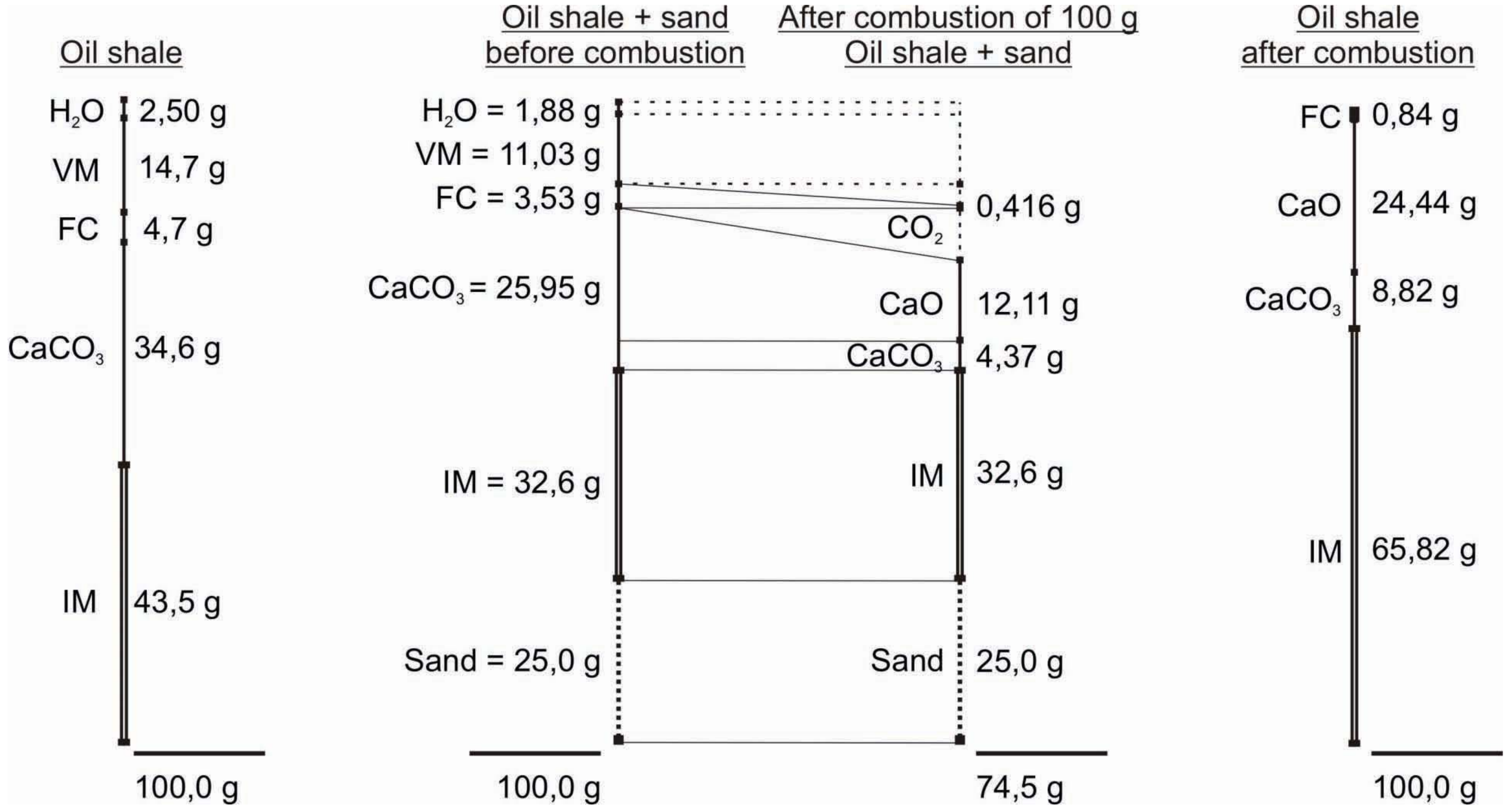

Figure (IV-4) - Synthesis of the characterization of oil shale and oil shale after combustion. Where: volatile matter (VM), fixed carbon (FC) and inert matter (IM).

IV.2.1.B Observation and analysis of the flue gas

The smoke was transparent until the front reached Z=180mm; it then started to change of color to a dense white, and condensation of water appeared inside the tubes. A few minutes after that, the smoke became yellow and at the same time, the first oil drops fell down inside the container.

Figure (IV-5) illustrates the transformations of oil shale and the reaction with air to form the flue gas, indicating the origin of each species. It also reports the results from analysis of the dry flue gas.

The amount of oxygen is small: 0.59 % when air (20.86 % O_2) was supplied. This indicates that the front consumes almost all of the oxygen, and is therefore limited in velocity by oxygen supply. This can be considered as an important result from this work.

The amount of methane is 0.99 %, that of NMHC of 3.14 % (equivalent C) and that of CO 7.44 %. From this, and assuming that the NMHC has the same LCV as methane, the lower calorific value of the flue gas can be estimated at 54 kJ mol^{-1}.

IV.2.1.C Liquid oil produced

At the end of the experiment, liquid oil was recovered in the reservoir; see Figure (IV-6).

The oil tended to be separated into different phases. Clear water was observed at the bottom, while a second black phase was floating; a third very viscous phase lay at the bottom. The analysis of oil is complex and was not undertaken.

After separation from clear water, the mass of oil was 160 g. In other words 52 % of the mass of organic matter initially present in oil shale is recovered as oil. It is interesting to note that this value corresponds with the amount of formed oil deduced from characterization of devolatilization, 53 %; see chapter (III.4). Nevertheless, this correspondence should not be considered as ordinary, since the oil formed in the combustion cell at pyrolysis can be cracked downstream into permanent gas or oxidized.

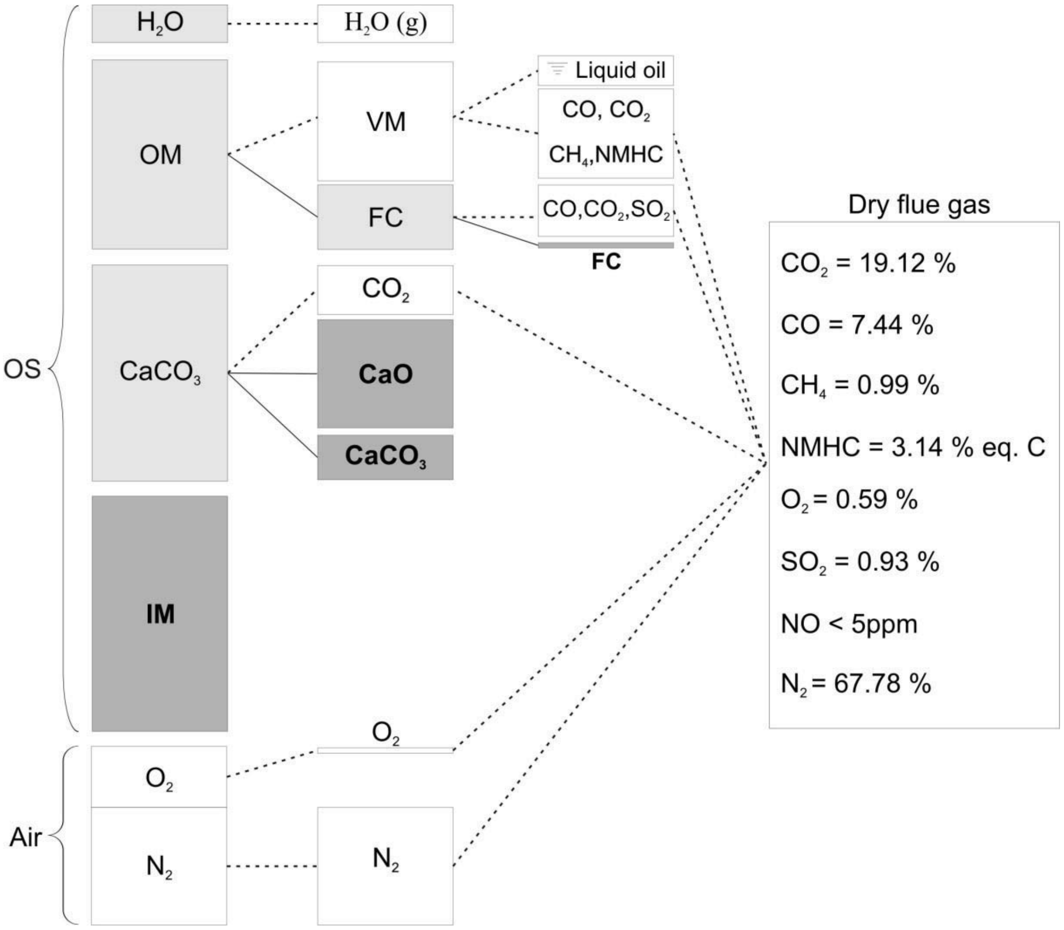

Figure (IV-5) - Description of the conversion of oil shale and air to produce the flue gas. On a dark color the components of oil shale solid residue.

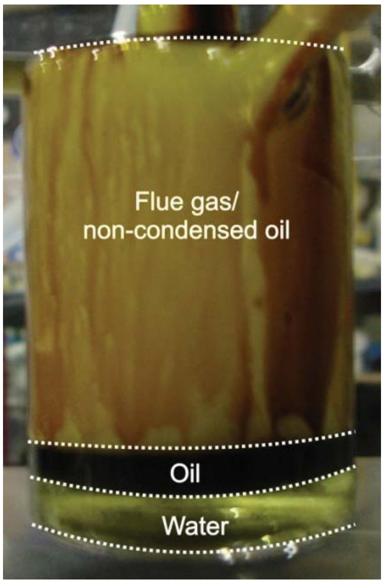

Figure (IV-6) - Shale oil recovery during experiments.

IV.2.1.D Instantaneous mass balance of the process

One can expect two types of results from an instantaneous mass balance:

(i) Several clues can be found in investigation of what is actually oxidized – part of the fixed carbon and potentially part of volatile matter – during the front propagation.

(ii) It should be possible to determine the respective proportions of CO and of CO_2 resulting from carbon oxidation.

The mass balance established here consists in calculating the composition of the flue gas out of the cell. The calculated values will be compared with the values measured experimentally. As illustrated in Figure (IV-5), the flue gas contains:

- the N_2 flow of the inlet air flow;
- the O_2 flow of the inlet airflow that was not oxidized;
- H_2O resulting from the drying of oil shale;
- CO_2 and CO resulting from:
  - direct production of the devolatilization;
  - the oxidation of part of the fixed carbon, following the reaction (r.4).
- CO_2 resulting from the decarbonation of carbonates;
- Volatile matter.

We assume here that there is no oxidation of volatile matter and of oil. During the experiment, and at time t = 2079 s, the front was located at Z= 90 mm (thermocouple 3), and gases were samples and analyzed. The front velocity was 3.68 mm min^{-1}. From this:

- The flow rates of volatile matters, of oil, and of formed fixed carbon were calculated using the partitioning established in the analysis of the devolatilization gas;

- A fraction of 88.2 % of the fixed carbon – as determined previously - was allowed to react with oxygen from the air supply;

- Carbonates were allowed to decarbonate by 83% corresponding with the value determined in the section IV.2.1.A.

The molar composition of the flue gas was calculated, and is reported in Table (IV.4).

	From Experiments	From Mass balance
O_2	0,59	6,66
CO	7,44	7,44
CO_2	19,12	19,18
CH_4	0,99	0,88
NMHC	3,14	3,70
N_2	-	60,72

Table (IV.4) - Composition of the flue gas (vol. %) as determined from analysis and as calculated from the mass balance.

Results

Fixing the f_r coefficient at 0.565, the fractions of CO and CO_2 calculated from the mass balance are in very good agreement with the experimentally measured fractions. It can be concluded that the front propagation is sustained by the oxidation of the fixed carbon only, i.e. that no volatile matter are oxidized. Moreover, this indicates that 56.5 % of this carbon is finally found as CO, while the rest is converted to CO_2.

Considering the amounts of CO_2 that are formed, it can be established from this mass balance that CO_2 from decarbonation of carbonates represents 69 % of the total CO_2 emissions, i.e. including CO_2 from FC oxidation.

If one considers the mass balance of oxygen species, the balance predicts 6.66 % residual O_2 in the flue gas, while 0.59 % is found experimentally. This would suggest that some O_2 has been consumed by another reaction not considered here. This reaction might be the one identified during DSC experiments, where a first exothermic peak was observed before the char oxidation peak. The improvement of the mass balance of oxygen species remains a perspective of this work.

Focussing on both the amounts of CH_4 and NMHC, the values calculated from the mass balance are closed to the experimental values. This indicates that these species, once formed during the devolatilization, are driven out of the cell without significant transformation, which confirms the conclusion that only fixed carbon is oxidized.

An energy balance can be established, based on:

- the LCV of the oil shale – measured at 6.0 MJ kg^{-1};

- the energy contained in the flue gas;
- the energy consumed by fixed carbon oxidation;

The oxidation of fixed carbon into CO and CO_2 consumes 10 % of the energy contained by the oil shale, while the fixed carbon left in the oil shale residue represents only 2.3 %. The flue gas calorific value energy represents 17 % of the oil shale energy.

IV.2.2 Physical aspects

IV.2.2.A Temperature of the bed

The values obtained at different locations inside the bed are reported in Figure (IV-7-a). The model developed further indicated that thermal equilibrium was achieved by following the measurement of the temperature that was the same for the solid phase and for the gas phase.

For thermocouple T1, close to the bed surface, a peak at about 750 °C was observed. After ignition at the surface, a combustion front started to self-propagate downward in co-current through the bed. For the other thermocouples placed along the axis (T2, T3, T10, T11, T12), peaks at a temperature near 1100 °C were observed. This temperature is comparable to that obtained during the calibration tests made with a charcoal/sand mix, where the amount of fixed carbon was similar.

On the horizontal cross section at mid-height of the bed and 11 mm away from the wall (crown thermocouples, T4 to T9), one can see that the peak temperature was about 180 °C lower than at the axis. This reveals that a pure 1D situation was not achieved, which can be attributed to significant heat loss at the walls of the cell. A global heat balance was established to estimate the heat loss over all the combustion process. The details of the calculation are given in Appendix B. It was found that approximately 42 % of the heat released by the combustion of the fixed carbon of oil shale was lost. Despite the quite large diameter of the fuel bed (91 mm) and the thickness of the insulation material around it, the heat losses were not negligible. This observation indicates that in experiments from the literature where the combustion front is observed in non-insulated transparent smaller-diameter reactor tubes, the heat losses were probably much higher, and significantly affected the front structure and propagation.

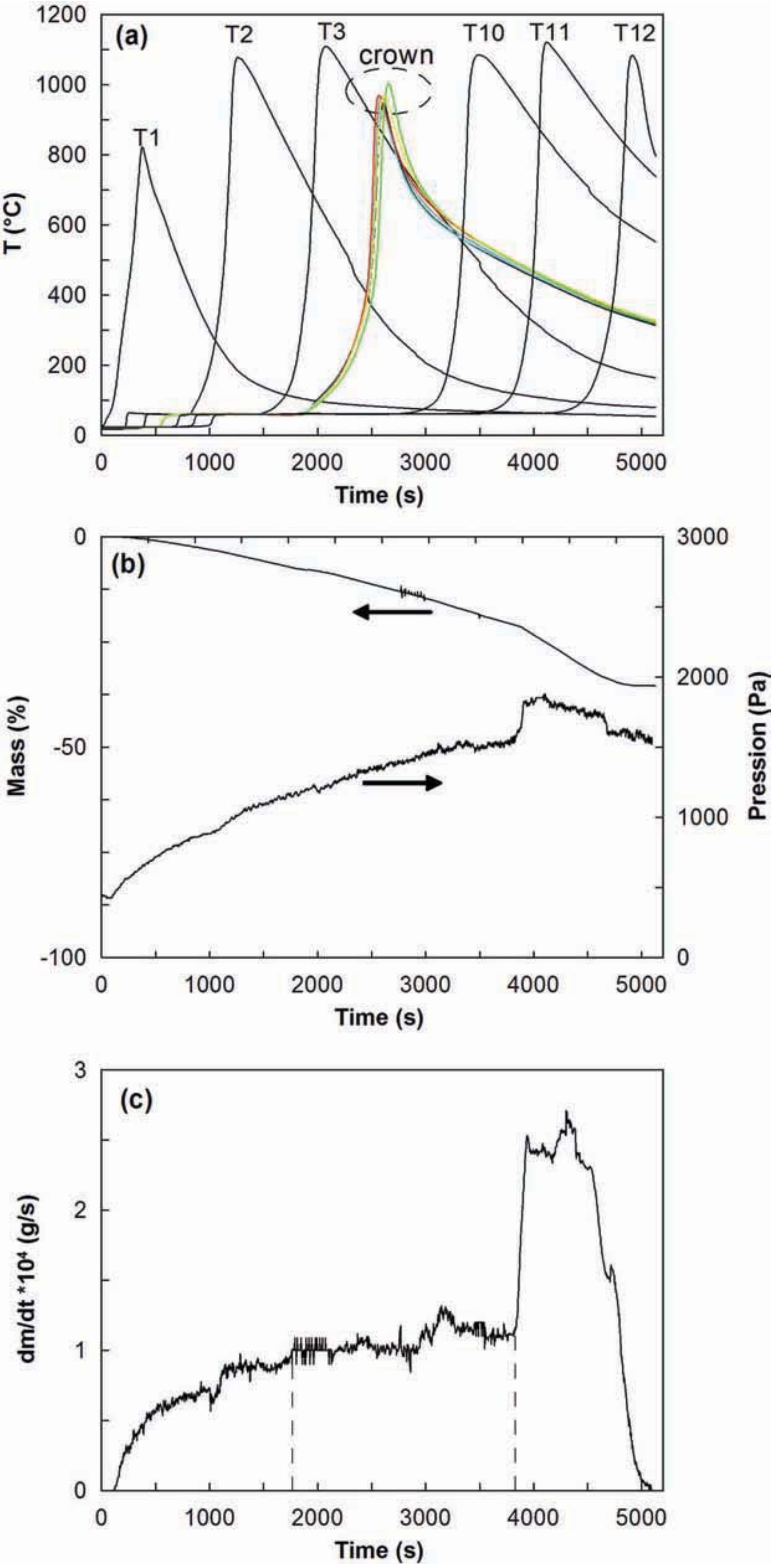

Figure (IV-7) - (a) Temperature evolution of the thermocouples placed along the axis (T1, T2, T3, T10, T11 and T12) and placed a horizontal cross section (crown). (b) Mass and pressure evolution in the bed. (c) Derivative of the mass evolution in the bed.

The heating rate inside the bed at the arrival of the front was between 60 and 90 K min^{-1}. This is much higher than the operating hate in a standard TG experiment, but it is within the range operational range of the horizontal tube furnace that was used to determine the amount of fixed carbon: 50 to 900 K min^{-1}.

Figure (IV-7-a) also shows a very clear phenomenon observed during the experiments. The temperatures at different positions of the bed all stabilized at a very constant temperature of 60 °C until the combustion front approached. This can be compared with the observation of a DTG peak at the same temperature of 60 °C during the test at 10 K min^{-1}. It is probable that this peak is due to the endothermic phase change that was not identified, but probably not due to drying of the oil shale.

Observing the dispersion of results during repeatability tests brought some insight into the probable mechanisms involved. In the case of oil shale/sand tests, the difference between the peak times at a given location, Figure (IV-8), might be explained by the complex flow developed in the cell, caused by the conversion of solid kerogen into liquid oil and then into gas, (Hansom and Lee 2005), generating overpressures in the bed. This clogging results in disturbance of fluid flow across the porous medium. One can verify this by observing Figure (IV-2) for charcoal/sand tests: for the “simple” medium, the temperature peak time results are coincident when the test is repeated.

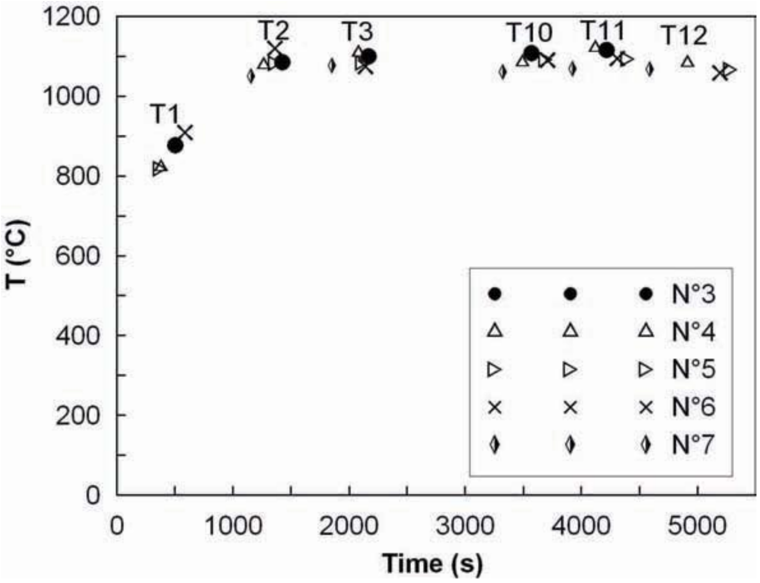

Figure (IV-8) - Axial temperature peak for five trials.

Figure (IV-9) shows axial temperature profiles along the reactor axis at different times.

This was obtained by plotting - at the peak time for each thermocouple - the temperature values for all thermocouples. Extrapolation curves around each thermocouple were obtained from the temperature values before and after the peak time, and using the front velocity to calculate the position of the thermocouple relative to the Temperature Peak Point (TPP) at each time. The temperature decrease downstream of the TPP (right hand side of TPP) keeps quite a constant shape at different times, while the hot zone upstream of the front becomes getting larger as the front progresses.

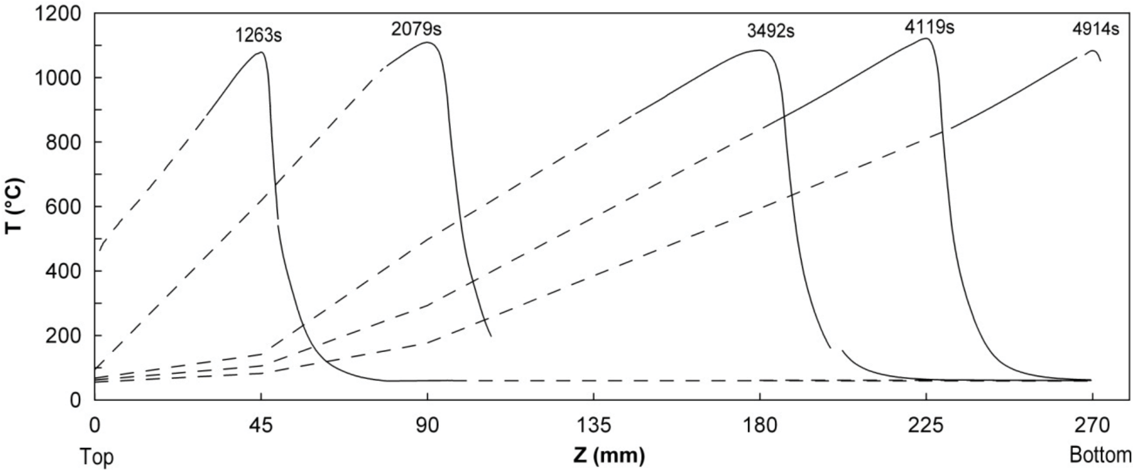

Figure (IV-9) - Axial temperature profiles along the axis of the cell at different times.

From the temperature profile at a given time (4119 s for instance), a first geometrical description of the front structure can be established, as follows:

- If one assumes that drying becomes very fast and is completed rapidly when the temperature reaches 150 °C, the drying zone can be localized downstream of the TPP, starting 18 mm from the TPP as illustrated in Figure (IV-10).

- Devolatilization can be assumed to progress significantly as the temperature reaches 250 °C, and to be very fast at 550 °C. Consequently, the devolatilization zone can be localized between 7 mm and 13 mm downstream the TPP; its thickness is as small as 6 mm.

- For fixed carbon oxidation to occur, the temperature must be higher than 550 °C, and oxygen must be present. Air is fed from upstream of the combustion front (small Z), and several percentage of O_2 are still present at the exit of the cell. The zone where the two criteria are satisfied ranges from very small Z to Z = 7 mm. Nevertheless, at small Z, there is probably no more fixed carbon present. It is not possible at this stage to localize where the oxidation has the highest rate, although this is probably around the TPP.

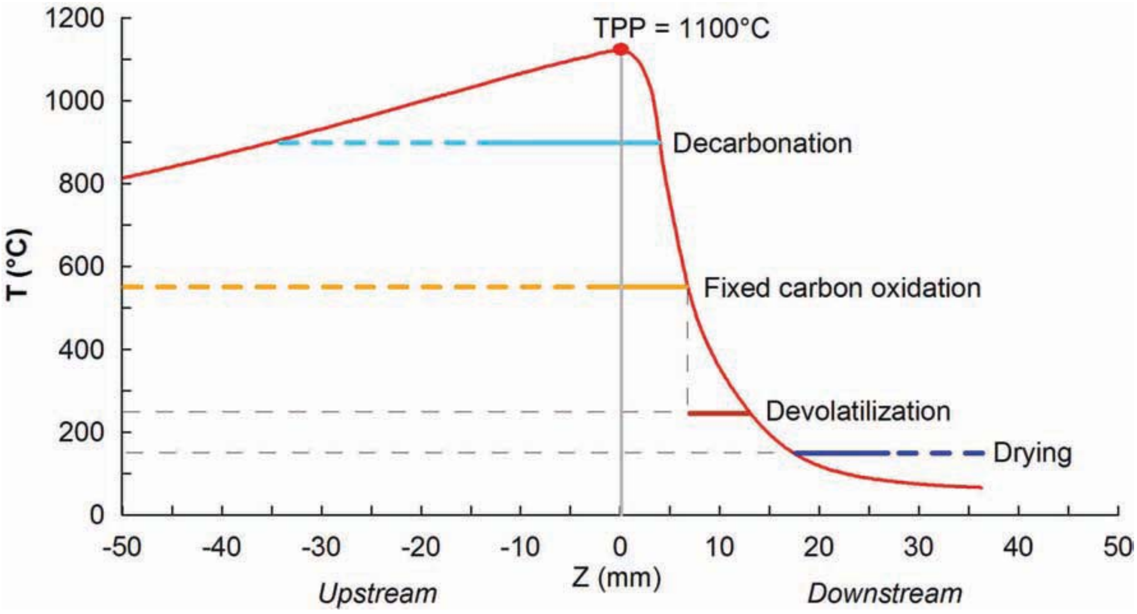

Figure (IV-10) - Front structure evaluated from temperature profile.

- Decarbonation of carbonates operates at a significant rate for temperatures above approximately 900 °C and as long as carbonates are present. The decarbonation zone is thus possibly located along 34 mm upstream of the TPP, and also downstream, along 4 mm.

IV.2.2.B The combustion front

Direct observation of the front

In an experiment, the combustion process was quenched with N_2, freezing the combustion front at mid-height of the cell. After impregnating the porous medium with a resin and making vertical cuts. It was possible from this experiment to visualize a clear difference in the color of the medium before and after passage of the front; Figure (IV-11) shows the photograph. The thickness of the transition zone is 3-6 times the average particle size. Nevertheless, it remains difficult to interpret this image in terms of thickness of the reaction zones.

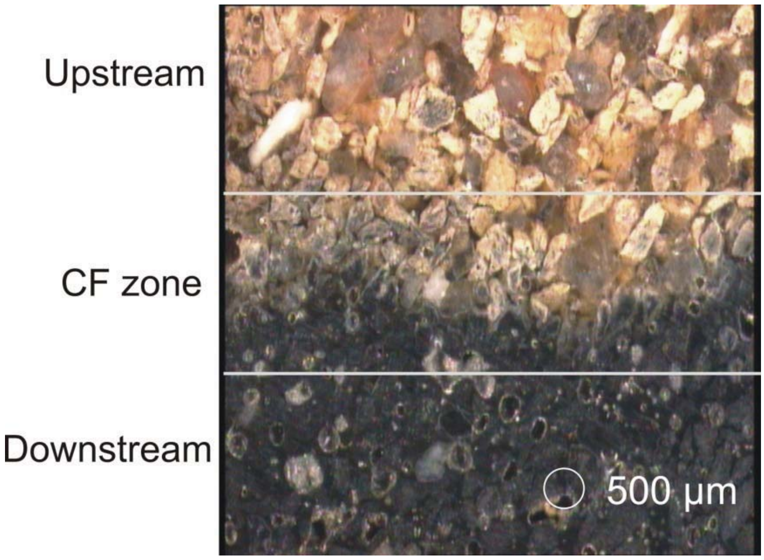

Figure (IV-11) - Photography of combustion front.

Chemical structure

The *chemical thickness* of the front was also investigated using the micro-sampling system. Figure (IV-12) summarizes the results obtained in term of the composition of the gas at different locations inside the front. It was particularly difficult to sample the 8 syringes over the appropriate period of time, i.e. when the front is passing at the sampling point inside the cell. Indeed, the front was not a plane surface and not horizontal as described later. In order to put together the results from different experiments, the experimental values are represented with space as the *X* scale, and relative to the TPP. As can be seen in Figure (IV-12) the results are quite scattered. Nevertheless, the average value of the CO_2 fraction downstream of the front (left hand side) is around 20 %, corresponding to the value obtained sampling the flue gas at the exit of the cell (19 %).

- As far as CO is concerned, its origin is fixed carbon oxidation only. The amount of CO released by devolatilization is negligible when compared with CO formed by fixed carbon oxidation. From the observation of the curve, it can be established that the oxidation is essentially concentrated in the zone up to 10mm downstream of the TPP. This is in good agreement with the first description proposed before. It is now possible to locate the upstream limit of the oxidation zone at the TPP: in all probability there is no more fixed carbon upstream of this point.

- CO_2 originates from the oxidation of fixed carbon but also from the decarbonation of calcite, in significant proportion, Figure (IV-12). The plot indicates that CO_2 is formed in a zone slightly larger than the zone for CO formation: the decarbonation zone spreads from 5mm upstream of the TPP, where the temperature is as high as 1100 °C. The fact that CO_2 is not released upstream of this point indicates that carbonates are not present anymore, i.e. the decarbonation has been completed. As far as the downstream limit of this zone is concerned, it seems not to extend further than 10 mm downstream of the TPP.

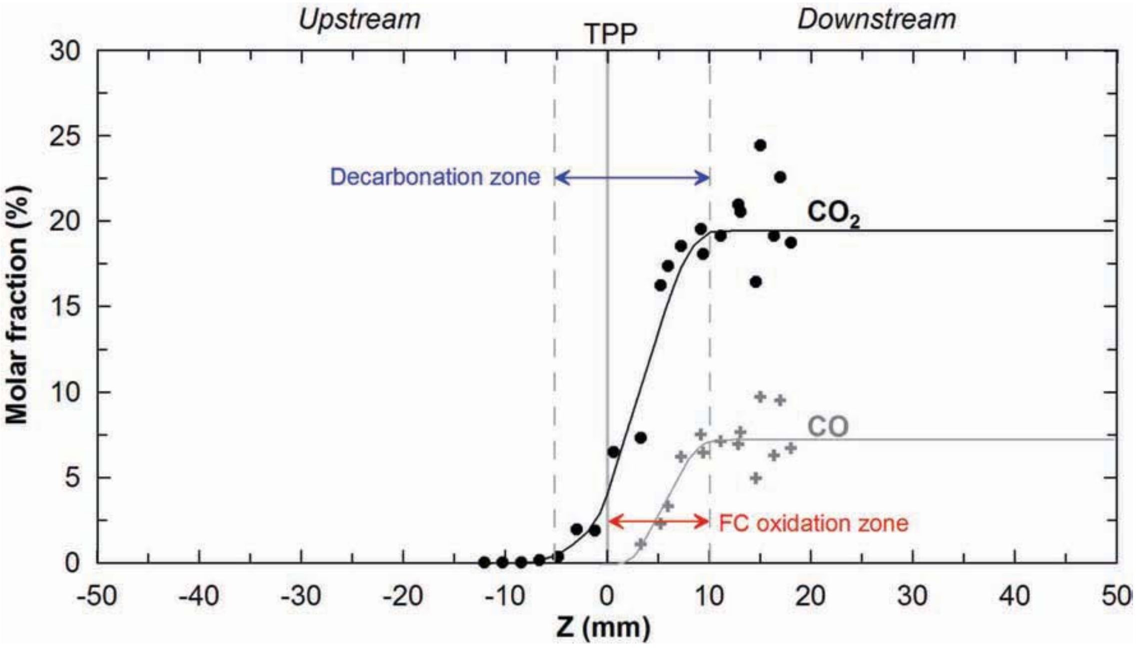

Figure (IV-12) - Results from different experiments with micro-sampling.

Shape of the front

Significant time duration separates the passage of the front (temperature signals) at the different thermocouples of the horizontal crown: the combustion front is thus not horizontal but inclined. From the propagation front velocity, and from the time separating the first peak and the last peak of the thermocouples crown, the slope of the front was evaluated at 4°, varying between 1° and 7° during repeatability tests. The fact that the front was not a horizontal surface may result from a non-uniform radiative heat flux during ignition. This explanation, however, cannot stand because as shown further, the front remains a horizontal surface during the combustion of a charcoal/sand mix. Therefore, a complex situation involving gas/oil condensations and re-evaporation is probably responsible for the front inclination in the case of oil shale. Instabilities due to the ignition process or heat loss through the walls may also explain the front inclination.

Moreover, looking at the results in Figure (IV-7-a), it is clear that the front reached the first thermocouple of the crown earlier than it probably reached the axis of the cell at the same Z, i.e. probably at the midway between the time for T3 peak and the time for T10 peak. This result indicates that the front was not a plane surface, but a curved surface with the top at the axis of the cell. Consequently, the front probably has the shape illustrated in Figure (IV-13), where three location (o) were plotted of the temperature peak at the time when the front passes at the axis of the cell at Z= 135 mm. One explanation might be that the front progress is controlled by O_2 supply, as demonstrated later. The mass flow rate of O_2 close to the cold walls is probably higher than at the axis because:

- the density of O_2 is higher, about 16 %, due to the lower temperature;
- the viscosity is smaller, about 10 %, also due to the lower temperature,
- the arrangement of particles in contact with the walls is not as dense as in the rest of the cell.

This might explain the more rapid progress of the front at the walls of the combustion cell.

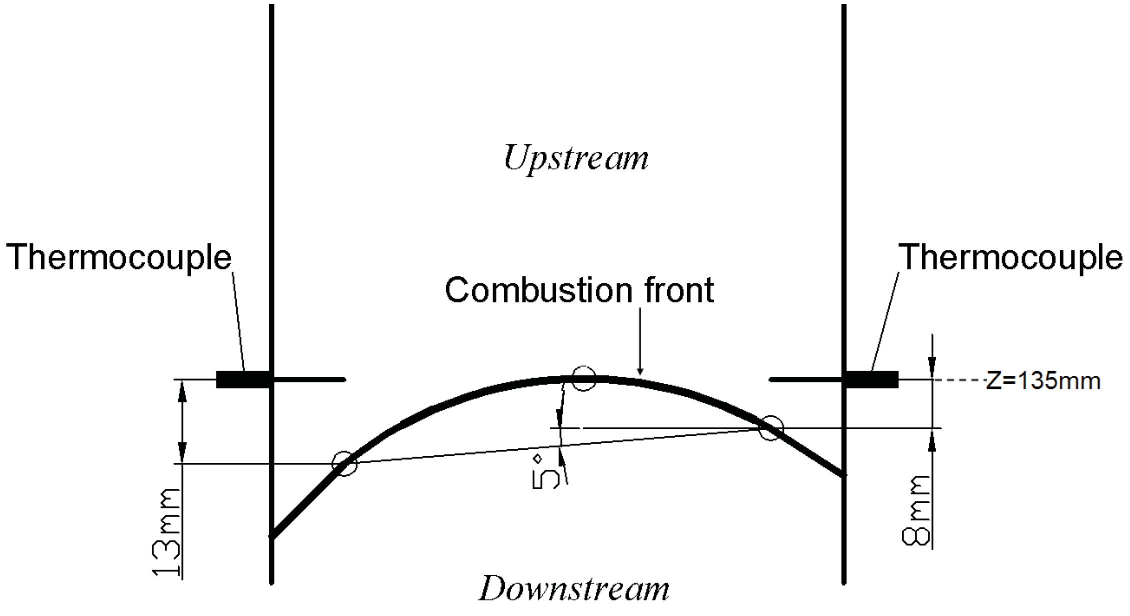

Figure (IV-13) - Shape of the front.

IV.2.2.C Pressure drop of the particle bed

As illustrated in Figure (IV-7-b), the pressure at the top of the bed first progressively increases from 500 Pa to 1500 Pa. After that, one can observe a rapid increase to 1800 Pa and a rapid decrease at the end of the test. The progressive increase might be explained by two phenomena:

(i) the temperature increase of the medium, as was confirmed from the experiments with charcoal/sand;

(ii) the progressive formation of an oil bank pushed by the combustion front or the clogging of the medium by oil deposits and porosity decrease. By the end of the test, the oil is evacuated at the bottom of the cell, explaining the rapid decrease in the pressure. Indeed, a flow of liquid oil at the bottom of the cell was observed starting at t = 3490 s, i.e. some time before the rapid pressure increase.

IV.2.2.D Mass loss of the particle bed

The evolution of the fuel bed mass is reported in Figure (IV-7-b). It is shown here that when liquid oil arrives at the bottom of the cell, it is evacuated to a container and not weighed with the rest of the cell. It is clear that the mass loss rate (slope of the curve) was not constant along the process. After 4900 s, the mass stopped decreasing.

The derivative of fuel bed mass gives a better reading. It was calculated using the recorded mass data and by smoothing the curve with a time step of 15 s; the results are shown in Figure (IV-7-c). Looking carefully at the results, one can distinguish three domains along the process:

(i) A starting domain, up to 1750 s during which the mass loss rate increases. This is attributed to the fact that the front at the very beginning is not hot enough to cause calcite decarbonation;

(ii) A more or less stable propagation domain, from t= 1750 s to t= 3800 s. Along this domain, the mass loss rate increases by only 14 %;

(iii) A perturbed domain after 3800 s, in which the mass loss rate rapidly increases and then rapidly decreases.

It is interesting to note that these three domains can also be observed – with time synchronization – on the bed top pressure curve. This would corroborate the explanation of the oil bank evacuation by the end of the process, explaining both the pressure drop loss and the high mass loss rate.

The stop of the front is not exactly sudden: it takes approximately 500 s for the mass loss rate to fall down to 0.

IV.2.2.E Velocity of the front

The velocity of the front calculated from the times of TPP at the different thermocouples on the axis is reported in Figure (IV-14) for all experiments. The results for the reference experiment are highlighted using a bold line.

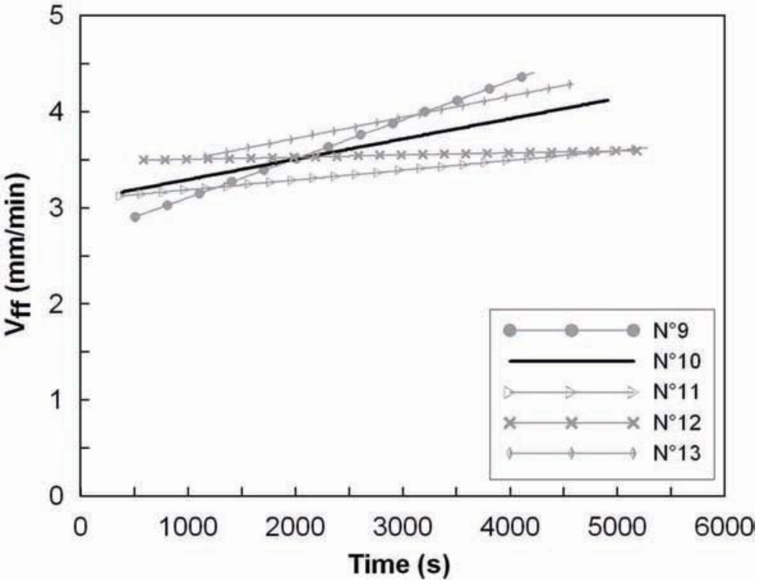

Figure (IV-14) - Repeatability trials of the combustion cell.

The front propagation velocity is 3.1 mm min^{-1} at the beginning of the experiment, and increases to 4.0 mm min^{-1} at the end. For the charcoal/sand tests, the propagation front velocity at the beginning was about 3.21 mm min^{-1} and at the end it increased to 4.84 mm min^{-1}. These values are comparable with oil shale/sand experimental results; this result is consistent with the fact that the front propagation is controlled by stoichiometry of fixed carbon oxidation, and that the mass fraction of fixed carbon was comparable for the two media. These values are characteristic of the smoldering propagation velocity. The repeatability tests for oil shale/sand combustion show that the increase in the velocity of the front is always observed, although some differences can be seen from one test to another. A probable explanation for the velocity evolution is a progressive change in the molar CO/CO_2 ratio produced by fixed carbon oxidation, which means a decrease in CO_2 production in favor of CO production. This enables the oxidation of a greater number of carbons with a given amount of O_2.

IV.2.2.F The physical state of oil

It is difficult to establish under what physical state – gas or liquid, adsorbed or not on the solid oil shale particles – the oil is transported through the porous medium downstream of the front. Eq. (IV.1) should be valid if there is no accumulation of matter (here, oil) inside the bed. The apparent density of the oil shale/sand mix was measured before (ρ_i) and after (ρ_p) the passage of the front, and U_f was calculated and plotted in Figure (IV-15). U_f calculated from the position of the TPP was also plotted in Figure (IV-15) as the actual front velocity.

$$U_f\left(\rho_i-\rho_p\right)=\frac{dm}{dt} \tag{IV.1}$$

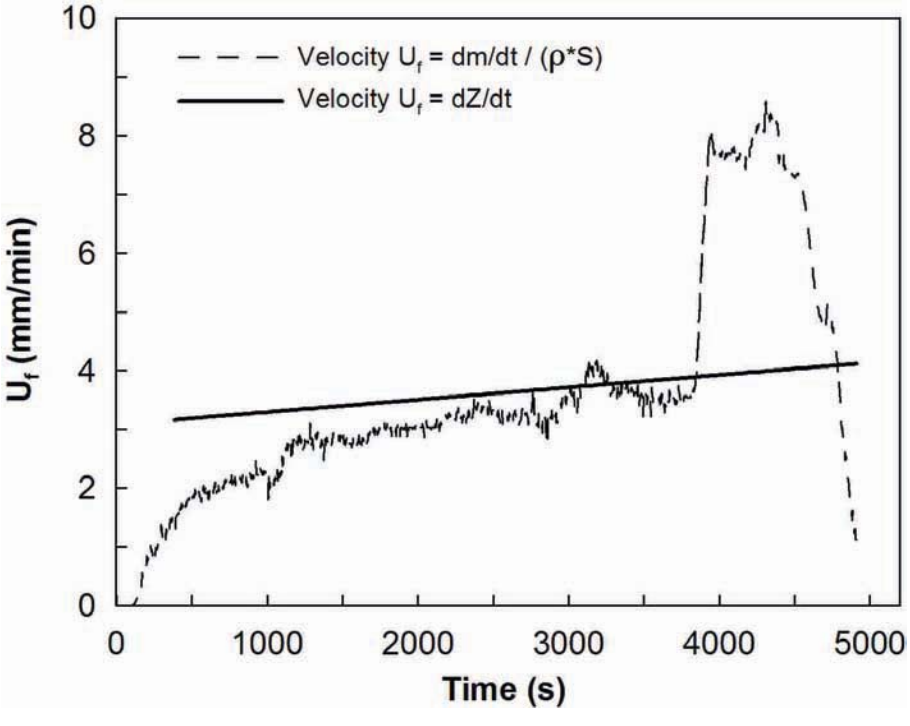

Figure (IV-15) - Two approaches to evaluate the front velocity.

The figure indicates that the front velocity as calculated from eq. (IV.1) is first lower than the actual velocity: this indicates that accumulation of oil occurs during this phase of the propagation process. Later on, as the front progresses, accumulation of oil is no longer possible; the oil is driven out from the cell by the end of the experiment, when the velocity deduced from eq. (IV.1) becomes higher than the actual velocity. A specific experiment was made to obtain information about the physical state of oil adsorbed in the porous medium. This experiment was stopped as the front reached the mid-height of the cell by switching the air feed to N_2. No liquid oil was observed; the oil is probably adsorbed at the surface of the solid particles. Nevertheless, this result does not eliminate the possibility that when the front progresses further in the cell, the liquid oil can be present.

IV.3 Combustion cell development and complementary results

The combustion cell body was developed prioritizing two aspects:

(i) Looking for materials that accept the high temperatures reached during the experiments;

(ii) Looking for materials with the best insulating properties. The material which surrounds the packaged bed is determinant for the experiment: a too conductive material may cause the deformation of the flame front.

During this thesis, before obtaining the final reactor made of stainless steel, it was tested two other types of material: Mullite and Kaowool.

Figure (IV-16) - Photograph of the mullite reactor after the first experiment.

In the first trial was used a tube reactor made of mullite material, which has a quite small thermal conductivity (3.5 $Wm^{-1}K^{-1}$ at 1200 °C), but a low thermal shock resistance: reactor fissured in three parts, after passage of the front; see Figure (IV-16).

After, three other reactors were made using directly an insulating material: Kaowool HS 45 Board, Thermal Ceramics, with a very small thermal conductivity: 0.21 $W\ m^{-1}\ K^{-1}$ at 1000 °C. Nevertheless, water and oil impregnated the internal surface of the reactor, and it was observed a progressive deterioration of the cell along the tests, Figure (IV-17).

Facing these difficulties, the final reactor was made of stainless steel, as shown in chapter II.

Figure (IV-17) - Photography of the reactor wall, after passage of the front.

The tests performed with the different cells enabled to vary three parameters:

1. Oil shale mass fraction, in the range 35 to 100% (first row in Figure (IV-18));
2. Air velocity, in the range 0.024 to 0.061 $m\ s^{-1}$ (second row in Figure (IV-18));
3. Average particle size, in the range 400 to 1500 µm (third row in Figure (IV-18)).

The results are synthesized in Figure (IV-18), where the first column gives the peak temperature, the second the front velocity, and the last column gives the CO and CO_2 molar fraction in the flue gas. The test performed with the mullite and ceramic reactors caused a number of problems and were not repeated as in the case of tests with the final cell. These results should be considered more as trends than as accurate values.

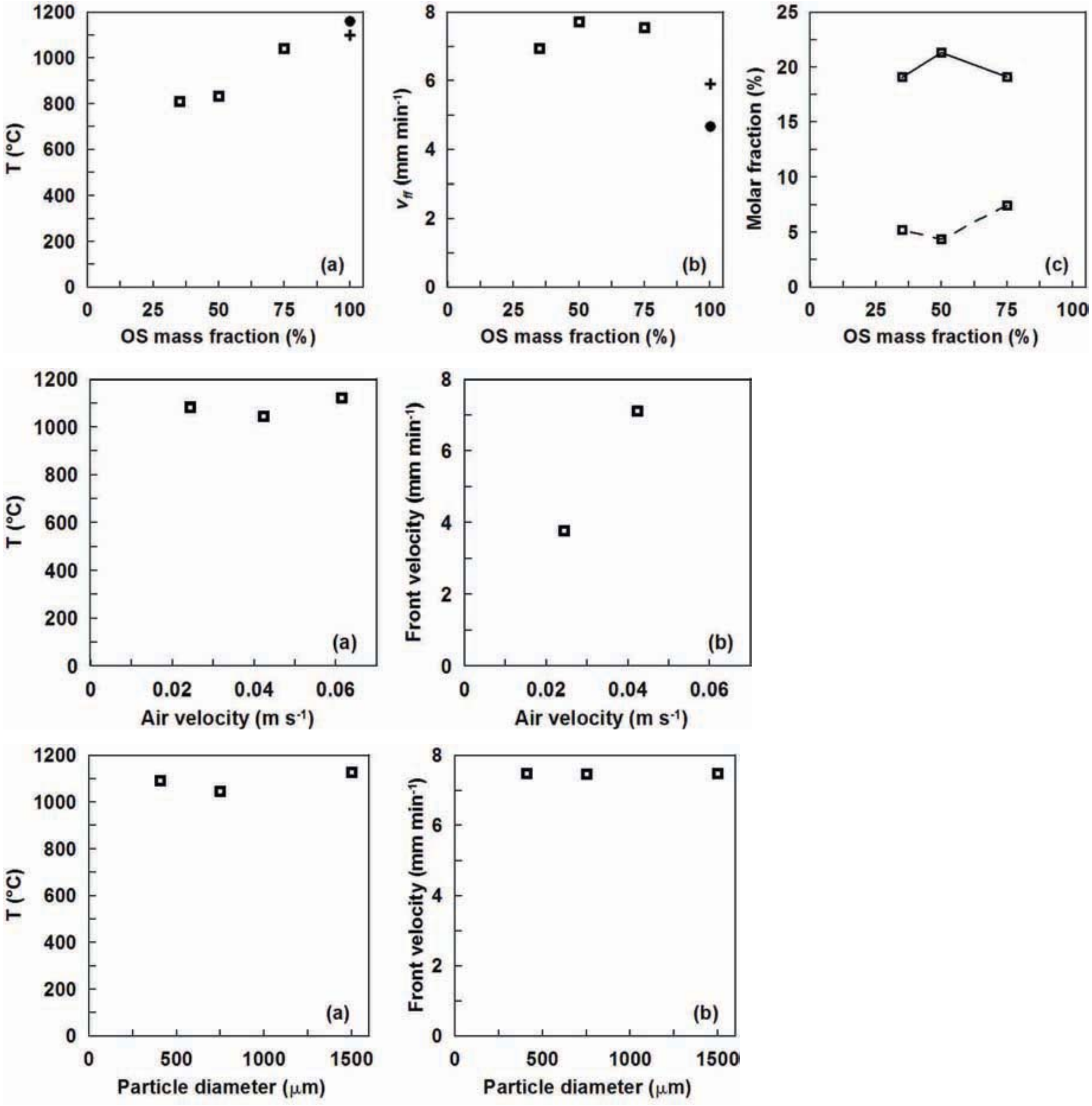

Symbols: (□) Stainless stell, (+) Mullite, (●) Ceramic, (—) CO_2, (- - -) CO

Figure (IV-18) – Peak temperature, front velocity and fraction of CO and CO_2 in the flue gas obtained experimentally varying the oil shale fraction, air velocity and particle size.

Performing the combustion of pure oil shale particle (without sand), the peak temperature was 1110 to 1160 °C, see first row in Figure (IV-18). Varying the oil shale fraction in the bed, it was seem that the CO and CO_2 molar fraction at the cell exit changes only a little; see Figure (IV-18).

When the air velocity was varied in the range 0.024 to 0.061 m s-1, it was observed that the front velocity is proportional to the entry air velocity; see Figure (IV.19), confirming a regime of oxygen-limited combustion.

Finally, when was varied the average particle size in the range 400 to 1500 µm, no effect of this parameter was observed on the temperature level in the reactor and on the front velocity.

Chapter V

1D numerical model

A complete mathematical model was developed by the "Institut de Mécanique des Fluides de Toulouse" (IMFT) team [(Lapene, Martins, et al. 2007), (Lapene, Debenest, et al. 2008)]. Briefly, to solve the heat transfer and the mass transfer equations simultaneously in the reactive porous medium, a homogeneous description at the Darcy-scale was used. Thermal local-nonequilibrium transport was allowed by the model, and treated with a two temperature model: one for the gas phase and another one for the solid phase. The chemical reactions considered are oxidation of fixed carbon and decarbonation reaction.

V.1 Mathematical Formulation

V.1.1 Nomenclature

m	Mass
t	Time, s
A	Frequency factor, s^{-1}
R	Perfect gas constant, $J.K^{-1}.mol^{-1}$
x	Position in x-axis, m
P	Pressure, $kg.s^{-2}.m^{-1}$
K	Porous media permeability, m^2
Q	Heat reaction rate, $J.s^{-1}.m^{-3}$
M	Molar mass, $kg.mol^{-1}$
k_0	Reaction rate, s^{-1}
E_a	Activation Energy, J
T	Temperature, K

v	Velocity, $m.s^{-1}$
$\dot{R}$	Reaction rate, $kg.s^{-1}.m^{-3}$
C_p	Mass heat capacity, $J.kg^{-1}.K^{-1}$
S_{spec}	Specific surface, m^{-1}
d_p	Average particle diameter, m
Pe	Peclet number
D	Dispersion coefficients $m.s^{-1}$
h	Thermal loss through walls, $J.s^{-1}.m^{-3}.K^{-1}$
Y	Mass fraction

Greek Symbols

ε	Volume fraction
μ	viscosity, $kg.s^{-1}.m^{-1}$
Γ	exchange coefficient, $J.s^{-1}.m^{-3}.K^{-1}$
ρ	density, $kg.m^{-3}$
λ	thermal conductivity, $J.m^{-1}.s^{-1}.K^{-1}$
α	$[CO_2]/[CO]$ ratio
Φ	Radiative heat flux, $J.m^{-1}.s^{-2}$

Indices, exponents

*	*effective*
s	*solid*
k	*constituent k*
g	*gas*
k	$\{N_2, O_2, CO, CO_2, CaCO_3, Fuel\}$
$_T$	*thermal*
$_C$	*Chemical*
$_{amb}$	*Ambient*
$_{rad}$	*Radiation*

V.1.2 Simplifying hypotheses

Three hypotheses are proposed in the present model:

1. The problem is monodimensional:

This hypothesis allows making a numerically efficient code, taking into account the couplings between heat and mass transport and the mechanisms of the chemical reactions, and especially allowing a first approach of the numerical problem. From this hypothesis it can be deduced:

$$\nabla = \frac{\partial}{\partial x}$$

2. The porosity is constant in time and space:

This hypothesis is justified by the choice of the porous medium material. From this hypothesis it can be deduced:

$$\frac{\partial \varepsilon_g}{\partial x} = \frac{\partial \varepsilon_s}{\partial x} = \frac{\partial \varepsilon_g}{\partial t} = \frac{\partial \varepsilon_s}{\partial t} = 0$$

3. Perfect gas law:

This hypothesis is often considered and can be used because the pressure in the porous medium is around the atmospheric pressure. From this one it can be deduced:

$$P = \rho_g r T \text{ , where } r = \frac{R}{M_\beta}$$

Using these hypotheses and referring to the local-nonequilibrium model, it can be written a simplified system of conservation equations.

V.1.3 Conservation equations

In this thesis, it was modeled mass and heat transport in reactive porous medium using a homogeneous description at the Darcy-scale. Local non equilibrium transport of heat was treated with a two field temperature model, one for the gas phase and one for the solid phase.

It was assumed that the two phases of the medium were:

- Solid phase: Oil shale fixed carbon, $CaCO_3$, Inert matter and sand;

- Fluid phase: gases N_2, O_2, CO, CO_2;

The organic matter converted into oil was not considered.

Considering all the approximations, it was written the various balance equations as described below. The first is the mass conservation equation

1. Mass

- Continuity of the gas phase

$$\epsilon_g \frac{\partial \rho_g}{\partial t} + \frac{\partial}{\partial x}\left(\rho_g v_g\right) = \dot{R}_g \tag{V.1}$$

- Species transport

$$\epsilon_g \frac{\partial \rho_g Y_k}{\partial t} + \frac{\partial}{\partial x}\left(\rho_g v_g Y_k\right) - \frac{\partial}{\partial x}\left(\rho_g D_k^* \frac{\partial Y_k}{\partial x}\right) = \dot{R}_{g,k} \tag{V.2}$$

2. Darcy equation – Neglecting gravity

$$\boldsymbol{v_g} = -\frac{\boldsymbol{k}}{\boldsymbol{\mu_g}} \frac{\boldsymbol{\partial P}}{\boldsymbol{\partial x}} \tag{V.3}$$

3. Energy equations:

- Gas phase energy balance

$$\begin{gathered} \varepsilon_g \cdot (\rho C_P)_g \frac{\partial T_g}{\partial t} + (\rho C_P)_g \cdot v_g \frac{\partial T_g}{\partial x} = \frac{\partial}{\partial x}\left(\lambda_g^* \frac{\partial T_g}{\partial x}\right) + \\ \Gamma_{s,g} \cdot (T_g - T_s) + Q_g + h(T_{amb} - T_g) \end{gathered} \tag{V.4}$$

- Solid phase energy balance

$$\varepsilon_s \cdot (\rho C_P)_s \frac{\partial T_s}{\partial t} = \frac{\partial}{\partial x}\left(\lambda_s^* \frac{\partial T_s}{\partial x}\right) + \Gamma_{g,s} \cdot (T_s - T_g) + Q_g + h(T_{amb} - T_s) \tag{V.5}$$

4. Perfect gas law (PGL):

$$P_g = \rho_g \frac{R}{\bar{M}_g} T_g \tag{V.6}$$

The pressure equation is obtained by combining eqs. (V.5) and (V.6):

$$\frac{\epsilon_g \bar{M}_g}{RT_g}\frac{\partial P_g}{\partial t} - \frac{\epsilon_g \bar{M}_g P_g}{RT_g^2}\frac{\partial T_g}{\partial t} + \frac{\epsilon_g P_g}{RT_g}\frac{\partial \bar{M}_g}{\partial t} + \frac{\partial}{\partial x}\left(-\rho_g \frac{K}{\mu_g}\frac{\partial P_g}{\partial x}\right) = \dot{R}_g \qquad \text{(V.7)}$$

Thus, the equation PLG can be reformulated as:

$$\rho_g = \frac{P_g \bar{M}_g}{T_g R} \qquad \text{(V.8)}$$

V.1.4 Initial and boundary conditions

Restricting our attention to one dimensional solution, the initial and boundary conditions at the inlet and outlet of the reactor were formulated as follows:

For (eq. 4.2):

- Initial condition:

At t=0 and $\forall x$, $Y_k = Y_k^{amb}$ (V.9)

- Boundary conditions:

If $|Pe_C| < 1$ then,

$Y_k\big|_{x=0} = Y_k\big|_{x=L} = Y_k^{amb}$ (V.10)

If $|Pe_C| > 1$ and $v_g > 0$ then,

$Y_k\big|_{x=0} = Y_k^{amb}$ at x=L, (V.11)

Dankwerts' conditions

If $|Pe_C| > 1$ and $v_g < 0$ then,

at x=0, Dankwerts' conditions (V.12)

and $Y_k\big|_{x=L} = Y_k^{amb}$

with,

$Y_k^{amb} = Y_{N_2}$ in ambient air (V.13)

Y_{O_2} in ambient air

For (eq. 4.3):

- Initial condition:

$$\text{At t=0 and } \forall x,\ v_g = 0 \tag{V.14}$$

- Boundary conditions:

$$\begin{aligned} v_g\big|_{x=0} &= v_e^* \\ v_g\big|_{x=L} &= -\frac{K}{\mu_g}\frac{\partial P_g}{\partial x}\bigg|_{x=L} \end{aligned} \tag{V.15}$$

where, v_e^* is the entry velocity directly linked to entry airflow that is equal v_e .

For (eq. 4.4):

- Initial condition:

$$\begin{aligned} &\text{At t=0 and } \forall x, \\ &T_g = T_g^{amb} \end{aligned} \tag{V.16}$$

- Boundary conditions:

$$\begin{aligned} &\text{If } |Pe_T| < 1 \text{ then,} \\ &T_g\big|_{x=0} = T_g\big|_{x=L} = T_g^{amb} \end{aligned} \tag{V.17}$$

$$\begin{aligned} &\text{If } |Pe_T| > 1 \text{ and } v_g > 0 \text{ then,} \\ &T_g\big|_{x=0} = T_g^{amb} \text{ and} \\ &\text{at x=L, Dankwerts'} \\ &\text{conditions} \end{aligned} \tag{V.18}$$

If $\left|Pe_T\right| > 1$ and $v_g < 0$ then,

at x=0, Dankwerts' conditions and at (V.19)

$$T_g\Big|_{x=L} = T_g^{amb}$$

where, T_g^{amb} is the ambient gas temperature.

For (eq. 4.5):

- Initial condition:

At t=0 and $\forall x$, $T_s = T_s^{amb}$ (V.20)

- Boundary conditions:

Si *t<t_{ig}* then,

$$-\lambda_s^* \frac{\partial T_s}{\partial x}\bigg|_{x=0} = \Phi_{rad} \quad \text{(V.21)}$$

$$\frac{\partial T_s}{\partial x}\bigg|_{x=L} = 0$$

else, (V.22)

$$\frac{\partial T_s}{\partial x}\bigg|_{x=0} = \frac{\partial T_s}{\partial x}\bigg|_{x=L} = 0$$

where, t_{ig} is the duration of the time ignition.

For (eq. 4.7):

- Initial condition:

At t=0 and $\forall x$, $P_g = P^{amb}$ (V.23)

- Boundary conditions:

$$\left.\frac{\varepsilon_g \overline{M}_g}{RT_g}\frac{\partial P_g}{\partial t}\right|_{x=0} - \left.\frac{\varepsilon_g \overline{M}_g P_g}{RT_g{}^2}\frac{\partial T_g}{\partial t}\right|_{x=0} + \left.\frac{\varepsilon_g P_g}{RT_g}\frac{\partial \overline{M}_g}{\partial t}\right|_{x=0} + \left.\frac{\partial}{\partial x}(-\rho_g v_g)\right|_{x=0} = \left.\dot{R}_g\right|_{x=0} \qquad \text{(V.24)}$$

$$\left.P_g\right|_{x=L} = P^{amb}$$

For (eq. 4.6):

- Initial condition:

$$\text{At t=0 and } \forall x\,,\ \rho_g = \rho^{amb} \qquad \text{(V.25)}$$

- Boundary conditions:

$$\left.\rho_g\right|_{x=0} = \frac{\left.P_g\right|_{x=0}\overline{M}_g}{\left.T_g\right|_{x=0}R}$$

$$\left.\rho_g\right|_{x=L} = \frac{\left.P_g\right|_{x=L}\overline{M}_g}{\left.T_g\right|_{x=L}R} \qquad \text{(V.26)}$$

where, ρ^{amb} is the air density at ambient temperature.

The system equation was solved to find the following unknown variables dependent on the time "*t*" and space *"x":* ρ_g, P_g, v_g, Y_k, T_g and T_s.

The physical variables calculated were: ε_g, ε_s, $\dot{R}_g$, D_k^*, $\dot{R}_{g,k}$, k, μ_g, Cp_g, Cp_s, λ_g^*, λ_s^*, $\Gamma_{s,g}$, $\Gamma_{g,s}$, Q_g, Q_s, R and $\overline{M}_g$. Some of these variables are implicitly dependent on unknown variables.

V.1.5 Empirical Data

Several physical variables were determined by empirical laws [hanbook].

Dynamic viscosity of the gas mix:

$$\mu_g = \frac{1.458 \times 10^{-6} \times T_g^{3/2}}{110.4 + T_g} \tag{V.27}$$

Heat capacity of the gases :

$$C_{pg,N_2} = 4.1868 \times 16 \times (6.76 + 0.606 \times 10^{-3} \times T_g + 0.13 \times 10^{-6} \times T_g^2) \tag{V.28}$$

$$C_{pg,O_2} = 4.1868 \times 36 \times (8.27 + 0.258 \times 10^{-3} \times T_g - \frac{1.877 \times 10^5}{T_g^2}) \tag{V.29}$$

$$C_{pg,CO} = 4.1868 \times 28 \times (6.60 + 1.2 \times 10^{-3} \times T_g) \tag{V.30}$$

$$C_{pg,C0_2} = 4.1868 \times 44 \times (7.70 + 5.3 \times 10^{-3} \times T_g - 0.83 \times 10^{-6} \times T_g^2) \tag{V.31}$$

Thermal conductivity of the gases:

$$\lambda_{g,N_2} = \frac{3.33143 \times 10^{-4} \times T_g^{0.7722}}{1 + \frac{16.323}{T_g} + \frac{373.72}{T_g^2}} \tag{V.32}$$

$$\lambda_{g,0_2} = \frac{4.4994 \times 10^{-4} \times T_g^{0.7456}}{1 + \frac{56.699}{T_g}} \tag{V.33}$$

$$\lambda_{g,CO} = \frac{5.9882 \times 10^{-4} \times T_g^{0.6863}}{1 + \frac{57.13}{T_g} + \frac{501.92}{T_g^2}} \tag{V.34}$$

$$\lambda_{g,CO_2} = \frac{3.69 \times T_g^{-0.3838}}{1 + \frac{964}{T_g} + \frac{1.86 \times 10^6}{T_g^2}} \tag{V.35}$$

Heat transfer coefficient:

$$\begin{gathered} \Gamma_{s,g} = A_{factor} \cdot \frac{\lambda_g}{d_p} \cdot \left(2 + 1.1 \cdot \mathrm{Re}^{0,6}\, \mathrm{Pr}^{1/3}\right) = \\ A_{factor} \cdot \lambda_g^* \frac{\lambda_g}{d_p} \cdot \left(2 + 1.1 \cdot \left(\frac{\rho_g v_g d_p}{\mu}\right)^{0,6} \left(\frac{\mu \cdot C_{Pg}}{\lambda_g}\right)^{1/3}\right) \end{gathered} \tag{V.36}$$

The global variables are calculated by the mixing laws:

$$C_{pg} = \sum_k Y_k C_{pg,k} \tag{V.37}$$

$$\lambda_g = \sum_{i=1}^{nbgaz} \frac{X_i \lambda_{g,i}}{\sum_j^{nbgaz} X_i A_{ij}} \tag{V.38}$$

$$A_{ij} = \frac{\left[1 + (\lambda_{g,i}/\lambda_{g,j})^{1/2} (M_{g,i}/M_{g,j})^{1/4}\right]^2}{\left[8\left(1 + M_{g,i}/M_{g,j}\right)\right]^{1/2}} \tag{V.39}$$

Where $A_{i,\ j}$ is a factor taking into account in the calculation of λ_g, *nbgaz* is the number of gaseous species, X_i is the molar fraction for the species *i.* Thus, the expressions of the macroscopic coefficient are:

$$\lambda_g^* = \epsilon_g \lambda_g \tag{V.40}$$

$$\lambda_s^* = \epsilon_s \lambda_s \tag{V.41}$$

V.1.6 Numerical integration

A standard sequential non-iterative operator splitting scheme was used to solve the resulting non-linear problem. Firstly is solved the mass and energy transports term, thanks to a transport operator which uses a full sequential approach and finite volume schemes – Appendix C (Lapene 2006). Finally, the chemistry operator, which is reduced to a stiff ODE system, is solved by the LSODES FORTRAN library, which uses backward differentiation formulas by Gear.

V.2 Determination of the model parameters

V.2.1 Parameters determined experimentally

In this section we briefly recall the main parameters determined before and used in the numerical code.

Physical properties:

1. apparent density of the packed bed, 1168 *kg* m^{-3};
2. bed porosity, 0.472 %;
3. real density adopted 2214 *kg* m^{-3};

Chemical properties:

4. reaction heat of decarbonation reaction - 589 kJ kg^{-1} of oil shale
5. kinetics:

   A_{decarb}=2.68x10^4 m^{-1}, E_{decarb}=135.1x10^3 kJ mol^{-1};

   A_{oxy}=0.055x10^4 m^{-1}, E_{oxy}=52.4x10^3 kJ mol^{-1};

6. oil shale composition: CF= 4.7 %; VM= 17.2 %; $CaCO_3$= 34.6 %; IM= 43.5 %;
7. reaction heat of char oxidation + 19470 kJ kg^{-1} corresponding with *fr*= 0.565.

Heat transfer properties:

8. Oil shale conductivity: $\lambda_s = 0.89$ W $m^{-1}K^{-1}$;
9. Heat transfer coefficient $\Gamma_{s,g} = 0.544$ kW m^{-2}K.

V.2.2 Parameters fitting

A number of parameters in the model were adjusted through a procedure of fitting the model to the experimental results. This was carried on when it was considered that the value determined directly was uncertain, and that their adjustments lead to better model results.

In the case of kinetics parameters, the activation energy value is saved and the pre-exponential is adjusted:

a. *Decarbonation rate parameter, A_{decarb}:*

As seen previously (IV.2.1.A), after the passage of the combustion front, it can be calculated that the front has decarbonated 83 % of the initially present carbonates inside the whole cell.

Thus the pre-exponential factor was adjusted to leave around 20 % of the carbonate in the bed. Figure (V.1) shows the result of the model which a value A_{decarb}= 0.25*2.68x10^4 min^{-1}, while the value determined from TG experiment was 2.68x10^4 min^{-1}. The original value was multiplied by a factor of 0.25 to retrieve to decarbonation rate in the reactor.

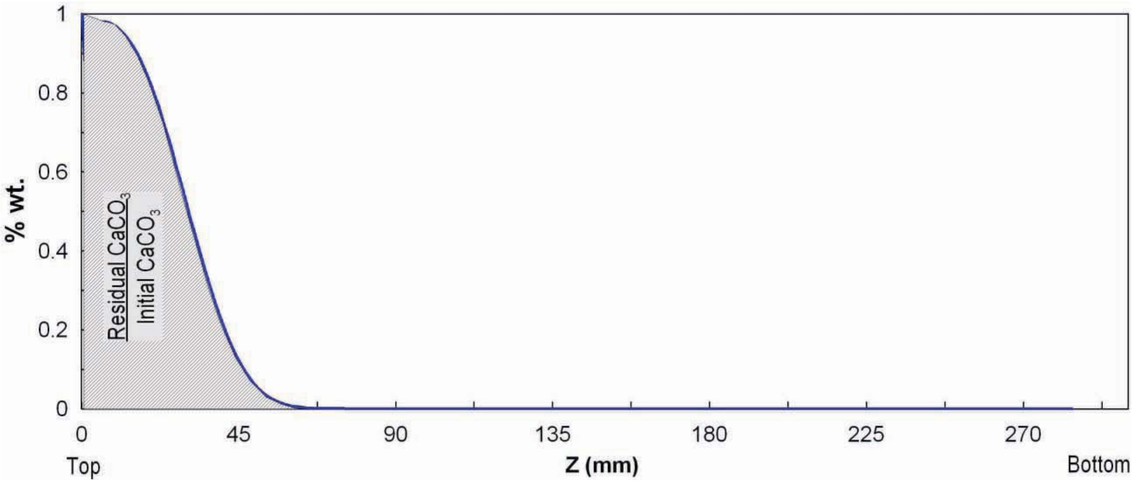

Figure (V.1) – $CaCO_3$ profile in the bed

b. *Char oxidation rate parameter, A_{oxy}:*

The pre-exponential factor of the char oxidation was adjusted by fitting the model temperature peak to the experimental value. The value of 550 min^{-1} determined from TG experiment was turned to 30.555 min^{-1} in the model, Figure (V.2).

In the case of thermal properties, the coefficients were adjusted by fitting the model predicted temperature field at a given time (t= 3492 s) with the experimental temperature profile. These were the parameters adjusted:

c. *Heat transfer coefficient between gas and solid.*

In chapter III (III.5.2) the heat transfer coefficient was evaluated from specific experiment and fitting a numerical model. A_{factor} value was adjusted to 55 in the model.

d. *Heat loss through the walls coefficient:*

In the energy equation there is a coefficient, Q_w, which takes into account the heat loss through the walls. Figure (V.2) shows the temperature obtained from the model under adiabatic combustion – i.e. excluding heat loss through the walls. This temperature plateau is characteristic of the *reaction leading* combustion front structure as discussed in chapter (I.6.2).

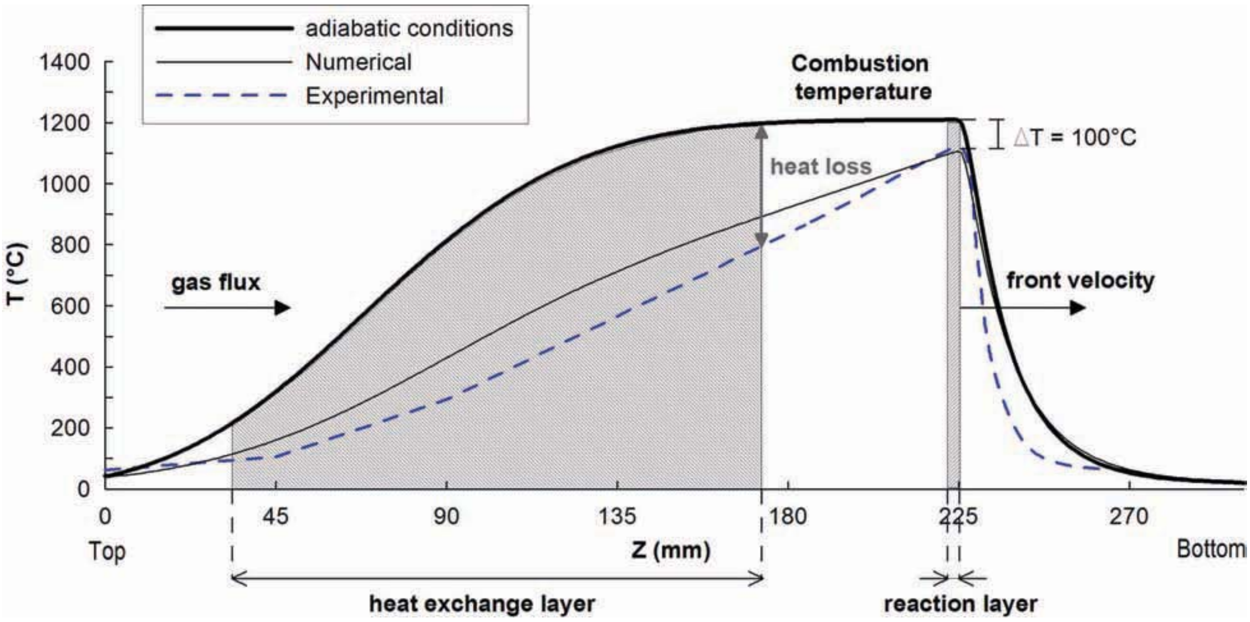

Figure (V.2) - Forward combustion front: reaction leading structure

The experimental temperature field also reported in figure is very different from the adiabatic model prediction; this is due to heat losses. By adjusting the value of *h* to 195 the model predicted temperature field fits the experimental temperature field satisfactorily. It can be calculated that with this value of *h*, the global heat loss for the overall combustion process is about 40 % of the energy released by fixed carbon oxidation. This percentage is in good agreement with the value of 50 % calculated through a heat balance of the experiment, as detailed in Appendix D.

Based on the equations presented in chapter I (I.6.2) and the char oxidation stoichiometry presented in chapter IV (cf. IV.2.1.D) it was calculated the Δ (the ratio of the specific heats of the gas and solid, and to the ratio of the initial concentrations of the solid fuel and the gaseous oxidizer), the adiabatic temperature and combustion temperature.

- The Δ was about 0.39. This confirms that the reaction leading structure (Aldushin, Rumanov and Matkowsky 1999).

- In the reaction leading structure, (Pinjala, Chen and Luss 1988) observed a pronounced superadiabatic effect in his experimental work. The adiabatic combustion temperature was calculated in the case of the mix 75/25 wt. oil shale/sand; see Appendix E. It was taken into account that carbon oxidizes into CO and CO_2 and that decarbonation occurs. The value obtained was 265

°C. The temperature level observed during experiments was about 1100 °C: the combustion is largely superadiabatic.

- Also in Figure (V.2), can be observed that the combustion temperature plateau computed under adiabatic conditions was 1200 °C, which is in very good agreement with 1190 °C calculated using the analytical method ($T_{plateau}$). The difference between experimental temperature level and the adiabatic temperature was 100 °C: heat losses are responsible for this peak temperature decrease, which is not so high regarding the value of 50 % losses.

V.3 Results from the numerical model

Once these parameters were fitted, the modeling was run and the results interpreted into detailed to gain information about the front structure. Table (V.1) presents the input data used.

Numerical parameters	**Description**	**Unit**
300	Number of nodes	-
$dt = 5x10^{-3}$	Time step	-
$dx = 1x10^{-3}$	Space step	*m*
$t_{exp} = 5200$	Time of experiment	*s*
Physical parameters		
$t_{ig} = 378$	Ignition time duration	*s*
0.30	Reactor length	*m*
$P_{atm}=1.013x10^5$	Atmospheric pressure	*Pa*
$T_{amb}=293.15$	Ambient temperature	*K*
$V_{in} = 0.0243$	Entry velocity	$m\ s^{-1}$
$S_{spec} =2321.26$	Specific surface	m^{-1}
$\varepsilon = 0.47$	Bed porosity	-
$d_p = 750$	Average particle diameter	*µm*
$\rho_s = 2214$	Solid density	$Kg\ m^{-3}$
Heat transfer properties		
$\lambda_s = 0.89$	Solid conductivity	$W\ m^{-1}K^{-1}$
$Cp_s = 0.585 \times T + 664.5$	Heat capacity of solid	$J\ kg^{-1}K^{-1}$

$\Gamma_{s,g} = 55 \cdot \frac{\lambda_g (2 + 1.1\mathrm{Re}^{0.6}\,\mathrm{Pr}^{1/3})}{\mathrm{d_p}}$	Heat transfer coefficient between solid and gas	$W\,m^{-2}K^{-1}$
Chemical parameters		
$Y_{CaCO_3} = 34.6$	Calcite mass fraction	Kg/kg
$Y_{FC} = 4.15$	Fixed carbon mass fraction	Kg/kg
$Y_{IM} = 43.5$	Inert matter mass fraction	Kg/kg
$fr = 0.565$	Ratio of the products of combustion: CO/CO_2	-
$+19470$	Reaction heat for char oxidation	$kJ\,kg^{-1}$
-589	Reaction heat for decarbonation process	$kJ\,kg^{-1}$
$C + [\frac{fr}{2} + (1-fr)]O_2 \rightarrow fr\,CO + (1-fr)CO_2$	Fixed carbon oxidation reaction	-
$CaCO_{3(s)} \rightarrow 0.56CaO_{(s)} + 0.44CO_{2(g)}$	Decarbonation reaction	-

Table (V.1) - Values of parameters used in the model for oil shale combustion.

V.3.1 Temperature of the bed

Concerning the temporal evolution of temperature, the Figure (V.3) shows the temperature for two thermocouples T1 and T2. A difference between the temperature peaks (numerical and experimental) is about 100 °C and a delay between the peak times were observed. This indicates that the description used for ignition process does not represent the real physical problem. However, the model was sufficient to start the reactions. After ignition at the surface, a combustion front starts to propagate through the bed. For the other thermocouples (T3, T10, T11 and T12), peaks at a temperature near 1100 °C were observed with no significant time delay. The combustion process was in an established regime. The temperature plateau at 60 °C observed during the experiments, Figure (IV.7-a), is not described by the model since there is no reaction included to take it into account; the implementation of a reaction into the model remains a possible improvement.

Figure (V.4) shows axial temperature profiles along the reactor axis at different times. As observed in the experimental result, the temperature decreases downstream the front, while the hot zone upstream the front becomes getting larger as the front progresses. This confirms that the reaction zone propagates more rapidly than the heat exchange zone, as discussed previously. The temperature level is almost the same once combustion process is well established, between Z= 90 mm until 300 mm.

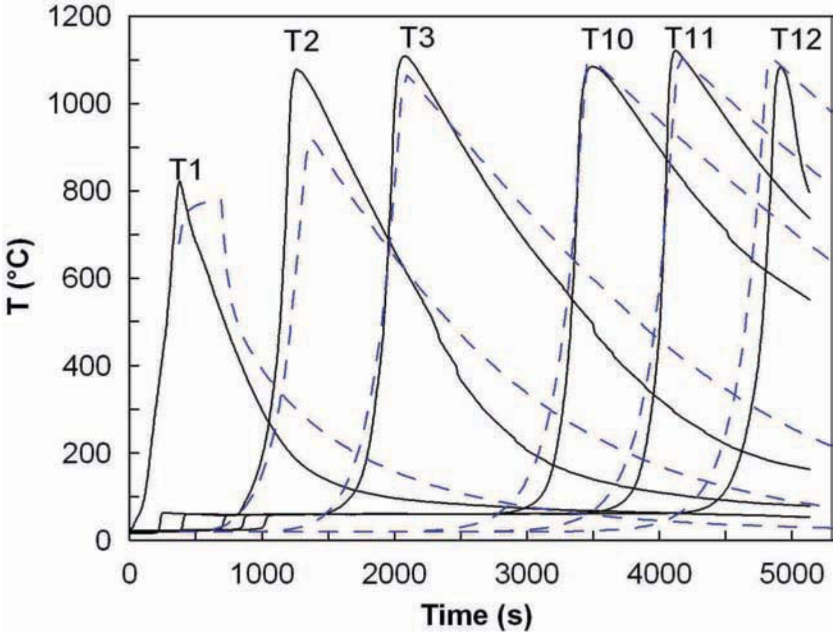

Figure (V.3) – Temperature evolution: (—) experimental, (– – –) numerical.

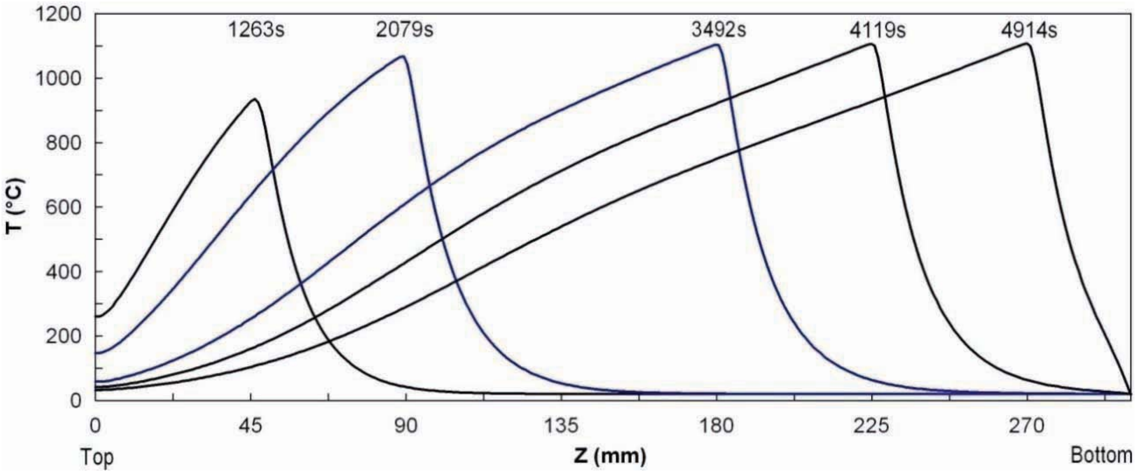

Figure (V.4) -Temperature profile in the bed.

V.3.2 Combustion front velocity

The numerical and experimental front velocities are shown in Figure (V.5). The model predicts a constant front velocity while experiments indicated an increasing value.

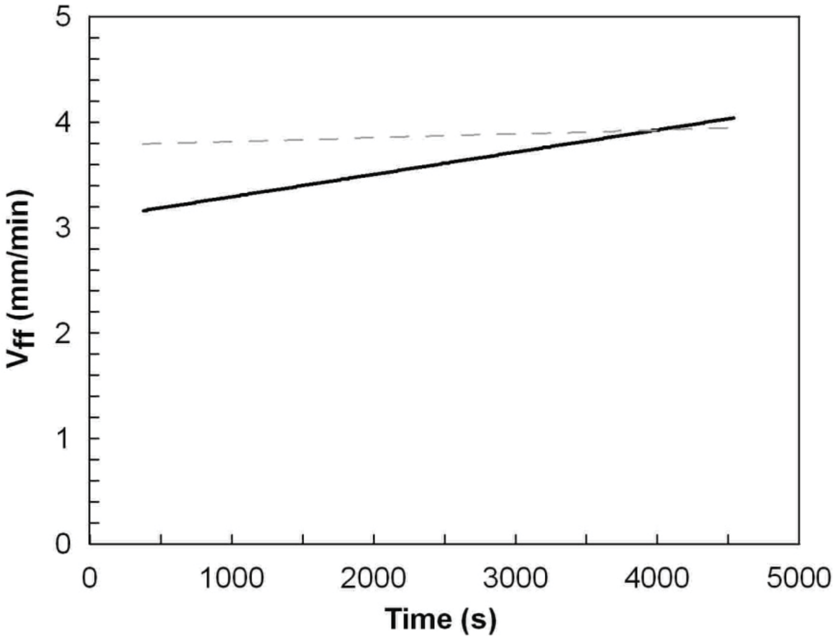

Figure (V.5) -Front velocity: (—) experimental, (– – –) numerical.

V.3.3 Combustion front structure

A detailed geometrical description of the front structure can be established, from the results of the model at a given time – 4119 s for instance. In Figure (V.6), it was plotted three types of results in relation to TPP:

- Temperature profile in the bed;
- Fixed carbon and $CaCO_3$ normalized density profile;
- Molar fraction of CO and CO_2.

It must be remembered that the numerical model does not describe drying and devolatilization reactions.

The fixed carbon combustion zone is identified as the zone where the density of fixed carbon changes. It was found between Z = -1 mm and Z = 11 mm; the thickness was about 12 mm. This is in good agreement with the experimental result (cf. IV.2.2.B) where was established that the oxidation is made in the zone 10 mm downstream the TPP.

The decarbonation zone - corresponding with changes in $CaCO_3$ - is located essentially along 4 mm upstream of the TPP, and also downstream, along 7 mm. The thickness was about 11 mm. This result shows that the decarbonation model used is in agreement with the experimental results that established a thickness about of 15 mm.

At the bottom of the figure, the model predicted CO and CO_2 molar fractions were plotted together with the experimental results from micro-sampling system. The shift between the curves at high Z is due to the fact that in the model, volatile matters are not taken into account and should not be considered. This figure shows a very satisfactory agreement.

As a synthesis of the results from the model, it can be concluded that:

- With a ratio of the specific heats of the gas and solid equal to 0.39, the reaction leading structure was established;
- The reaction zone propagates more rapidly than the heat exchange zone;
- The heat losses represents about 50 % of the fixed carbon oxidation; these losses have a little impact on the front peak temperature;
- A two temperature model was used; however the difference between the two phases (solid and fluid) temperature was less than 3 °C, indicating a thermal local equilibrium;
- The thickness of the fixed carbon oxidation was about 10 mm;
- The thickness of the decarbonation zone was about 11 mm

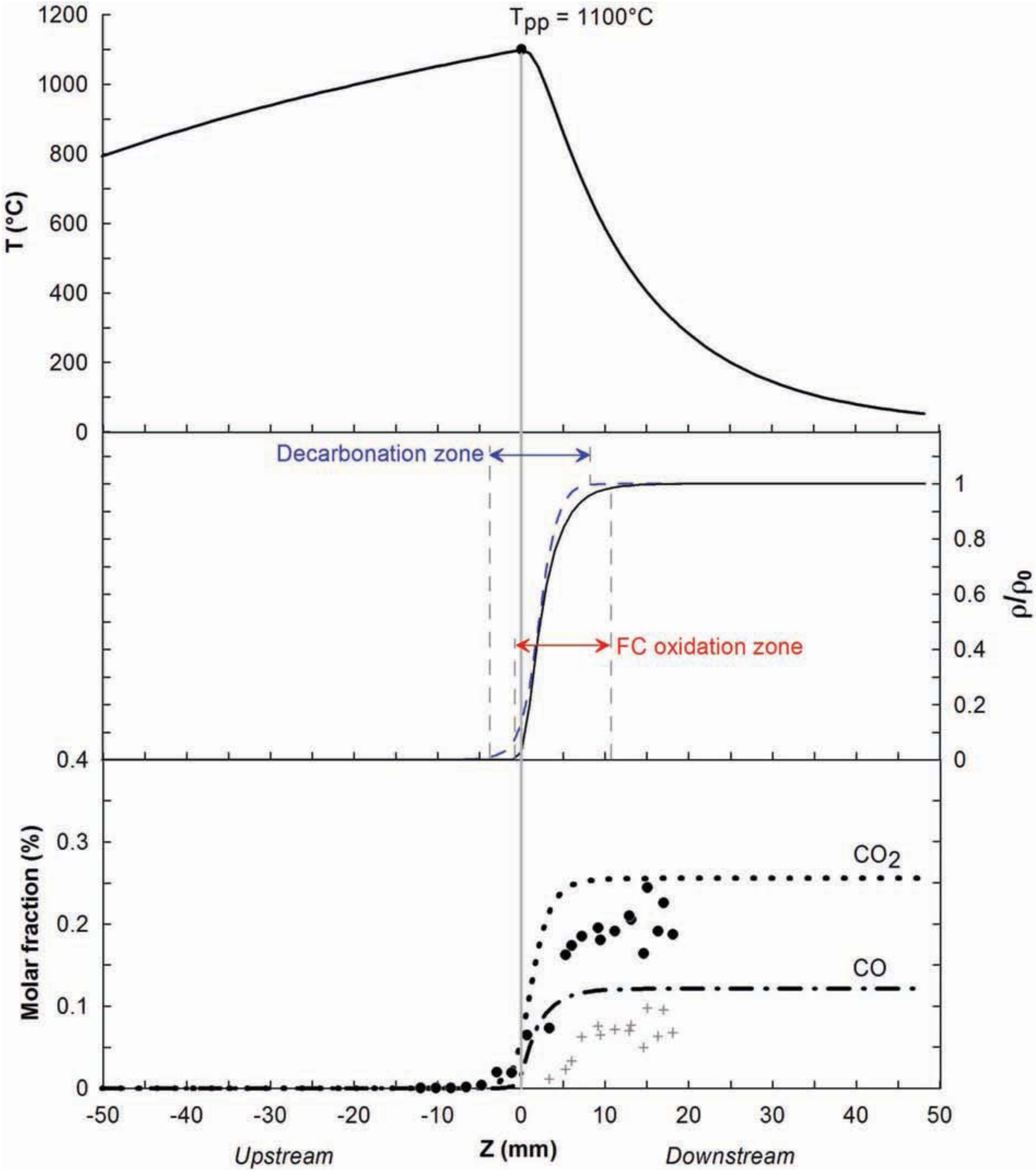

Figure (V.6) – Model computed: (—) normalized Fixed carbon density profile, (– – –) $CaCO_3$ density profile, (…) CO_2 molar fraction, (– · –) CO molar fraction. Experimental measures: (•) CO_2 and (+) CO molar fraction.

V.4 Parametric study

This topic was dedicated to the observation of the behavior of the numerical model when a parameter is changed. The experimental and numerical confrontation was made allowing the identification of strength and weakness of the model.

The following parameters were used to investigate the influence on combustion process:

- Air velocity varied in the range 0.024 to 0.062 m s^{-1};
- Particle diameter varied in the range 407 to 1500 µm;

The reference experiment was made with an air velocity of 0.042 m s^{-1}, a particle size of 750 µm and a 75 % of oil shale in the bed. It was taken a higher velocity to having a lower experiment time.

V.4.1 Influence of airflow

Figure (V.8) illustrates the influence of air velocity. Numerical and experimental results have the same trend. The model indicates that increasing the air velocity from 0.024 to 0.062 m s^{-1} results in an increase of 130 °C in the temperature peak.
The experiments indicated a smaller increase. Concerning the combustion front velocity, it was observed that both numerical and experimental results are proportional to the airflow of injection. This was the expected result since the front propagation is controlled by air supply.

A particular case must be mentioned. The experiments with air velocity at 0.062 m s^{-1} were run several times. However, the front struggled propagating only once. Figure (V.7) shows the temperatures recording obtained during this experiment. It shows a non stable propagation. It is possible that 0.062 m s^{-1} is the upper limit for air velocity for a stable propagation of a combustion front.

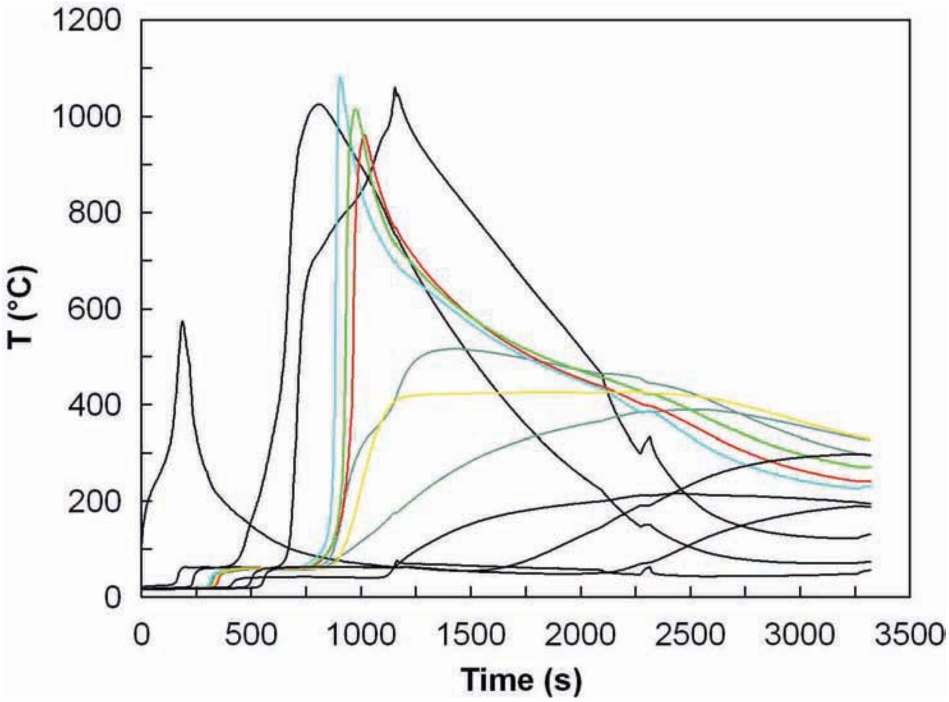

Figure (V.7) -Temperature evolution for air velocity at 0.062 m s-1.

V.4.2 Influence of particle diameter (d_p)

Figure (V.9) shows that increasing the average particle diameters from 407 to 1500 µm, the temperature peak in the reactor is quite constant. Both experiments and the model lead to this result. The same trend was observed for combustion front velocity.

(Sensöz, Angın and Yorgun 2000) performed the experiments at a high heating rate at 40 K min^{-1} in the “Heinze retort”; his results indicated that there was no significant effect of the particle size in the range 224 to 850 µm on the conversion and oil yield.

In the numerical model the particle diameter is taken into account only in the calculation of heat transfer coefficient between phase solid and fluid. This coefficient can be calculated at 29.8, 29.9 and 30.1 kW m^2 K^{-1} for particle diameters of 400, 750 and 1500 µm respectively. For the three average particles diameter, this parameter has indeed a negligible influence on $\Gamma_{s,g}$ value.

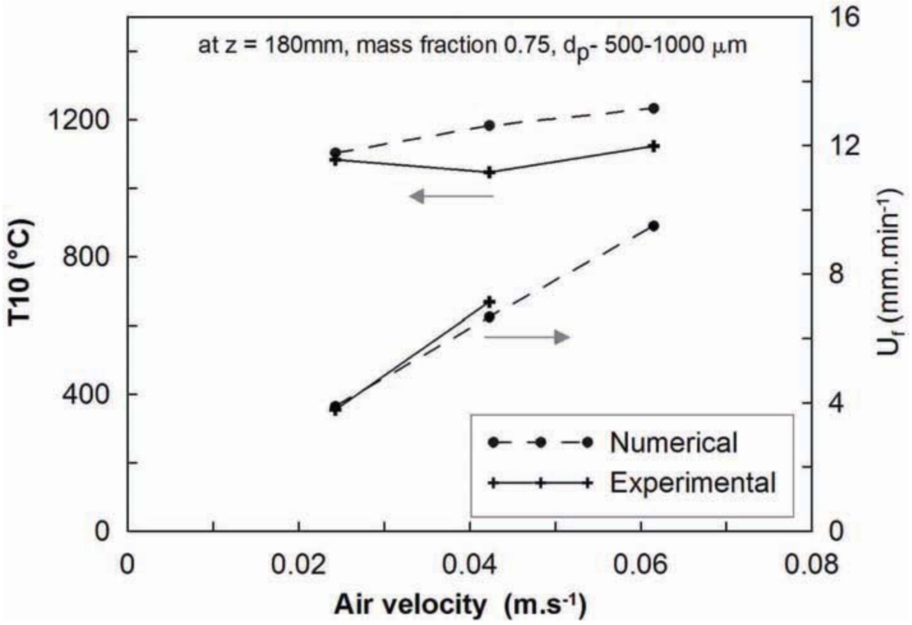

Figure (V.8) - Air velocity versus temperature and front velocity.

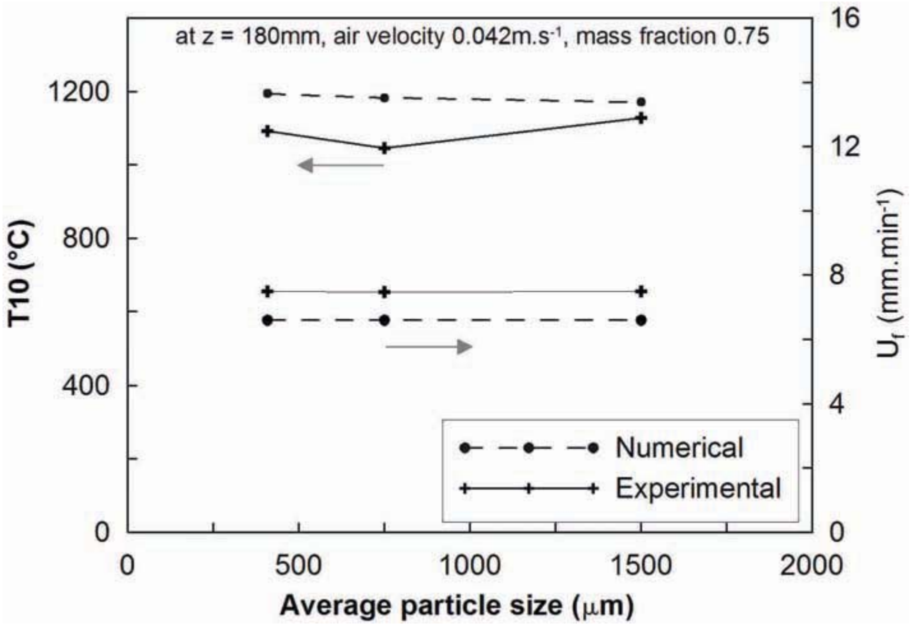

Figure (V.9) - Average particle diameter versus temperature and front velocity.

In summary, the numerical tool reproduces in general correctly trends of experimental results for the oil shale combustion. First of all, it was in put into the model some physical, chemical and thermal properties determined in this work. The model shows a good answer in relation to the real physical problem, however, it was necessary adjust the pre-exponential factors for both reactions taken into account in the model. The simulation of the case described in chapter IV showed a good agreement with the experimental results, particularly the confirmation of the propagation structure: reaction leading structure. It was also possible to confirm the thickness of the decarbonation and fixed carbon oxidation zone.

Finally, about the parametric study, some points must be highlighted:

- the front propagation is controlled by air supply;
- the air velocity of 0.062 m s^{-1} as a possible upper limit of propagation;
- the particle size variation there is no significant effect in the combustion propagation.

Conclusions and perspectives

In the last part of the thesis, the main developments and results are summarized. Possible directions for further research are given.

The aims of this work were formulated in order to obtain a better understanding of the dynamic behavior of co-current combustion front propagation in reactive porous medium.

Regarding the chemical characterization of oil shale, a detailed proximate analysis established with a horizontal tube furnace made it possible to determine a global composition of oil shale: volatile matter 17.2 %, fixed carbon 4.7 %, carbonate 34.6 % and inert matter 43.5 %. Still concerning this experiment, two points must be highlighted: firstly the fixed carbon amount was not affected by the heating rate; secondly, at a high temperature and under nitrogen atmosphere, the fixed carbon disappears progressively, which remains an unexplained phenomenon. Analyzing the devolatilization gases, it was determined that, the organic matter is converted: ¼ into fixed carbon, ¼ into pyrolysis gas (which the composition was detailed) and ½ into shale oil.

From detailed analysis of the oil shale, of the solid residue after passage of the front and of the flue gas, it was established that:

- The front devolatilizes integrally the oil shale;
- The front oxidizes 88.2 % of the fixed carbon that is formed during devolatilization;
- The front decarbonates 83.2 % of the calcite.

A new and original experimental device was designed, developed and operated with success.

Calibration tests with the “simple” medium charcoal/sand showed a plane and horizontal combustion front. A mass balance of the species O_2 (from air) and CO and CO_2 produced by oxidation of charcoal was closed satisfactorily. The combustion of oil shale showed a much more complicated situation.

- The combustion front had a curved and inclined surface. The front progresses faster close to the walls than the reactor axis; explanations in terms of O_2 supply and gas viscosity were proposed;

- The mass balance of the carbon species was closed satisfactorily, but the balance of oxygen was not correct. For these experiments, the oil shale had to be mixed with sand to lower the peak temperature. The air feeding velocity was 0.0243 m s^{-1} at STP.

Concerning the question of what is oxidized in the front, it seems that the non condensable volatile matter - as characterized in previous tests – are almost integrally retrieved at the exit of the cell. Therefore, it appears that only fixed carbon oxidation occurs. Nevertheless, two observations make this conclusion uncertain: the O_2 mass balance was not closed, and the oxidation of a fraction of oil shale, observed during DSC experiments (before the oxidation of fixed carbon), was not taken into account in the mass balance. Moreover, 56.5 % of the fixed carbon is finally retrieved as CO, while the rest is converted into CO_2. Considering the CO_2 formed, it was established that the CO_2 from decarbonation of carbonates represents 69 % of the total CO_2 emissions, including CO_2 from fixed carbon oxidation.

From the temperature fields established by measurements, only rough estimates of the thickness of the different zones in the front could be established. However, using the micro-sampling system, precisions were gained on these aspects:

- it can be established that the oxidation is essentially concentrated in the zone from the temperature peak point (TPP) toward 10 mm downstream of the TPP;
- the decarbonation zone spreads from 5mm upstream of the TPP to 10 mm downstream.

It was shown that accumulation of oil occurs on the bottom of the bed during the propagation process. Later on, as the front progresses, this oil is driven out from the cell by the end of the experiment. For that raison is thought that liquid oil is never formed inside the medium and pushed by the front during the propagation process. This observation may be due to the short length of the cell used in this work.

Concerning the energy balance, the fixed carbon oxidation into CO and CO_2 consumes 10 % of the energy contained by the oil shale, while the fixed carbon left in the oil shale residue represents only 2.3 %. The flue gas energy represents 17 % of the oil shale energy. Despite the quite large diameter and the good thermal insulation, heat losses through the walls remain high, about 40 % as determined from a global heat balance of the cell.

Developing the numerical model and interpreting the results made possible numerous achievements. A mathematical formulation with 1D geometry and two phases - the solid phase and the gas phase - was adopted. Previous observations indeed indicated that liquid oil is probably never formed inside the medium.

The determination of most of the properties required by the model was achieved from specific experiments including:

- Structural properties: density, porosity;
- Thermal properties: thermal conductivity and heat transfer coefficient;
- Reactions heat and kinetic parameters of reactions;
- Oil shale composition: fixed carbon, volatile matter, carbonates and inert matter amounts.

Nevertheless, it was necessary to adjust some of the properties for the model to fit the experimentally determined temperature fields and decarbonation profile in bed. This was the case for the pre-exponential factor of fixed carbon oxidation and decarbonation reactions, heat exchange coefficient $\Gamma_{s,g}$, and the heat loss coefficient.

The temperature field corresponds to the *reaction leading structure.* In this situation, the reaction zone propagates more rapidly than the heat exchange zone.

The model retrieved that 50 % of the heat released by fixed carbon oxidation was lost through the walls. A calculation without heat losses indicated that the temperature peak would be until 1200 °C instead of 1100 °C without heat losses.

In the modeled configuration, the thermal equilibrium occurred, making a two temperature approach unnecessary.

Concerning the chemical structure of the front, it was finally stated that:

- the fixed carbon oxidation zone has about 12mm of thickness. This is quite similar to the experimental results from micro-sampling system.

- the decarbonation zone is located essentially along 4mm upstream of the TPP, and also downstream, along 7 mm, demonstrating a good agreement with the experimental results from micro-sampling system.

The parametric study finally indicated that the model predicts satisfactorily the response of the front when changed the air velocity. This study confirmed that the front propagation was controlled by O_2 supply, as established from the previous mass balance. It was demonstrated that the variation in the particle size between 400 and 1500 μm does not affect the front propagation.

In this PhD thesis the structure of the combustion front propagating in a reactive porous medium was proposed using a fine experimental device and a numerical tool. New implications for future works are opened. The main perspectives of this study are:

With micro-sampling system:

- To quantify the oxygen contained in the micro-samples of the flue gas. This will allow a more accuracy in the evaluation of the fixed carbon oxidation zone;

- To quantify the hydrocarbons contained in the micro-samples of the flue gas. This will allow the evaluation of the devolatilization zone.

With the combustion cell:

- To carry out the combustion of crushed oil shale without sand;

- To carry out the combustion of pyrolyzed oil shale. Thus, it will be easier the improvement of the mass balance of oxygen;

- To determine the limit values – higher and lower for the main parameters that affect the front propagation: air velocity, mass fraction of oil shale in the bed and oxygen molar fraction.

With the numerical model:

- The improvement of oil shale combustion mechanisms, including the reaction responsible for originating a temperature plateau at 60°C observed during the experiments.

References

Akkutlu, I. Y., and Y. C. Yortsos. "The dynamics of in-situ combustion fronts in porous media." *Combustion and Flame* 134, no. 3 (2003): 229-247.

Aldushin, A. P. "Heat transfer and convection combustion regimes of porous systems with filtration of heat carrier." *Combustion, Explosion, and Shock Waves* 26, no. 2 (mars 1990): 180-187.

Aldushin, A. P. "New results in the theory of filtration combustion." *Combustion and Flame* 94, no. 3 (August 1993): 308-320.

Aldushin, A. P. "New results in the theory of filtration combustion." *Combustion and Flame* 94, no. 3 (August 1993): 308-320.

Aldushin, A. P., I. E. Rumanov, and B. J. Matkowsky. "Maximal energy accumulation in a superadiabatic filtration combustion wave." *Combustion and Flame* 118, no. 1-2 (July 1999): 76-90.

Altun, N. E., C. Hiçyılmaz, J.-Y. Hwang, A. S. Bağcı, and M. V. Kök. "Oil Shales in the world and Turkey; reserves, current situation and future prospects: a review." Edited by Estonian Academy Publishers. *Oil Shale* 23, no. 3 (2006): 211–227.

Babkin, V. S., V. I. Drobyshevich, Y. M. Laevskii, and S. I. Potytnakov. "Filtration combustion of gases ." *Combustion, Explosion, and Shock Wave* 19, no. 2 (mars 1983): 147-155.

Bar-Ilan, A., G. Rein, A. C. Fernandez-Pello, J. L. Torero, and D. L. Urban. "Forced forward smoldering experiments in microgravity." *Experimental Thermal and Fluid Science* 28, no. 7 (September 2004): 743-751.

Bar-Ilan, A., O.M. Putzeys, G. Rein, A.C. Fernandez-Pello, and D.L. Urban. "Transition from forward smoldering to flaming in small polyurethane foam samples." *Proceedings of the Combustion Institute* 30, no. 2 (January 2005): 2295-2302.

Barkia, H., L. Belkbir, and S. A. A. Jayaweera. "Kinetic studies of oxidation of residual carbon from moroccan oil shale kerogens." *Journal of Thermal Analysis and Calorimetry* 86, no. 1 (septembre 2006): 121-123.

Barkia, H., L. Belkbir, and S. A. A. Jayaweera. "Thermal analysis studies of oil shale residual carbon." *Journal of Thermal Analysis and Calorimetry* 76, no. 2 (mai 2004): 615–622.

Batsale, J., C. Gobbe, and M. Quintard. "Local non-equilibrium heat transfer in porous media." *Recent Research Development in Heat, Mass and Momentum Transfer 1.* India: Research Signpost, 1996. 1–24.

Bekri, O. «Caractéristiques et propriétés physico-chimiques des schistes bitumineux de Timahdit et Tarfaya.» *Thése de Doctorat.* Université Mohamed V, 27 Février 1996.

Biyikoglu, A., and M. Sivrioglu. "Simulation of Combustion in a Coal-Fired Boiler with a Fixed Bed." *Energy Sources* 26, no. 8 (July 2004): 795-809.

Bousaid, I. S. Recovery of heavy crude oil from shallow formations by in situ combustion. N.Y. USA Patent 4.638.864. January 27, 1987.

Bruan, V., M. Halim, M. Ziyad, C. Largeau, and A. Amblès. "Characterization of the Moroccan Timahdit (X-layer) oil shale kerogen using pyrolysis and thermally assisted hydrolysis and methylation." *Journal of Analytical and Applied Pyrolysis* 61, no. 1-2 (November 2001): 165-179.

CanREN. "Natural Resources Canada." Vers. Bioenergy Series - 1. Edited by ©Her Majesty the Queen in Right of Canada. Bruce McCallum, Ensight Consulting, P.E.I. 2001. http://www.canren.gc.ca/prod_serv/index.asp?CaId=129&PgId=727.

Castanier, L. M., and W. E. Brigham. "Upgrading of crude oil via in situ combustion." *Journal of Petroleum Science and Engineering* 39, no. 1-2 (August 2003): 125-136.

Chanaa, M. B., M. Lallemant, and A. Mokhlisse. "Pyrolysis of Timahdit, Morocco, oil shales under microwave field." *Fuel* 73, no. 10 (October 1994): 1643-1649.

Cinar, M., L. M. Castanier, and A. R. Kovscek. "Improved Analysis of the Kinetics of Crude-Oil In-Situ Combustion." *SPE 113948, Proceedings of the SPE Western Regional Meeting.* Bakersfield, CA., 2008.

Countryman, and McDaniel. "Cargolaw." 2004. http://www.cargolaw.com/2004nightmare_coal-face.html.

Debenest, G. «Simulation numérique 3D, à la microéchelle, de la combustion en lit fixe de schistes bitumineux.» *Thèse de doctorat de l'Université de Poitiers.* 17 Octobre 2003.

Debenest, G., V.V. Mourzenko, and J.-F. Thovert. "Smoldering in fixed beds of oil shale." *Combust. Theory Modelling* 9 (February 2005a): 113-135.

Debenest, G., V.V. Mourzenko, and J.-F. Thovert. "Smouldering in fixed beds of oil shale grains: governing parameters and global regimes." *Combustion Theory and Modelling* 9 , no. 2 (2005b): 301–321.

Dollimore, D., P. Tong, and K.S. Alexander. "The kinetic interpretation of the decomposition of calcium carbonate by use of relationships other than the Arrhenius equation." *Thermochimica Acta* 282-283 (1996): 13-27.

Dyni, J. R. *Geology and Resources of Some World Oil-Shale Deposits.* USGS Scientific Investigations Report, http://pubs.usgs.gov/sir/2005/5294/, 2005.

Fatehi, M., and M. Kaviany. "Adiabatic reverse combustion in a packed bed." *Combustion and Flame* 1, no. 99 (1994): 1-17.

Gersten, J., V. Fainberg, G. Hetsroni, and Y. Shindler. "Kinetic study of the thermal decomposition of polypropylene, oil shale, and their mixture." *Fuel* 79, no. 13 (October 2000): 1679-1686.

Ghabi, C., G. Rein, H. B. Ticha, and M. Sassi. "Bidimensional Numerical Model for Polyurethane Smoldering." *Progress in Computational Heat and Mass Transfers 1.* Paris: Proceedings of the 4 ICCHMT, 2005. 572-578.

Gort, R., M. Valk, and G. Brem. "Solid fuel combustion in a laboratory grate furnace." *Proc. 3rd AsianPacific Symposium on Combustion and energy utilization.* Hongkong, 1995.

Hallett, W. L. H. "Packed bed combustion: An overview." *Combustion Institute Canadian Section Spring Meeting.* 2005.

Hamilton, J. "Econbrowser." September 27, 2005. http://www.econbrowser.com.

Hansom, J., and M.-K. Lee. "Effects of hydrocarbon generation, basal heat flow and sediment compaction on overpressure development: a numerical study." *Petroleum Geoscience* 11, no. 4 (2005): 353-360.

Hobbs, M. L., P. T. Radulovic, and L. D. Smoot. "Combustion and gasification of coals in fixed-beds." *Progress in Energy and Combustion Science* 19, no. 6 (1993): 505-586.

Howell, J. R., M. J. Hall, and J. L. Ellzey. "Combustion of hydrocarbon fuels within porous inert media." *Progress in Energy and Combustion Science* 22, no. 2 (1996): 121-145.

Jaber, J. O., and S. D. Probert. "Pyrolysis and gasification kinetics of Jordanian oil-shales." *Applied Energy* 63, no. 4 (August 1999): 269-286.

Johnson, H. R., P. M. Crawford, and J. W. Bunger. *Strategic Significance of America's Oil Shale Resource.* U.S. Department of Energy , Washington, DC: AOC Petroleum Support Services, LLC and Washington, D.C., 2004.

Kaviany, M. *Principles of Heat Transfer in Porous Media.* Edited by Springer. Vol. 1. New York: Mechanical Engineering Series , 1995.

Khor, A., C. Ryu, Y. B. Yang, V. N. Sharifi, and J. Swithenbank. "Straw combustion in a fixed bed combustor." *Fuel* 86, no. 1-2 (January 2007): 152-160.

Kiehne, T. M., D. E. Wilson, and R. D. Matthews. "Numerical solution technique for transient, two-dimensional combustion with multi-step kinetics." *Computer Methods in Applied Mechanics and Engineering* 83, no. 1 (October 1990): 9-31.

Kissinger, H.E. "Reaction kinetics in differential thermal analysis." *Analytical Chemistry, 29 (11), pp. 1702-1706.* 29, no. 11 (1957): 1702-1706.

Kok, M. V. "Thermal investigation of Seyitomer oil shale ." *Thermochimica Acta* 369, no. 1-2 (March 2001): 149-155 .

Kök, M. V., and M. R. Pamir. "Comparative pyrolysis and combustion kinetics of oil shales." *Journal of Analytical and Applied Pyrolysis* 55, no. 2 (July 2000): 185-194.

Kök, M. V., and M. R. Pamir. "Pyrolysis and combustion studies of fossil fuels by thermal analysis methods." *Journal of Analytical and Applied Pyrolysis* 35, no. 2 (December 1995): 145-156.

Kok, M. V., and R. Pamir. "ASTM kinetics of oil shales." *J. Therm. Anal. Cal.* 53, no. 2 (1998): 567–575.

Kök, M. V., G. Guner, and S. Bagci. "Combustion kinetics of oil shales by reaction cell experiments." *Oil Shale* 25, no. 1 (2008): 5–16.

Kok, M. V., J. Sztatisz, and G. Pokol. "Characterization of oil shales by high pressure DSC." *J. Therm. Anal. Cal* 56, no. 2 (1999): 939–946.

Kowhakul, W., M. Kumasaki, M. Arai, and M. Tamura. "Calorimetric behaviors of N2H4 by DSC and superCRC." *Journal of Loss Prevention in the Process Industries* 19, no. 5 (September 2006): 452-458.

Lapene, A. *Modélisation numérique de la combustion en lit fixe de combustibles solides.* Rapport de stage, IMFT, Toulouse: Master Recherche en Dynamique des Fluides, Energétique et Transferts, 2006.

Lapene, A., G. Debenest, M. Quintard, M. F. Martins, and S. Salvador. "Numerical Simulation of Combustion in Reactive Porous Media." *International Review of Mechanical Engineering (I.RE.M.E.)* xx, no. x (2008): xxx-xxx.

Lapene, A., M. F. Martins, G. Debenest, M. Quintard, and S. Salvador. "Numerical simulation of oil shale combustion in a fixed bed: modelling and chemical." *Eurotherm Seminar N° 81 Reactive Heat Transfer in Porous Media.* Albi, France, 2007.

Liang, L., et al. "Experimental study on effects of moisture content on combustion characteristics of simulated municipal solid wastes in a fixed bed." *Bioresource Technology* 99, no. 15 (October 2008): 7238-7246.

Lisbôa, A., C. Rombaldo, and W. Rodrigues. "Adding Tires to the Feedstock of the Petrosix Oil Shale Processing Plant." *XXII CIIQ.* shale processing plant". Retrieved on Date from, 2006.

Lu, C., and Y. C. Yortsos. "Pattern formation in reverse filtration combustion." *Physical review. E, Statistical, nonlinear, and soft matter physics* 72 (2), no. 3 (2005): 036201.1-036201.16.

Maciejewski, M. "Computational aspects of kinetic analysis.: Part B: The ICTAC Kinetics Project — the decomposition kinetics of calcium carbonate revisited, or some tips on survival in the kinetic minefield." *Thermochimica Acta* 355, no. 1-2 (July 2000): 145-154.

Moallemi, M. K., H. Zhang, and S. Kumar. "Numerical modeling of two-dimensional smoldering processes." *Combustion and Flame* 95, no. 1-2 (October 1993): 170-182.

Nazzal, J. M. "Influence of heating rate on the pyrolysis of Jordan oil shalenext term." *Journal of Analytical and Applied Pyrolysis* 62, no. 2 (February 2002): 225-238.

Ohlemiller, T.J. "Modeling of Smoldering Combustion Propagation." *Progress in Energy and Combustion Science* 11, no. 4 (1985): 277-310.

Oliveira, A. A. M., and M. Kaviany. "Nonequilibrium in the transport of heat and reactants in combustion in porous media." *Progress in Energy and Combustion Science* 27, no. 5 (May 2001): 523-545.

Pinjala, V., Y.C. Chen, and D. Luss. "Wrong-way behavior of packed-bed reactors: II. Impact of thermal dispersion." *A.I.Ch.E. Journal* 34, no. 10 (May 1988): 1663–1672.

Quintard, M., and S. Whitaker. "Local thermal equilibrium for transient heat conduction: theory and comparison with numerical experiments." *International Journal of Heat and Mass Transfer* 38 , no. 15 (1995): 2779-2796.

—. *One- and two-equation models for transient diffusion processes in two-phase systems.* Edited by Academic Press. Vol. 23. New York: Advances in Heat Transfer, 1993.

Rabinovich, O. S., and I. G. Gurevich. "Effect of heat losses on propagation of stationary low-temperature filtration combustion waves with forced filtration of the gas-oxidizer." *Combustion, Explosion, and Shock Waves* 20, no. 1 (janvier 1984): 29-35.

Rajeshwar, K., R. Nottenburg, and J. Dubow. "Thermophysical properties of oil shales." *Journal of Materials Science* 14 , no. 9 (1979): 2025-2052. .

Rein, G., C. Lautenberger, A. C. Fernandez-Pello, J. L. Torero, and D. L. Urban. "Application of genetic algorithms and thermogravimetry to determine the kinetics of polyurethane foam in smoldering combustion." *Combustion and Flame* 146, no. 1-2 (July 2006): 95-108.

Ryu, C., Y. B. Yang, A. Khor, N. E. Yates, V. N. Sharifi, and J. Swithenbank. "Effect of fuel properties on biomass combustion: Part I. Experiments—fuel type, equivalence ratio and particle size." *Fuel* 85, no. 7-8 (May 2006): 1039-1046.

Saastamoinen, J. J., R. Taipale, M. Horttanainen, and P. Sarkomaa. "Propagation of the ignition front in beds of wood particles." *Combustion and Flame* 123, no. 1-2 (October 2000): 214-226.

Sadiki, A., W. Kaminsky, H. Halim, and O. Bekri. "Fluidised bed pyrolysis of Moroccan oil shales using the hamburg pyrolysis process." *Journal of Analytical and Applied Pyrolysis* 70, no. 2 (December 2003): 427-435.

Samtani, M., D. Dollimore, and K. S. Alexander. "Comparison of dolomite decomposition kinetics with related carbonates and the effect of procedural variables on its kinetic parameters." *Thermochimica Acta* 392–393 (2002): 135–145.

Saoiabi, A., A. Doukkali, M. Hamad, A. Zrineh, M. Ferhat, and Y. Debyser. "Comportement thermique des schistes bitumineux de Timahdit (Maroc)Thermal behaviour of the Timahdit (Morocco) oil shales." *Comptes Rendus de l’Académie des Sciences - Series IIC - Chemistry* 4, no. 5 (May 2001b): 361-366.

Saoiabi, A., A. Doukkali, M. Hamad, A. Zrineh, M. Ferhat, and Y. Debyser. "Schistes bitumineux de Timahdit (Maroc) : composition et propriétés physicochimiquesTimahdit (Morocco) oil shales: composition and physicochemical properties." *Comptes Rendus de l’Académie des Sciences - Series IIC - Chemistry* 4, no. 5 (May 2001a): 351-360.

Schult, D.A., B.J. Matkowsky, V.A. Volpert, and A.C. Fernandez-Pello. "Propagation and extinction of forced opposed flow smolder waves." *Combustion and Flame* 101, no. 4 (June 1995): 471-490.

Sensöz, S., D. Angın, and S. Yorgun. "Influence of particle size on the pyrolysis of rapeseed (Brassica napus L.): fuel properties of bio-oil." *Biomass and Bioenergy* 19, no. 4 (October 2000): 271-279.

Shin, D., and S. Choi. "The combustion of simulated waste particles in a fixed bed." *Combustion and Flame* 121, no. 1-2 (April 2000): 167-180.

Skala, D., H. Kopsch, M. Sokic, H.J. Neumann, and J.A. Jovanovic. "Kinetics and modelling of oil shale pyrolysis." *Fuel* 69, no. 4 (1990): 490-496.

Sonibare, O. O., O.A. Ehinola, and R. Egashira. "Thermal and geochemical characterization of Lokpanta oil shales, Nigeria." *Energy Conversion and Management* 46, no. 15-16 (September 2005): 2335-2344.

Tagutchou, J.P. "Fixed bed gasification of wood char: Thermal, chemical and mechanical characterisation." *Eurotherm Seminar N° 81 Reactive Heat Transfer in Porous Media, Ecole des Mines d'Albi.* Albi - France, 2007.

Taulbee, D., T. Coburn, A. Rubel, G. Thomas, and L. Yates. *Eastern Oil Shale Symposium.* Lexington, 1982. 51.

Thunman, H., and Bo Leckner. "Co-current and counter-current fixed bed combustion of biofuel—a comparison." *Fuel* 82, no. 3 (February 2003): 275-283.

Thunman, H., and Bo Leckner. "Influence of size and density of fuel on combustion in a packed bed." *Proceedings of the Combustion Institute* 30, no. 2 (January 2005): 2939-2946.

Vantelon, J-P., B. Lodeho, S. Pignoux, J. L. Ellzey, and J. L. Torero. "Experimental observations on the thermal degradation of a porous bed of tires." *Proceedings of the Combustion Institute* 30, no. 2 (January 2005): 2239-2246.

Wang, J. H., C. Y. H. Chao, and W. Kong. "Experimental study and asymptotic analysis of horizontally forced forward smoldering combustion." *Combustion and Flame* 135, no. 4 (December 2003): 405-419.

Wang, J. H., C. Y. H. Chao, and W. Kong. "Experimental study and asymptotic analysis of horizontally forced forward smoldering combustion." *Combustion and Flame* 135, no. 4 (December 2003): 405-419.

Whitaker, S. "Improved Constraints for the Principle of Local Thermal Equilibrium." *Ind. & Eng. Chem.* 30 (1991): 983-997 .

Whitaker, S. "Simultaneous heat, mass and momentum transfer in porous media, a theory of drying." *Advances in Heat Transfer* 13 (1977): 119-203 .

Williams, P. T., and A. Ahmad. "Investigation of oil-shale pyrolysis processing conditions using thermogravimetric analysis." *Applied Energy* 66, no. 2 (June 2000): 113-133.

Williams, P. T., and N. Ahmad. "Influence of process conditions on the pyrolysis of Pakistani oil shales." *Fuel* 78, no. 6 (May 1999): 653-662.

Winderickx. "winderickx." http://www.winderickx.pl/en/msw_municipal_waste_incinerators.php.

Yang, C., Z. Fang, J. Liu, W. Liu, and H. Zhou. "A study on the kinetics of thermal decomposition of polyaniline." *Thermochimica Acta* 352-353 (2000): 159-164.

Yang, Y. B., C. Ryu, A. Khor, N. E. Yates, V. N. Sharifi, and J. Swithenbank. "Effect of fuel properties on biomass combustion. Part II. Modelling approach—identification of the controlling factors." *Fuel* 84, no. 16 (November 2005a): 2116-2130.

Yang, Y. B., C. Ryu, A. Khor, V. N. Sharifi, and J. Swithenbank. "Fuel size effect on pinewood combustion in a packed bed." *Fuel* 84, no. 16 (November 2005b): 2026-2038.

Yang, Y. B., H. Yamauchi, Nasserzadeh V., and J. Swithenbank. "Effects of fuel devolatilisation on the combustion of wood chips and incineration of simulated municipal solid wastes in a packed bed." *Fuel* 82, no. 18 (December 2003): 2205-2221.

Yang, Y. B., V. N. Sharifi, and J. Swithenbank. "Effect of air flow rate and fuel moisture on the burning behaviours of biomass and simulated municipal solid wastes in packed beds." *Fuel* 83, no. 11-12 (August 2004): 1553-1562.

Zhou, H., A.D. Jensen, P. Glarborg, P.A. Jensen, and A. Kavaliauskas. "Numerical modeling of straw combustion in a fixed bed." *Fuel* 84, no. 4 (March 2005): 389-403.

Ziyad, M., J.-P.P. Garnier, and M. Halim. "Nonisothermal kinetics of H2S and H2 generation from Timahdit oil shale." *Fuel* 65 , no. 5 (1986): 715-720.

Appendix A

Charcoal combustion (Mass balance of carbon)

Description	Nomenclature	value	unit
data:			
Reactor diameter	ϕ	0.091	m
Section	S	0.0065	m^2
Reactor height	H_R	0.28	m
Reactor Volume	V_R	0.00182	m^3
Front velocity	U_f	6,33E-05	$m\ s^{-1}$
Bed apparent density (before-comb.)	ρ_{0_bed}	1284,9	$kg\ m^{-3}$
Bed apparent density (post-comb.)	ρ_{f_bed}	1238,7	
Charcoal mass fraction in the bed	X_{CF}	100	-
composition:			
FC mass fraction	X_{FC}	3.6	% mass
% of FC oxidized by the front	CF_{oxy}	100	%
Flow rates:			
Ambient temperature	T_{amb}	273.15	K
Inlet air flow rate	qm_{AIR}	9.50	$l\ min^{-1}$
Inlet molar air flow rate $= qm_{AIR}/(60 \times 22.4)$	$qmol_{AIR}$	0.00707	$mol_{air}\ s^{-1}$
Inlet molar flow rate - N_2 $= qm_{AIR} \cdot (100 - 20.93)/100$	$qmol_{N_2}$	0.00559	$mol_{N2}\ s^{-1}$
Inlet molar flow rate - O_2 $= qm_{AIR} \cdot 20.93/100$	$qmol_{O_2}$	0.00148	$mol_{O2}\ s^{-1}$
CO et CO_2 in the smoke from: $C + [\frac{fr}{2} + (1-fr)]O_2 \rightarrow fr\ CO + (1-fr)CO_2$			
Mass flowrate of oxidized fixed carbon	$qmFC_{ox}$	0,0000191	$kg_C\ s^{-1}$
$= U_f \cdot S \cdot \rho_{0\_bed} \cdot X_{OS} \cdot X_{CF} \cdot CF_{OX}$			
Molar flowrate of oxidized fixed carbon	$qmolFC_{ox}$	0,00159	$mol_C\ s^{-1}$
$= qmFC_{ox}/0.012$			
Molar Fraction of C oxidized into CO:	fr	0.28	mole/mole
Molar flow rate of CO $= qmolFC_{ox} \cdot fr$	$qmol_{CO}$	0,00044	$mol_{CO}\ s^{-1}$
Molar flow rate of CO_2	$qmol_{CO_2}$	0,00114	$mol_{CO2}\ s^{-1}$

$= qmolFC_{ox} \cdot (1 - fr)$			
Molar flow rate - (O_2 consumed) $= qmolFC_{ox} \cdot \left[\frac{fr}{2} + (1 - fr) \right]$	$qmol_{O_2^{cons}}$	0,00137	$mol_{O2}\ s^{-1}$

Appendix B

Oil shale combustion (Mass balance of carbon)

Description	Nomenclature	value	unit
data:			
Reactor diameter	ϕ	0.091	*m*
Section	S	0.0065	*m^2*
Reactor height	H_R	0.28	*m*
Reactor Volume	V_R	0.00182	*m^3*
Front velocity	U_f	$6.13x10^{-5}$	*$m\ s^{-1}$*
Bed apparent density (before-comb.)	ρ_{0_bed}	1168.0	*$kg\ m^{-3}$*
Bed apparent density (post-comb.)	ρ_{f_bed}	956.9	
Oil shale mass fraction in the bed	X_{OS}	75.0	-
Oil shale composition:			
Moisture	X_{H_2O}	2.50	*% mass*
Repartition of organic matter:			
% of oil shale converted into NMHC	X_{NMHC}	1.93	*% mass*
% of oil shale converted into oil	X_{oil}	10.28	*% mass*
% of oil shale converted into CO of devolatilization	X_{CO}	0.20	*% mass*
% of oil shale converted into CO_2 of devolatilization	X_{CO_2}	0.98	*% mass*
% of oil shale converted into CH_4 of devolatilization	X_{CH_4}	0.37	*% mass*
% of oil shale converted into SO_2 of devolatilization	X_{SO_2}	0.93	*% mass*
FC mass fraction in the oil shale	X_{FC}	4.70	*% mass*
% of FC oxidized by the front	CF_{oxy}	88.20	*%*
$CaCO_3$ mass fraction in the oil shale	X_{CaCO_3}	34.60	*% mass*
$CaCO_3$ mass lost	$CaCO_3^{decarb}$	42.30	*% of $CaCO_3$*
Flow rates:			
Ambient temperature	T_{amb}	273.15	*K*
Inlet air flow rate	qm_{AIR}	9.50	*$l\ min^{-1}$*

Inlet molar air flow rate $= qm_{AIR}/(60 \times 22.4)$	$qmol_{AIR}$	0.00707	*mol air* s^{-1}
Inlet molar flow rate - N_2 $= qm_{AIR} \cdot (100 - 20.93)/100$	$qmol_{N_2}$	0.00559	*mol* $N_2\ s^{-1}$
Inlet molar flow rate - O_2 $= qm_{AIR} \cdot 20.93/100$	$qmol_{O_2}$	0.00148	*mol* $O_2\ s^{-1}$

CO et CO₂ in the smoke from: $C + [\frac{fr}{2} + (1 - fr)]O_2 \rightarrow fr\ CO + (1 - fr)CO_2$

Mass flowrate of oxidized fixed carbon $= U_f \cdot S \cdot \rho_{0\_bed} \cdot X_{OS} \cdot X_{CF} \cdot CF_{OX}$	$qmFC_{ox}$	0.0000145	$kg_C\ s^{-1}$
Molar flowrate of oxidized fixed carbon $= qmFC_{ox}/0.012$	$qmolFC_{ox}$	0.00121	$mol_C\ s^{-1}$
Molar Fraction of C oxidized into CO:	fr	0.565	*mole/mole*
Molar flow rate of CO $= qmolFC_{ox} \cdot fr$	$qmol_{CO}$	0.00068	$mol_{CO}\ s^{-1}$
Molar flow rate of CO_2 $= qmolFC_{ox} \cdot (1 - fr)$	$qmol_{CO_2}$	0.00053	$mol_{CO2}\ s^{-1}$
Molar flow rate - (O_2 consumed) $= qmolFC_{ox} \cdot \left[\frac{fr}{2} + (1 - fr)\right]$	$qmol_{O_2^{cons}}$	0.00087	mol_{O2} *cons* s^{-1}

Pyrolysis gases

Molar flow rate of CO from devolatilization $= U_f \cdot S \cdot \rho_{0\_bed} \cdot X_{OS} \cdot \frac{X_{CO}}{0.028}$	$qmol_{CO^{pyr}}$	2.50x10^{-6}	*mol* s^{-1}
Molar flow rate of CO_2 from devolatilization $= U_f \cdot S \cdot \rho_{0\_bed} \cdot X_{OS} \cdot \frac{X_{CO_2}}{0.044}$	$qmol_{CO_2^{pyr}}$	7.78 x10^{-5}	*mol* s^{-1}
Molar flow rate of CH_4 from devolatilization $= U_f \cdot S \cdot \rho_{0\_bed} \cdot X_{OS} \cdot \frac{X_{CH_4}}{0.016}$	$qmol_{CH_4^{pyr}}$	8.08 x10^{-5}	*mol* s^{-1}
Molar flow rate of SO_2 from devolatilization $= U_f \cdot S \cdot \rho_{0\_bed} \cdot X_{OS} \cdot \frac{X_{SO_2}}{0.064}$	$qmol_{SO_2^{pyr}}$	5.08 x10^{-5}	*mol* s^{-1}
Molar flow rate of NMHC from devolatilization $= U_f \cdot S \cdot \rho_{0\_bed} \cdot X_{OS} \cdot \frac{X_{NMHC}}{0.016}$	$qmol_{NMHC^{pyr}}$	4.22 x10^{-4}	*mol* s^{-1}

Drying and decarbonation

Mass flow rate of H_2O from drying	$qmol_{H_2O^{drying}}$	0.00049	$mol_{H2O}\ s^{-1}$

$=U_f \cdot S \cdot \rho_{0\_bed} \cdot X_{OS} \cdot \frac{X_{H_2O}}{0.014}$			
Molar flow rate of CO_2 from decarbonation $=U_f \cdot S \cdot \rho_{0\_bed} \cdot X_{OS} \cdot X_{CaCO_3} \frac{CaCO_3^{decarb}}{0.044}$	$qmol_{CO_2^{decarb}}$	0.001162	$mol_{CO2}\ s^{-1}$
Oxygen consumed			
Molar flow rate of O_2 from smoke $=qmol_{O_2} - qmol_{O_2^{cons}}$	$qmol_{O_2^{smoke}}$	0.00061	$mol_{O2}\ s^{-1}$

Appendix C

Extracted from (Lapene 2006, P. 46-48) :

B.1 La méthode des volumes finis

La méthode a été décrite pour la première fois en 1971 par Patanker et Spalding et publiée en 1980 par Patankar [14].

La méthode des volumes finis est une technique de discrétisation qui convertit les équations de conservation aux dérivées partielles en équations algébriques qui peuvent être résolues numériquement. La technique des volumes de contrôle consiste dans l'intégration des équations aux dérivées partielles sur chaque volume de contrôle pour obtenir les équations discrétisées qui conservent toutes les grandeurs physiques sur un volume de contrôle. Les différentes étapes de la mise en oeuvre sont :

- le domaine de calcul est discrétisé en un nombre fini de points (les noeuds du maillage), autour desquels on définit des volumes élémentaires (appelés volumes de contrôle) contigus, non juxtaposés et sans discontinuités aux interfaces,
- les équations modèles sont intégrées sur chaque volume de contrôle,
- les intégrales sur chaque volume de contrôle en un noeud donné sont évaluées en approchant la variation de la grandeur scalaire par des profils ou des lois d'interpolations entres les noeuds voisins du point considéré,
- les équations algébriques sont écrites en fonction des valeurs de la grandeur scalaire aux noeuds du maillage,
- le système algébrique linéaire obtenu est résolu.

Les avantages de cette méthode sont :

la préservation du caractère conservatif des équations sur chaque volume de contrôle (continuité des flux aux interfaces), valable pour n'importe quelle finesse de maillage,
- la mise en oeuvre relativement facile,
- l'applicabilité aux géométries complexes,
- le temps de calcul et de stockage mémoire raisonnable (matrice de type bande).

L'inconvénient est le manque de précision par rapport à des méthodes de haut degré de précision telles que les méthodes spectrales. Vous trouverez sur la figure (B.1) une illustration sur un maillage en 2 dimensions.

Ce maillage est un maillage régulier, c'est à dire que $\Delta x = \Delta y = \Delta h$. Le volume de contrôle est représenté en gris. Il est habituel de désigné le point lié au volume de contrôle par la lettre P. Les autres points du maillage seront notés (N, S, E et W) en référence aux points cardinaux Nord, Sud, East, West écrits en anglais. Pour évaluer l'intégrale sur le volume de contrôle on a besoin de points intermédiaires situés sur la frontière. Celui situé entre P et E sera noté e, celui entre P et W sera noté w. Il en va de même pour les autres.

Notre code sera un code 1D (une dimension). Nous utiliserons un maillage régulier. Dans ce cas la distance entre P et respectivement N, S, E et W est la même et on la note Δx. La distance entre P et respectivement n, s, e et w vaut donc $\Delta x/2$. On adopte d'autres notations : la grandeur scalaire Φ évaluée au point P que

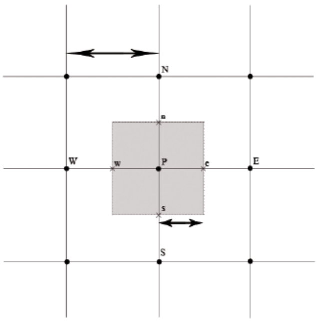

FIG. B.1 – Maillage pour un domaine en 2 dimensions

l'on note habituellement Φ_P en convention volumes finis sera noté Φ_i. La grandeur scalaire Φ évaluée au point E sera notée Φ_{i+1} et par analogie la grandeur scalaire Φ évaluée au point W sera notée Φ_{i-1}. Il en découle que Φ évaluée en e sera notée $\Phi_{i+\frac{1}{2}}$ et Φ évaluée en w, $\Phi_{i-\frac{1}{2}}$.

Les termes temporels seront traités avec un schéma implicite décentré d'ordre 1. On notera Φ^n, la grandeur scalaire évaluée à l'instant t et Φ^{n+1}, la grandeur scalaire évaluée à l'instant $t+\Delta t$, avec Δt le pas de temps. Les termes diffusifs seront traités avec un schéma centré d'ordre 1, les termes convectifs avec un schéma amont (ou UPWIND).

B.2 Equation de transport des espèces

Soit l'équation (2.2), on la reformule ainsi :

$$\epsilon_g\rho_g\frac{\partial Y_k}{\partial t}+\epsilon_g Y_k\frac{\partial \rho_g}{\partial t}+\rho_g v_g\frac{\partial Y_k}{\partial x}+Y_k\frac{\partial}{\partial x}\left(\rho_g v_g\right)-\frac{\partial}{\partial x}\left(\rho_g D_k^*\frac{\partial Y_k}{\partial x}\right) = \dot{R}_{g,k} \tag{B.1}$$

$$Y_k\left(\frac{\partial}{\partial x}\left(\rho_g v_g\right)+\epsilon_g\frac{\partial \rho_g}{\partial t}\right)+\epsilon_g\rho_g\frac{\partial Y_k}{\partial t}+\rho_g v_g\frac{\partial Y_k}{\partial x}-\frac{\partial}{\partial x}\left(\rho_g D_k^*\frac{\partial Y_k}{\partial x}\right) = \dot{R}_{g,k} \tag{B.2}$$

On reconnait l'équation 2.1. On obtient finalement :

$$Y_k\dot{R}_g+\epsilon_g\rho_g\frac{\partial Y_k}{\partial t}+\rho_g v_g\frac{\partial Y_k}{\partial x}-\frac{\partial}{\partial x}\left(\rho_g D_k^*\frac{\partial Y_k}{\partial x}\right)=\dot{R}_{g,k} \tag{B.3}$$

On intègre maintenant sur le volume de contrôle :

$$\int_t^{t+\Delta t}\int_w^e Y_k\dot{R}_g dxdt+\int_t^{t+\Delta t}\int_w^e \epsilon_g\rho_g\frac{\partial Y_k}{\partial t}dxdt+\int_t^{t+\Delta t}\int_w^e \rho_g v_g\frac{\partial Y_k}{\partial x}dxdt$$

$$-\int_t^{t+\Delta t}\int_w^e \frac{\partial}{\partial x}\left(\rho_g D_k^*\frac{\partial Y_k}{\partial x}\right)dxdt=\int_t^{t+\Delta t}\int_w^e \dot{R}_{g,k}dxdt \tag{B.4}$$

$$Y_k|_P^{n+1}\left.\dot{R}_g\right|_P^{n+1}\Delta x\Delta t+\left[\epsilon_g\rho_g\frac{\partial Y_k}{\partial t}\right]_t^{t+\Delta t}\Delta x+\rho_g|_P^{n+1}\ v_g|_P^{n+1}\left[Y_k\right]_w^e\Delta t$$

$$-\left[\rho_g D_k^*\frac{\partial Y_k}{\partial x}\right]_w^e\Delta t=\left.\dot{R}_{g,k}\right|_P^{n+1}\Delta x\Delta t \tag{B.5}$$

$$Y_k|_P^{n+1}\left.\dot{R}_g\right|_P^{n+1}\Delta x+\left(\epsilon_g\rho_g\right)|_P^{n+1}\left[\frac{\partial Y_k}{\partial t}\right]_t^{t+\Delta t}\frac{\Delta x}{\Delta t}+\left(\rho_g v_g\right)|_P^{n+1}\left[Y_k\right]_w^e-\left[\rho_g D_k^*\frac{\partial Y_k}{\partial x}\right]_w^e=\left.\dot{R}_{g,k}\right|_P^{n+1}\Delta x \tag{B.6}$$

On introduit l'opérateur $max(.,.)$ tel que :

$$max(A,B)=\begin{cases} A\ si\ A>B \\ B\ sinon\end{cases} \tag{B.7}$$

En appliquant le schéma amont l'équation (B.6) devient :

$$\begin{aligned}
&Y_k|_P^{n+1} \, \dot{R}_g\Big|_P^{n+1} \Delta x + (\epsilon_g \rho_g)|_P^{n+1} \frac{Y_k|_P^{n+1} - Y_k|_P^n}{\Delta t} \Delta x \\
&+ \rho_g|_P^{n+1} \left[Y_k|_P^{n+1} \, max\left(v_g|_P^{n+1}, 0 \right) - Y_k|_E^{n+1} \, max\left(-v_g|_P^{n+1}, 0 \right) + Y_k|_W^{n+1} \, max\left(v_g|_P^{n+1}, 0 \right) \right. \\
&\left. - Y_k|_P^{n+1} \, max\left(-v_g|_P^{n+1}, 0 \right) \right] - \left[(\rho_g D_k^*)|_e^{n+1} \left(\frac{Y_k|_E^{n+1} - Y_k|_P^{n+1}}{\Delta x} \right) - (\rho_g D_k^*)|_w^{n+1} \left(\frac{Y_k|_P^{n+1} - Y_k|_W^{n+1}}{\Delta x} \right) \right] \\
&= \dot{R}_{g,k}\Big|_P^{n+1} \Delta x
\end{aligned} \tag{B.8}$$

En introduisant les notations énoncées précédemment et en réorganisant la formule précédente on obtient :

$$\begin{aligned}
&Y_k|_i^{n+1} \left\{ \dot{R}_g\Big|_i^{n+1} \Delta x + (\epsilon_g \rho_g)|_i^{n+1} \frac{\Delta x}{\Delta t} + \rho_g|_i^{n+1} \left[max\left(v_g|_i^{n+1}, 0 \right) \right. \right. \\
&\left. \left. + max\left(-v_g|_i^{n+1}, 0 \right) \right] + \frac{(\rho_g D_k^*)|_{i+\frac{1}{2}}^{n+1}}{\Delta x} + \frac{(\rho_g D_k^*)|_{i-\frac{1}{2}}^{n+1}}{\Delta x} \right\} \\
&+ Y_k|_{i+1}^{n+1} \left\{ - \rho_g|_i^{n+1} \, max\left(-v_g|_i^{n+1}, 0 \right) - \frac{(\rho_g D_k^*)|_{i+\frac{1}{2}}^{n+1}}{\Delta x} \right\} \\
&+ Y_k|_{i-1}^{n+1} \left\{ - \rho_g|_i^{n+1} \, max\left(v_g|_i^{n+1}, 0 \right) - \frac{(\rho_g D_k^*)|_{i-\frac{1}{2}}^{n+1}}{\Delta x} \right\} = \dot{R}_{g,k}\Big|_i^{n+1} \Delta x + (\epsilon_g \rho_g)|_i^{n+1} \frac{\Delta x}{\Delta t} Y_k|_i^n
\end{aligned} \tag{B.9}$$

On obtient donc un système du type $A \, Y_k|_i^{n+1} + B \, Y_k|_{i+1}^{n+1} + C \, Y_k|_{i-1}^{n+1} = D$ pour $1 \leq i \leq nx$ et pour $n \neq 0$, avec nx le nombre de noeuds.

Discrétisons maintenant les conditions aux limites.

Si $|P_{eO}| < 1$ alors :

$$\begin{aligned}
Y_k|_1^{n+1} &= \frac{Y_k^{amb} + Y_k|_2^{n+1}}{2}, \ \forall n \\
Y_k|_{nx}^{n+1} &= \frac{Y_k^{amb} + Y_k|_{nx-1}^{n+1}}{2}, \ \forall n
\end{aligned} \tag{B.10}$$

Si $|P_{eO}| > 1$ et $v_g > 0$ alors :

$$Y_k|_1^{n+1} = \frac{Y_k^{amb} + Y_k|_2^{n+1}}{2}, \ \forall n \tag{B.11}$$

et en $x = L$, condition de type Dankwerts, ce qui se traduit par :

$$\begin{aligned}
&Y_k|_{nx}^{n+1} \left\{ \dot{R}_g\Big|_{nx}^{n+1} \frac{\Delta x}{2} + (\epsilon_g \rho_g)|_{nx}^{n+1} \frac{\Delta x}{2\Delta t} + (\rho_g v_g)|_{nx}^{n+1} \right\} \\
&+ Y_k|_{nx-1}^{n+1} \left\{ - (\rho_g v_g)|_{nx}^{n+1} \right\} = \dot{R}_{g,k}\Big|_{nx}^{n+1} \frac{\Delta x}{2} + (\epsilon_g \rho_g)|_{nx}^{n+1} \frac{\Delta x}{2\Delta t} Y_k|_{nx}^n
\end{aligned} \tag{B.12}$$

Si $|P_{eO}| > 1$ et $v_g < 0$ alors :

en x=0, condition de type Dankwerts ce qui se traduit par :

$$\begin{aligned}
&Y_k|_1^{n+1} \left\{ \dot{R}_g\Big|_1^{n+1} \frac{\Delta x}{2} + (\epsilon_g \rho_g)|_1^{n+1} \frac{\Delta x}{2\Delta t} + (\rho_g v_g)|_1^{n+1} \right\} \\
&+ Y_k|_2^{n+1} \left\{ (\rho_g v_g)|_1^{n+1} \right\} = \dot{R}_{g,k}\Big|_1^{n+1} \frac{\Delta x}{2} + (\epsilon_g \rho_g)|_1^{n+1} \frac{\Delta x}{2\Delta t} Y_k|_1^n
\end{aligned} \tag{B.13}$$

et en $x = L$:

$$Y_k|_{nx}^{n+1} = \frac{Y_k^{amb} + Y_k|_{nx-1}^{n+1}}{2}, \ \forall n \tag{B.14}$$

Enfin les conditions initiales se traduisent par :

$$Y_k\big|_i^0 = Y_k^{amb}, \ \forall i \tag{B.15}$$

B.3 Equation de la chaleur du solide

En reprenant les mêmes étapes que pour la discrétisation de l'équation précédente on obtient finalement, pour $1 < i < nx$ et pour $n \neq 0$ le système suivant :

$$T_s\big|_i^{n+1}\left[(\epsilon_s\rho_s C_{ps})\big|_i^{n+1}\frac{\Delta x}{\Delta t} + \frac{\lambda_s\big|_{i-\frac{1}{2}}^{n+1}}{\Delta x} + \frac{\lambda_s\big|_{i+\frac{1}{2}}^{n+1}}{\Delta x} + \Gamma_{s,g}\big|_i^n\,\Delta x\right] + T_s\big|_{i-1}^{n+1}\left[-\frac{\lambda_s\big|_{i-\frac{1}{2}}^{n+1}}{\Delta x}\right]$$

$$+\,T_s\big|_{i+1}^{n+1}\left[-\frac{\lambda_s\big|_{i+\frac{1}{2}}^{n+1}}{\Delta x}\right] = T_s\big|_i^n\,(\epsilon_s\rho_s C_{ps})\big|_i^n\,\frac{\Delta x}{\Delta t} + \Gamma_{s,g}\big|_i^n\,\Delta x\,T_g\big|_i^n + Q_s\big|_i^{n+1}\,\Delta x \tag{B.16}$$

Discrétisons maintenant les conditions aux limites :

Si $t < t_{all.}$ alors :

$$T_s\big|_1^{n+1}\left[\frac{\lambda_s\big|_1^{n+1}}{\Delta x}\right] + T_s\big|_2^{n+1}\left[\frac{-\,\lambda_s\big|_1^{n+1}}{\Delta x}\right] = \Phi_{rad}\big|^{n+1}\,\frac{\Delta x}{2} \tag{B.17}$$

sinon :

$$T_s\big|_1^{n+1} = T_s\big|_2^{n+1} \tag{B.18}$$

et :

$$T_s\big|_{nx}^{n+1} = T_s\big|_{nx-1}^{n+1} \tag{B.19}$$

Enfin les conditions initiales se traduisent par :

$$T_s\big|_i^0 = T_s^{amb} \tag{B.20}$$

B.4 Equation de la chaleur du gaz

En reprenant les mêmes étapes que pour la discrétisation de l'équation précédente on obtient finalement, pour $1 < i < nx$ et pour $n \neq 0$ le système suivant :

$$\begin{aligned}
&T_g\big|_i^{n+1}\Bigg\{(\epsilon_g\rho_g C_{pg})\big|_i^{n+1}\frac{\Delta x}{\Delta t} + (\epsilon_g\rho_g C_{pg})\big|_i^{n+1}\Big[max\left(v_g\big|_i^{n+1},0\right)\\
&\quad +max\left(-v_g\big|_i^{n+1},0\right)\Big] + \frac{\lambda_s\big|_{i-\frac{1}{2}}^{n+1}}{\Delta x} + \frac{\lambda_g\big|_{i+\frac{1}{2}}^{n+1}}{\Delta x} + \Gamma_{g,s}\big|_i^n\,\Delta x\Bigg\}\\
&\quad + T_g\big|_{i-1}^{n+1}\left\{(-\,\epsilon_g\rho_g C_{pg})\big|_i^{n+1}\,max\left(-v_g\big|_i^{n+1}\right) - \frac{\lambda_g\big|_{i-\frac{1}{2}}^{n+1}}{\Delta x}\right\}\\
&\quad + T_g\big|_{i+1}^{n+1}\left\{(-\,\epsilon_g\rho_g C_{pg})\big|_i^{n+1}\,max\left(v_g\big|_i^{n+1}\right) - \frac{\lambda_g\big|_{i+\frac{1}{2}}^{n+1}}{\Delta x}\right\}\\
&= T_g\big|_i^n\,(\epsilon_g\rho_g C_{pg})\big|_i^n\,\frac{\Delta x}{\Delta t} + \Gamma_{g,s}\big|_i^n\,\Delta x\,T_s\big|_i^n + Q_g\big|_i^{n+1}\,\Delta x
\end{aligned} \tag{B.21}$$

Discrétisons maintenant les conditions aux limites.

Si $|P_{eT}| < 1$ alors :

$$T_g|_1^{n+1} = \frac{T_g^{amb} + T_g|_2^{n+1}}{2}, \ \forall n$$

$$T_g|_{nx}^{n+1} = \frac{T_g^{amb} + T_g|_{nx-1}^{n+1}}{2}, \ \forall n \tag{B.22}$$

Si $|P_{eT}| > 1$ et $v_g > 0$ alors :

$$T_g|_1^{n+1} = \frac{T_g^{amb} + T_g|_2^{n+1}}{2}, \ \forall n \tag{B.23}$$

et en $x = L$, condition de type Dankwerts, ce qui se traduit par :

$$\begin{aligned} T_g|_1^{n+1} \Big\{ (\epsilon_g \rho_g C_{pg})|_1^{n+1} \frac{\Delta x}{\Delta t} + (\epsilon_g \rho_g C_{pg})|_1^{n+1} \Big[max\left(v_g|_1^{n+1}, 0\right) \\ + max\left(-v_g|_1^{n+1}, 0\right) \Big] + \Gamma_{g,s}|_1^n \, \Delta x \Big\} \\ + T_g|_2^{n+1} \Big\{ (- \, \epsilon_g \rho_g C_{pg})|_1^{n+1} \, max\left(v_g|_1^{n+1} \right) \Big\} \\ = T_g|_1^n \, (\epsilon_g \rho_g C_{pg})|_1^n \frac{\Delta x}{\Delta t} + \Gamma_{g,s}|_1^n \, \Delta x \, T_s|_1^n + Q_g|_1^{n+1} \, \Delta x \end{aligned} \tag{B.24}$$

Si $|P_{eO}| > 1$ et $v_g < 0$ alors :

en x=0, condition de type Dankwerts ce qui se traduit par :

$$\begin{aligned} T_g|_{nx}^{n+1} \Big\{ (\epsilon_g \rho_g C_{pg})|_{nx}^{n+1} \frac{\Delta x}{\Delta t} + (\epsilon_g \rho_g C_{pg})|_{nx}^{n+1} \Big[max\left(v_g|_{nx}^{n+1}, 0\right) \\ + max\left(-v_g|_{nx}^{n+1}, 0\right) \Big] + \Gamma_{g,s}|_{nx}^n \, \Delta x \Big\} \\ + T_g|_{nx-1}^{n+1} \Big\{ (- \, \epsilon_g \rho_g C_{pg})|_{nx}^{n+1} \, max\left(-v_g|_{nx}^{n+1} \right) \Big\} \\ = T_g|_{nx}^n \, (\epsilon_g \rho_g C_{pg})|_{nx}^n \frac{\Delta x}{\Delta t} + \Gamma_{g,s}|_{nx}^n \, \Delta x \, T_s|_{nx}^n + Q_g|_{nx}^{n+1} \, \Delta x \end{aligned} \tag{B.25}$$

et en $x = L$:

$$T_g|_{nx}^{n+1} = \frac{T_g^{amb} + T_g|_{nx-1}^{n+1}}{2}, \ \forall n \tag{B.26}$$

Enfin les conditions initiales se traduisent par :

$$T_g|_i^0 = T_g^{amb}, \ \forall i \tag{B.27}$$

B.5 Equation de la pression

En reprenant les mêmes étapes que pour la discrétisation de l'équation précédente on obtient finalement, pour $1 < i < nx$ et pour $n \neq 0$ le système suivant :

$$\begin{aligned} P_g|_{i-1}^{n+1} \left\{ \left. \left(\frac{-\rho_g \epsilon_g}{\mu_g} \right) \right|_{i-\frac{1}{2}}^{n+1} \frac{1}{\Delta x} \right\} \\ + P_g|_i^{n+1} \left\{ \left. \left(\frac{\epsilon_g \bar{M}_g}{R T_g} \right) \right|_i^{n+1} \frac{\Delta x}{\Delta t} - \left. \left(\frac{\epsilon_g \bar{M}_g}{R T_g^2} \right) \right|_i^{n+1} \left(T_g|_i^{n+1} - T_g|_i^n \right) \frac{\Delta x}{\Delta t} \right. \end{aligned}$$

$$+ \left(\frac{\rho_g K}{\mu_g}\right)\bigg|_{i+\frac{1}{2}}^{n+1} \frac{1}{\Delta x} + \left(\frac{\rho_g K}{\mu_g}\right)\bigg|_{i-\frac{1}{2}}^{n+1} \frac{1}{\Delta x} + \left(\frac{\epsilon_g}{RT_g}\right)\bigg|_{i}^{n+1} \left(\bar{M}_g\big|_i^{n-1} - \bar{M}_g\big|_i^{n}\right) \frac{\Delta x}{\Delta t}\Bigg\}$$

$$+ P_g\big|_{i+1}^{n+1} \left\{ \left(\frac{-\rho_g \epsilon_g}{\mu_g \Delta x}\right)\bigg|_{i+\frac{1}{2}}^{n+1} \right\} = \dot{R}_g\Big|_i^{n+1} \Delta x + \left(\frac{\epsilon_g \bar{M}_g}{RT_g}\right)\bigg|_i^{n+1} \frac{\Delta x}{\Delta t}\, P_g\big|_i^n \tag{B.28}$$

Discrétisons maintenant les conditions aux limites.

. En $x = 0$, on obtient :

$$P_g\big|_1^{n+1} \left\{ \left(\frac{\epsilon_g \bar{M}_g}{RT_g}\right)\bigg|_1^{n+1} \frac{\Delta x}{2\Delta t} - \left(\frac{\epsilon_g \bar{M}_g}{RT_g^2}\right)\bigg|_1^{n+1} \left(T_g\big|_1^{n+1} - T_g\big|_1^{n}\right) \frac{\Delta x}{2\Delta t} + \left(\frac{\rho_g K}{\mu_g}\right)\bigg|_{\frac{3}{2}}^{n+1} \frac{2}{\Delta x} \right\}$$

$$+ P_g\big|_2^{n+1} \left\{ \left(\frac{-\rho_g \epsilon_g}{\mu_g \Delta x}\right)\bigg|_{\frac{3}{2}}^{n+1} \right\} = \dot{R}_g\Big|_2^{n+1} \frac{\Delta x}{2} + \left(\frac{\epsilon_g \bar{M}_g}{RT_g}\right)\bigg|_2^{n+1} \frac{\Delta x}{2\Delta t}\, P_g\big|_i^n + (\rho_g v_g)\big|_1^{n+1} \tag{B.29}$$

et en $x = L$:

$$P_g\big|_{nx}^{n+1} = \frac{\left(P_g\big|_{nx-1}^{n+1} + P^{amb}\right)}{2} \tag{B.30}$$

Appendix D

Energy balance over an experiment

The total heat loss of the combustion cell can be estimated as the sum:

- of the heat lost at the external walls of the cell;
- and the heat necessary to heat the cell from the initial room temperature to its final average temperature.

The loss at the external walls was calculated following:

$$Q_{wall} = h\, S\, (T_p - T_{amb})\, t$$

where:

- the heat transfer coefficient by natural convection *h* was estimated t₀ 15 Wm^{-2} K^{-1} ;
- the external surface of the cell *S* was estimated at 0.251 m^2;
- the temperature of the external surface T_p was measured at 60°C;
- the ambient temperature T_{amb} was 18°C;
- the time *t* was estimated at half the duration of an experiment, or 2500 s, since the external surface at a given level of the cell is hot only when the front has passed through.

The energy to heat the combustion cell from the room temperature T_{amb} to the average final temperature T_p can be expressed:

$$Q_{cell} = m\, Cp\, (T_p - T_{amb})$$

where:

- m is the mass of the cell, 5.0 kg;

- *Cp* is the specific heat of the insulation material, estimated at 1386 $J.kg^{-1}.K^{-1}$

The total heat loss is then $Q_{tot} = Q_{wall}+Q_{cell} = 291+396 = 687$ kJ

The fixed carbon in the cell was oxidized following:

$$C+[\frac{fr}{2}+(1-fr)]O_2 \rightarrow fr\,CO+(1-fr)CO_2$$

The calorific value for this reaction is $\Delta H_{ox} = 19470$ kJ kg^{-1} for *fr* = 0.565.

The total mass of fixed carbon oxidized was $m_{FC\text{-}ox} = 84.2$ g.

The energy released by the combustion of the fixed carbon was:

$Q_{ox} = m_{FC\text{-}ox} . \Delta Hox = 1640$ kJ

The fraction of lost energy was then
$Fr_{lost} = Q_{tot}/Q_{ox} = 0.42$

Appendix E

Adiabatic combustion temperature

Adiabatic combustion temperature

1g crude OS	**(g)**	**0,75 (g) OS**		**0,75 (g) pyrolized OS**		**100 g**	**Char + inert (g)**	**(mol)**	**1mole of C**
CF	4,7	CF	3,53	CF	3,53	4,05	4,05	0,34	1
carbonates	34,6	carbonates	25,95	carbonates	25,95	29,79	29,79	0,30	0,88
H_2O	2,5	H_2O	1,88	H_2O	0	0,00	66,16	0,66	1,96
MV	14,7	MV	11,03	MV	0	0,00			
inert	43,5	inert	32,63	inert	32,63	37,46			
		Sand	25	Sand	25	28,70		(M=100)	
		tot	100,00		87,1	100,00	100,00		

Air stoechiometric

fr =	**0,565**				
C	**(1-fr/2) (O_2 +3,8 N_2)**	→	**CO**	**CO_2**	**N_2**
1	0,72	→	0,57	0,44	2,73

on (1) /off (0)	1		
$CaCO_3$	→	**CO_2**	**CaO**
0,88	→	0,88	0,88
I_{NERT}	→	**I_{NERT}**	
1,96	→	**1,96**	

Conservation of enthalpy

The total enthalpy of reactants is equal the total enthalpy of products:

$$\sum_r n_r \left[\Delta h^0_{f,r} + \int_{T_{amb}}^{T_r} Cp_r \, dT\right] = \sum_p n_r \left[\Delta h^0_{f,p} + \int_{T_{amb}}^{T_p} Cp_p \, dT\right]$$

$$\sum n_p \left[Cp_r \times (T_p - T_{amb})\right] - \sum n_r \left[Cp_r \times (T_r - T_{amb})\right] = \sum \Delta h_{f,p} - \sum \Delta h_{f,r}$$

indices
r: reactants
p: products
amb: ambient
ad: adiabatic

assuming that: i)the heat capacities are constant (but they still depend on the species type k); ii)the temperature of reactant, Tr = Tamb; iii)T_p=T_{ad}:

$$\sum n_p \left[Cp_p \times (T_{ad} - T_{amb})\right] = \sum \Delta h_{f,p} - \sum \Delta h_{f,r} = H_{react} \quad \rightarrow \quad \mathbf{T_{ad} = T_{amb} + H_{react} / (\sum n_p \, Cp)}$$

Enthalpy of combustion		
∑dH produit	-1139	*J/mol C*
∑dH réactifs	-1066,15	*J/mol C*
Heat = ∑dH product - ∑dH reactant =	72624	*J/mol C*

Molar heat capacity (J. mol^{-1}.K^{-1} at 600K)			
N_2	**CO_2**	**CO**	**INERT = CaO**
30,75	45,75	30,45	49,80
∑ np Cp	302,72	*J/mol*	

Theoretic

T_{ad} =	538	*K*
	265	*°C*